VLADIMIR GONÇALVES MIRANDA

Kondo Effect in disordered graphene

Niterói

Março 2014

VLADIMIR GONÇALVES MIRANDA

Kondo Effect in disordered graphene

Tese apresentada ao Curso de Pós-Graduação em Física da Universidade Federal Fluminense, como requisito parcial para obtenção do Título de Doutor em Física.

Orientador:
Prof. Dr. CAIO HENRIQUE LEWENKOPF

Universidade Federal Fluminense
Instituto de Física

Niterói

Março 2014

M672 Miranda, Vladimir Gonçalves
Kondo effect in disordered graphene / Vladimir Gonçalves Miranda ; orientador: Caio Lewenkopf. -- Niterói, 2014.
106 p. : il.

Tese (Doutorado) – Universidade Federal Fluminense, Instituto de Física, 2014.
Bibliografia: p. 100-106.

1.EFEITO KONDO. 2.PSEUDOGAP. 3.GRAFENO. 4.VACÂNCIA. 5.DESORDEM. 6.FASE DE GRIFFITHS. I.Lewenkopf, Caio, Orientador. II.Universidade Federal Fluminense. Instituto de Física, Instituição responsável. III.Título.

CDD 530.41

To the memory of my uncle Paulo
and to my nephew Gabriel.

Acknowledgements

I would like to thank Prof. Caio Lewenkopf for the supervision. His enthusiasm with science is stimulating, and the clear way he exposes his thoughts has the power to transform the most complexes topics into easy matter. Add to this his good humour and politeness and you get the successful recipe for putting together great learning and pleasant moments.

I am also very grateful to Prof. Luis Gregorio Dias, our collaborator in this work. I am indebted with him for all the countless emails and skype conversations to talk about physics. Prof. Luis never let a single email question unanswered (even the most silly one), and my learning about the Kondo physics and the NRG method were extremely enriched due to him.

I am grateful to the colleagues Andre Ricardo, Rhonald, Leandro, Mariana, Jesus, Bruno, Daiara and Emilia for the Thursday's meetings to discuss about graphene. Each of them contributed in a singular way for my understanding of different aspects of this vibrating area in those evening encounters.

The friends collected during this journey, specially Álvaro, Cadu, Daniel, Jaque, Orahcio, Thiago and Victor for the friendship which propitiated so many nice moments all over these PhD years.

To my mother for all her dedication to her children which allowed me to get in this position today. I own to her the die hard character I (try to) have in all the things I get involved.

To my family, that helped me in different ways and understood the times I had to stay apart from them to dedicate myself to my studies.

Last but not least to my lovely wife for all the support all over these years. Her patience and comprehension have no counterpart. Besides all the hours I had to dedicate to this project, stealing me from her company, she has always stimulated me to go ahead.

Abstract

Recent experiments found evidences that vacancies give rise to local magnetic moments in graphene sheets. This vacancy-mediated magnetism has renewed the interest on Kondo physics in graphene systems. The Kondo effect is singular in graphene due to its vanishing density of states at low energies, which puts graphene in the class of the so-called pseudogap systems. The pseudogap leads to a Kondo physics that is significantly different than that of the metallic case. There is a recent report on the observation of the Kondo effect in graphene in the literature [1]. However, this result has been contested in favor of a Curie-like paramagnetism persistent down to temperatures as low as 2K [2]. In this cloudy scenario, theory can offer valuable support to elucidate this puzzle.

In this thesis we put forward a theoretical model to address the Kondo effect in graphene with vacancies. We show that disorder plays a central role for the Kondo physics in graphene being the mechanism responsible for the coupling between the local moment created by the vacancy and the conduction band electrons. Our study shows that graphene's nearest neighbors tight-binding Hamiltonian can, upon inclusion of the long-range disorder term, be mapped into a single impurity Anderson-like model. This Anderson Hamiltonian provides the necessary inputs to implement the Numerical Renormalization Group method (NRG), that allows a full characterization of the low-temperature behavior of the system physical properties.

We perform NRG simulations and analyze the system's magnetic susceptibility. We find that disorder "spoils" the pseudogap character of graphene since our results are consistent with those of a "standard" metal. We also use the NRG method to study the distributions of Kondo temperatures $P(T_K)$. We find that the resulting $P(T_K)$ depends on the disorder strength and, in a more subtle manner, on the chemical potential. We show that disorder can lead to long logarithmic tails in $P(T_K)$, consistent with a quantum Griffiths phase, opening the possibility of observation of non-Fermi-liquid behavior in graphene. Finally, we argue that our study can also offer a conciliatory scenario to the contentious experimental results reported in the literature about the low-temperature behavior of local magnetic moments generated by vacancies in graphene.

Resumo

Experimentos recentes encontraram evidências que vacâncias dão origem a momentos magnéticos locais em folhas de grafeno. Este magnetismo mediado por vacâncias renovou o interesse na física de Kondo em grafeno. O efeito Kondo em grafeno é singular devido à sua densidade de estados ir a zero a baixas energias, colocando-o na classe dos chamados sistemas de pseudogap. O pseudogap leva a uma física de Kondo significativamente diferente da de sistemas metálicos. Na literatura, há relato recente de observação do efeito Kondo em grafeno [1]. No entanto, este resultado foi contestado em favor da observação de paramagnetismo do tipo lei de Curie persistente a temperaturas baixas até 2K [2]. Em meio a este cenário controverso, a teoria pode fornecer uma ajuda valiosa para elucidar este problema.

Nesta tese, nós propomos um modelo teórico para tratar o efeito Kondo em grafeno com vacâncias. Nós mostramos que a desordem tem um papel central para a física de Kondo no grafeno, sendo responsável pelo acoplamento entre o momento localizado gerado pela vacância e os elétrons da banda de condução. Nosso estudo mostra que o Hamiltoniano de ligações fortes de primeiros vizinhos do grafeno pode, após inclusão do termo de desordem de longo alcance, ser mapeado num modelo do tipo Anderson de uma impureza. Este modelo de Anderson fornece as entradas necessárias para implementação do método do Grupo de Renormalização Numérico (NRG), que permite uma caracterização completa do comportamento a baixas temperaturas das propriedades físicas do sistema.

Nós realizamos simulações via NRG e analisamos a susceptibilidade magnética do sistema. Deste estudo observamos que a desordem "arruína" o caráter de pseudogap do grafeno pois nossos resultados são consistentes com o esperado para metais "comuns". Também aplicamos o método do NRG para avaliar as distribuições de temperaturas de Kondo $P(T_K)$. Observamos que as distribuições $P(T_K)$ dependem do grau da desordem e, de uma maneira mais sutil, do potencial químico. Mostramos que a desordem pode levar a $P(T_K)$ com caudas logarítmicas longas, consistente com uma fase de Griffiths quântica. Isto abre a possibilidade da observação de comportamento do tipo não líquido de Fermi em grafeno. Finalmente, argumentamos que nosso estudo pode oferecer um cenário conciliatório para os resultados experimentais conflituosos na literatura acerca do comportamento a baixas temperaturas de momentos magnéticos localizados gerados por vacâncias em grafeno.

List of Figures

Contents

1 Introduction

1.1 Introductory remarks on graphene

Less than a decade has elapsed since the realization of the experiment [13], conducted by the Manchester Group headed by Andre Geim and Kostya Novoselov, that first isolated and identified a truly (one-atom-thick) 2D crystal: graphene. This discovery triggered the scientific community to explore the properties of this new material with such an engagement probably never seen before. As a recon for the importance of their pioneering work, Geim and Novoselov were awarded with the 2010 Nobel prize in Physics.

Graphene attracted the attention of the scientific community due to its unique chemical, mechanical, optical, thermal and electronic properties [3, 5, 14, 15, 16, 17, 18, 19, 20, 21, 22, 23, 24, 25]. Many of the promising properties are yet to be explored, but some of the already known aspects are: exquisite chemical sensitivity to foreign molecules [5] and ability to adsorb and desorb various atoms and molecules [15], impermeability to gases [5, 15], breaking strength 200 times greater then steel and the largest tensile strength measured so far [5], flexibility [15], very high thermal and electrical conductivity [3, 5, 15] and transparency [5].

The combination of such superb characteristics into a single material makes graphene a potential candidate to be used in technological applications and has stimulated the interest on graphene across the physics frontiers to disciplinary areas such as chemistry, biology and engineering. Just to mention some possibilities under investigation we have the use in touch screens, e-paper, transistors, photodetectors, solar cells, sensors, tissue-engineering etc [23].

The two questions that naturally rise at this point are: What is graphene? and What makes it so special? It is known since a long date that carbon atoms can combine in different manners forming distinct allotropes. Graphene is a monolayer of carbon atoms tightly packed in a two-dimensional honeycomb lattice and may be thought as a single

layer of graphite (see Fig. 1)[1]

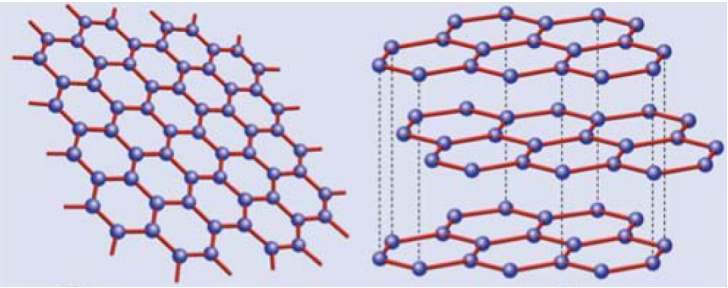

Figure 1: (Left) Graphene honeycomb lattice. (Right) Graphite is composed of stacks of graphene. Adapted from Ref. [3]

The electronic configuration of atomic carbon is $1s^2\ 2s^2\ 2p^2$. Single carbon atoms are extremely unstable and have the natural tendency to combine with other atoms to form more stable structures, such as solids or molecules. In carbon-carbon bonds, the s and p orbitals combine themselves forming the so-called $s-p$ hybridized orbitals [26, 27]. The $1s$ electrons form the core nucleus and constitute a deep valence band, hence the properties of carbon materials are essentially determined by the $2s$ and $2p_x$, $2p_y$ and $2p_z$ orbitals[2] [21]. There are different possibilities of combinations of these orbitals, and this is the reason for the existence of different allotropes with such distinct properties as those found in graphite and diamond, for instance [21, 27]. For the case of graphene, the $2s$ orbital combines with two $2p$'s (generally called p_x and p_y), forming what is called a sp^2 hybridization [27]. These three hybridized orbitals (denominated σ orbitals) form a trigonal planar structure (see Fig. 2a) which, in combination with the same structure of other carbon atoms, form a covalent (σ) bond between carbon atoms separated by $1.42A$ (see Fig. 2b). These bonds are very strong, being responsible for the great robustness of graphene's lattice. The saturation of the resulting σ bonding orbitals leaves an extra p orbital (also denoted π or p_z orbital) which is orthogonal to the planar structure and hosts a single electron. These p-orbitals form a band that is usually considered in theoretical studies of low-energy electronic properties of graphene [3].

As we show below, three ingredients are determinant for the unusual electronic properties of graphene: 2D character, the lattice geometry and the fact that it is composed solely by carbon atoms.

The lattice structure of graphene is shown in Fig. 2b. The honeycomb lattice is not a

[1] This is actually the way it was first obtained, stripped from graphite crystals using scotch tapes [13].

[2] In the presence of other atoms, such as H, O or other C atoms, it is energetically favorable to promote one electron from the $2s$ orbital to one $2p$ orbital in order to form covalent bonds with these atoms.

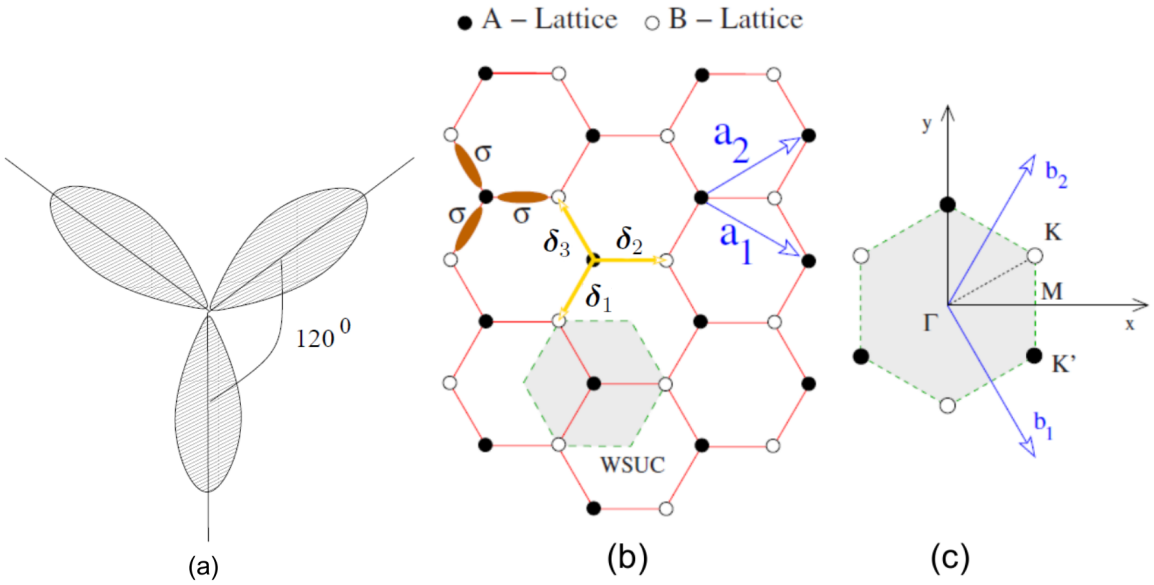

Figure 2: (a) Trigonal planar structure formed by the sp^2 hybridization. (b) Bipartite nature of the graphene lattice also denoted the lattice vectors $\boldsymbol{a}_1$ and $\boldsymbol{a}_2$ and first neighbors vectors $\boldsymbol{\delta}_i$, $i = 1, 2, 3$. (c) Representation of the first Brilloin zone of graphene with the high symmetry points Γ, M, K and K'. Adapted from Ref. [4].

Bravais lattice [28]. Instead, it can be viewed as being composed of two interpenetrating triangular sublattices A and B in such a way that sites of one sublattice have only nearest neighbors of the opposite sublattice. As a consequence, the unit cell has two atoms, one in each sublattice. The primitive vectors are given by $\boldsymbol{a}_1$ and $\boldsymbol{a}_2$. The corresponding first Brillouin zone of the associated reciprocal lattice is displayed in Fig. 2c.

Even though we mentioned that graphene was only experimentally isolated recently [13], a theoretical model to describe the basic electronic properties of graphene was developed a long time ago by Wallace [29], who was interested in studying Graphite's band structure and used graphene as an example to illustrate the model. The electronic structure of graphene is well described by tight binding model for the π electrons. Considering that electrons hop only to nearest neighbors, the model Hamiltonian reads [3]

$$H = -t \sum_{\langle i,j \rangle} \left[a^{\dagger}_{i,\sigma} b_{j,\sigma} + H.c \right] \tag{1.1}$$

where $t \approx 2.8$eV [3] is the hopping integral, $a^{\dagger}_{i,\sigma}$ ($a_{i,\sigma}$) creates (annihilates) an electron with spin σ on site $\boldsymbol{R}_i$ on sublattice A and an analogous definition applies to $b^{\dagger}_{j,\sigma}$ ($b_{j,\sigma}$). The square brackets indicate that the sum is restricted to nearest neighbors only. To take into account the translation symmetry of the lattice, a transformation to the momentum representation is necessary. In this representation the Hamiltonian is written as a 2×2

matrix (due to the two atoms in the unit cell) cast as[3] [25]:

$$H = \begin{pmatrix} 0 & -tS(\mathbf{k}) \\ -tS^*(\mathbf{k}) & 0 \end{pmatrix}, \tag{1.2}$$

where the function $S(\mathbf{k})$ reads [25]:

$$S(\mathbf{k}) = \sum_n e^{i\mathbf{k}\cdot\boldsymbol{\delta}_n}, \quad n = 1, 2, 3, \tag{1.3}$$

where $\boldsymbol{\delta}_n$ denotes the three nearest neighbors vectors (see Fig. 2b).

The simple structure of the Hamiltonian, Eq. 1.2, with null terms in the main diagonal is a consequence that the graphene unit cell possess only identical atoms [4]. This gives a gapless band structure, as we show below.

The diagonalization of Eq. (1.2) leads to the dispersion relation [25]:

$$E_{\pm}(\mathbf{k}) = \pm|t|\sqrt{3 + f(\mathbf{k})}, \tag{1.4}$$

where $f(\boldsymbol{k})$ is [25]:

$$f(\mathbf{k}) = 2\cos\left(\sqrt{3}k_y a\right) + 4\cos\left(\frac{\sqrt{3}}{2}k_y a\right)\cos\left(\frac{3}{2}k_x a\right), \tag{1.5}$$

with $a \approx 1.42$A the lattice parameter.

The result found in Eq. (1.4) shows that the system is particle-hole symmetric, a consequence of the bipartite nature of the lattice [4].

The system is gapless since the valence and conduction band touch each other at six points which correspond to the corners of the Brilloun zone (see Fig. 2c). From these six corners only two $\boldsymbol{K}$ and $\boldsymbol{K'}$ are inequivalent, the others being connected by reciprocal lattice vectors.

The two energy bands are represented in Fig. 3. As there are two π electrons in the unit cell, neutral graphene is half-filled. Due to the characteristics of the bands described above, the low energy physics of the system is determined by the behavior of the dispersion relation close to the Brillouin zone corners. Taylor expanding Eq. (1.4) close to one such

[3] For more details on this calculations see Ref. [27]

[4] If the atoms were not equal, the onsite energies would differ and there would be non-null terms in the main diagonal. A finite term on the main diagonal also appears under consideration of next nearest neighbors, but this effect is considerably smaller [3].

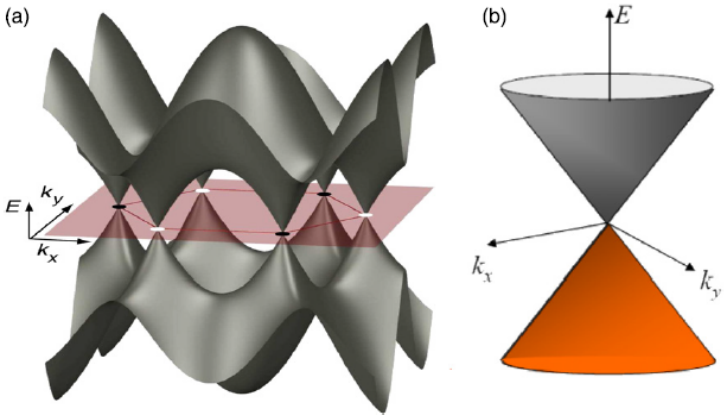

Figure 3: (a) Graphene band structure. (b) Conical relation obtained in the low-energy limit close to the $\boldsymbol{K}$ (or $\boldsymbol{K}'$) point. Extracted from Ref. [5]

point, $\boldsymbol{K}$ for instance[5], one obtains [3]:

$$E_{\pm}(\mathbf{q}) = \pm v_F|\mathbf{q}|, \tag{1.6}$$

where $\boldsymbol{k} = \boldsymbol{K} + \boldsymbol{q}$, $|\mathbf{q}| \ll |\boldsymbol{K}|$ and $\boldsymbol{q}$ is the momentum measured relative to $\boldsymbol{K}$. $v_F = 3ta/2\hbar \approx 10^6$m/s is the Fermi velocity. In Fig. 3b is plotted the band structure close to one of the corners confirming the behavior described by Eq. (1.4).

The result presented by Eq. (1.4) has a striking consequence for the physics of graphene: its low energy spectra is governed by a Dirac-like (relativistic) equation[6] instead of the usual situation, governed by the Schrodinger equation for systems where the energy dispersion is given by a quadratic relation $E(\boldsymbol{k}) = k^2/2m$, with m the electron mass. Hence, the electrons in graphene behave as massless Dirac fermions, but instead of the light velocity c, with a Fermi velocity $v_F \approx c/300$. This has enormous consequences for the observation of phenomena of the realm of QED in graphene. Successfully experiments on graphene have already observed the ocurrence of a minimum in the conductivity when the carriers density tends to zero [14], Klein tunneling (insensitivity of Dirac Fermions to electrostatic potentials barriers) [3], anomalous integer quantum Hall effect [30, 31] which can be observed even at room temperature [32].

Note that since the Dirac points $\boldsymbol{K}$ and $\boldsymbol{K}'$ are inequivalent, the complete description of the electrons of graphene is given by a 4-dimensional spinor, accounting to the

[5] A similar result is found for $\boldsymbol{K}'$.

[6] For this reason, the $\boldsymbol{K}$ and $\boldsymbol{K}'$ points are usually denoted Dirac points (cones). The term valley is also very frequent.

informations respective of each sublattice and "valley", reading [3, 25]:

$$\Psi = \begin{pmatrix} \Psi_A^K \\ \Psi_B^K \\ \Psi_A^{K'} \\ \Psi_B^{K'} \end{pmatrix}, \tag{1.7}$$

where the spin index is omitted since for pristine graphene there is no process distinguishing any spin direction and it enters only as a degeneracy factor.

For pristine graphene, the Dirac Hamiltonian which acts on this spinor has no terms connecting the $\boldsymbol{K}$ and $\boldsymbol{K'}$ valleys [25]:

$$H = \begin{pmatrix} 0 & k_x - ik_y & 0 & 0 \\ k_x + ik_y & 0 & 0 & 0 \\ 0 & 0 & 0 & -k_x + ik_y \\ 0 & 0 & -k_x - ik_y & 0 \end{pmatrix}, \tag{1.8}$$

where in the Hamiltonian Eq. (1.8), the upper (lower) block corresponds to $\boldsymbol{K}$ ($\boldsymbol{K'}$) Dirac point. This particular configuration allows to separate each block and derive two effective reduced Hamiltonians for each valley. Hence the contribution of each valley may be described by a 2-dimensional spinor [3]. This scenario has to be revised under the introduction of mechanisms that generates coupling of the two valleys. A particular case where this happens is the presence of short-range disorder in the system. In this case the full 4-dimensional structure has to be considered [16].

The density of states derived for graphene has also a peculiar form (see Fig. 4). As expected it embodies the particle-hole symmetric character of this system[7]. A remarkable aspect is that, due to the linear dispersion, in the low-energy regime $\rho(\epsilon) \propto |\epsilon|/v_F^2$ [3], hence the density of states vanishes linearly close to charge neutrality ($\epsilon = 0$). This means that pristine graphene is not a metal, since $\rho(\epsilon)$ vanishes for $\epsilon \to 0$, nor an insulator since it possess no band gap. Depending on the community it is called a gapless semiconductor or a semimetal [3]. This state of affairs is crucial for the effects of electron-electron interactions in this system and in particular for the problem we address in this thesis, namely, the Kondo effect in graphene.

[7] Valid when only nearest neighbor interactions are taken into account. Depart from this form due to inclusion of next nearest neighbors interactions may be seen in Fig. 5 of [3].

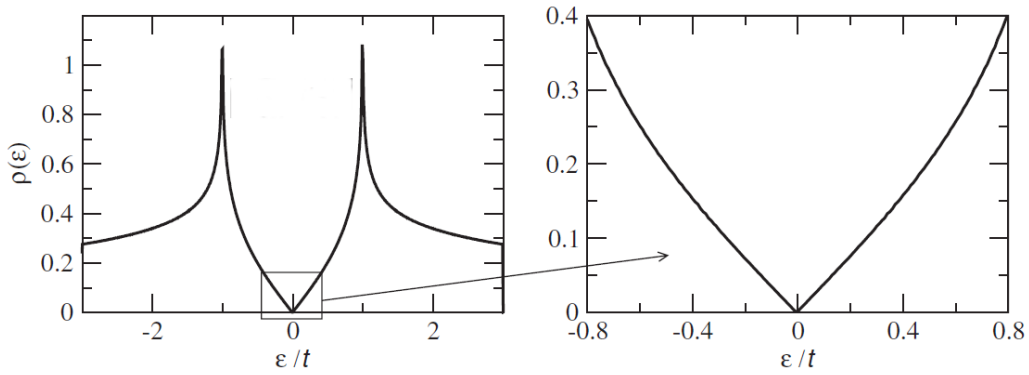

Figure 4: (Left) Graphene density of states. (Right) The region in the inset shows a linear shape as energy goes down to $\epsilon = 0$. Extracted from Ref. [3]

1.2 Introductory remarks on the Kondo effect

The Kondo effect is known to the condensed matter community for many decades. The first experimental observations of its signature remounting back to the 1930's [8]. Contrary to what was expected, it was observed that by cooling down a piece of a metal the resistivity decreased monotonically until a certain temperature, where it reached a minimum. Chilling below this point however produced an increase in the resistivity until a saturation at a finite value. Later it was discovered that the occurrence of such phenomenon was connected to the presence of very diluted magnetic impurities in the metal host[8]. Since most of the early experiments dealt with very diluted concentrations of impurities in the host metal, to a first approximation, the latter do not interact with each other, hence the phenomenon can be essentially considered as due to a single magnetic impurity in a metal. By a magnetic impurity we mean any atom with an unfilled shell, so that unpaired electrons form a magnetic moment [33]. Experimentally, the effect of these localized moments show up as a Curie-like contribution to the magnetic susceptibility, but answering the questions of how this localized moment survives in the metallic environment and how this affect the conduction electrons of the metal took decades to be developed [8].

A complete understanding of the Kondo effect in metallic systems was only accomplished fifty years after its first experimental observation. On the theoretical side, contributions of P. W. Anderson, J. Kondo and K. Wilson were essential for the construction of a complete solution to the problem. In chronological order, to mention some of these outstanding contributions, we can cite the theoretical modelling derived by Anderson that

[8] A few parts per million of iron in gold, for instance [33].

was able to establish the conditions whether a magnetic impurity immersed in a metal "remains" magnetic or not [34]; Kondo's perturbative approach that accounted for the minimum of the resistivity observed in the experiments [35]; Wilson's development of the numerical renormalization group (NRG) scheme, responsible for the full characterization of the low-temperature physical properties of the system [36].

The heuristic picture that emerges from the theory and explains the puzzle has in its origin the fact that atoms with unpaired electrons tend to form bonds or spin singlets in order to spread their electrons over a larger region of space and minimize their kinetic energy [33]. As mentioned above, impurities in the system were ideally so diluted that they do not interact. In this case, the way the impurity finds to form the bond is via the surrounding conduction electrons. The picture here is slightly different then bonding in molecules such as H_2 where the two electrons are localized. Here only the electron impurity is localized and the initially delocalized conduction electrons have to somehow localize forming a strongly correlated state through an energy-cost process to originate the "bond". As an outcome of this process, the bond is rather weak and only appears at very low temperatures[9] (tens of Kelvin [33]). Electronic transport is severely influenced when a bond is formed since the conduction electrons take part on it. In this case, a conduction electron passing by the impurity will not be simply scattered in a new direction and give as a by-product an increase in the resistivity. Now, these conduction electrons will have to take part in the bond during an amount of time before being scattered in a new random direction [33]. Hence, at sufficiently low temperatures, when the "bond" is well developed the resistivity stops to rise and saturates at a new level. In this point the conduction electrons "quench" (are paired with) the local moment of the impurity and the Curie signature in the magnetic susceptibility disappears.

1.3 Kondo effect in graphene

The vanishing density of states at the charge neutrality point puts graphene in a class of systems denoted as pseudogap systems [37]. Kondo physics in these systems reveals new aspects such as the presence of quantum critical behavior [38]. Depletion of conduction electrons at very low energies may lead to a failure in the bond formation between the conduction electrons and the impurity. In this situation the localized spin remains unquenched down to extremely low temperatures [37, 38]. Pseudogap Kondo physics has been extensively studied [38], but its physical realization was generally addressed in the

[9] Compare for instance the case of bonds in molecules, where they are stable even at room temperature.

context of d-wave superconductors [37, 38]. Graphene, besides offering another platform of realization of pseudogap Kondo effect, has the advantage of having additional handle with respect to the superconductors. Since graphene can easily be doped (by electrons or holes) [13], it allows the possibility of study how Kondo physics is affected by the tuning of a chemical potential [39].

Intense theoretical activity on the study of magnetic impurities in graphene and their consequences for the Kondo effect has increased recently [11, 17, 39, 40, 41, 42, 43, 44, 45, 46]. The conditions necessary for the presence of localized magnetic moments on adatoms with inner shell electrons in graphene are established in Ref. [40]. Interestingly, it is pointed out that in graphene the formation of localized magnetic moments can be controlled by an electric field [40]. Analysis of Kondo physics shows interesting results such as gate-dependent critical coupling J_c [41, 42] and Kondo temperature T_K [11, 44]. Despite the theoretical advances on the Kondo effect in graphene due to magnetic adatoms, the literature contains scarce experimental material on this issue. The only published experimental work, so far, makes use of a scanning tunnelling microscope to manipulate[10] and probe Co adatoms on the graphene sheet deposited on an insulating SiO_2 substrate. However, a clear-cut signature of the Kondo effect is not observed in the experiment [48]. Interestingly, the emergence of magnetism associated with defects are detected in this study [48].

In general, magnetism is associated to systems with d or f electrons. However, the possibility of magnetism with p electrons has been pointed out in carbon systems due to the presence of defects or edge effects [49]. Defect-induced magnetism in graphene provides other interesting route for exploration of the Kondo effect rather than magnetic atoms. One such kind of defect is a vacancy. A vacancy occurs when an atom is removed from the sheet. This action results in the formation of local moments which were predicted theoretically [50, 51, 49, 52] and the onset of vacancy magnetism confirmed by experiments [1, 2, 53, 54]. The interaction between these vacancy-induced local moments with graphene conduction electrons can lead to the Kondo effect. In this scenario, experimental observation of the Kondo effect in graphene has been reported [1].

[10] This route was successfully adopted to address the Kondo effect in metallic systems [39, 47].

1.4 Outline

In this thesis we give a theoretical approach to the problem of the Kondo effect in graphene arising from vacancies. The remaining of this work is separated in four parts. In Chapter 2 we present in some detail the experiment that served as a motivation to this work. In Chapter 3 the background for a theoretical approach to the Kondo effect is constructed. We introduce the Anderson and Kondo models [8] and discuss the main results and ideas derived by these authors for the Kondo effect in metallic systems. A schematics of the NRG method developed by Wilson [10, 36, 55] is conducted. We end the chapter discussing the physics of pseudogap systems making a comparative study between the differences with the metallic case and address some theoretical results developed for the Kondo effect in graphene. Chapter 4 presents our theoretical modelling to the problem of the Kondo effect in graphene showing how disorder plays a key part in this process. Finally, in Chapter 5 we bring our conclusions.

2 Experimental Motivation

The Kondo effect has been recently observed in graphene by the Maryland group [1]. The experiment consists of the bombardment of a graphene sheet, deposited on SiO_2, with 500eV He^+ in ultra-high vacuum. The process originates vacancies in graphene. The resistivity $\varrho(V_g, T)$ of the irradiated samples was analized as a function of gate voltage V_g and temperature T. The authors claim that $\varrho(V_g, T)$ shows a temperature-dependent contribution $\varrho_K(V_g, T)$ which follows the universal dependence expected for spin-1/2 single parameter Kondo scattering. Below we review in more detail the experiment and its main findings.

Repeating sample preparation of a previous work [56], graphene deposited over SiO_2 was irradiated with 500eV He^+ in ultra-high vacuum (UHV) at low temperature. Afterwards the sample was annealed overnight at 490K and air exposed during transfer to an ^{3}He cryostat. The conductivity $\sigma(V_g)$ was measured before and after sample irradiation (but before annealing) at $T = 17$K, and after the annealing at $T = 300$mK. Figure 5 shows the curves obtained. The estimated mobilities in each of these stages were, respectively: 4000, 300 and 2000cm^{2}V^{-1}s^{-1}. Due to disorder, the irradiated sample shows a lower mobility than the pristine one. But what is the nature of the defects caused by irradiation? The experimental evidence for defect mediated intervalley scattering is the observation of a D band peak in the Raman spectra presented after annealing and air exposure, see Fig. 6. This is evidence of short range scattering, which could be a vacancy, a larger damaged region or a Stone-Wales defect (a kind of local reconstruction) [16].

Another evidence of short range disorder in the irradiated sample comes from the study of weak localization (WL) which manifest in the observation of the sample magnetoresistance (see below). One important aspect about short range scattering is that it may cause localization. The interaction of localized states with the band conduction electrons is key to understand the Kondo physics. An appropriate model to deal with the scattering of conduction electrons by a localized state is the so-called Anderson model, and in the next sections we will present the ideas behind this model and the numerical renor-

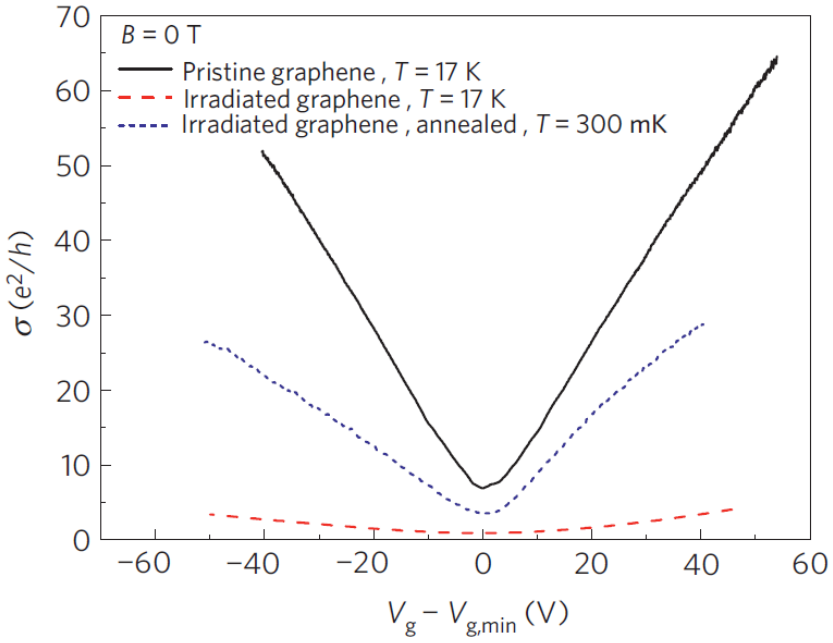

Figure 5: $\sigma(V_g)$ of graphene sample before He^+ irradiation (black solid line), after irradiation (red dashed line) and after annealing at $T = 490$K (blue short-dashed line). Extracted from Ref. [1].

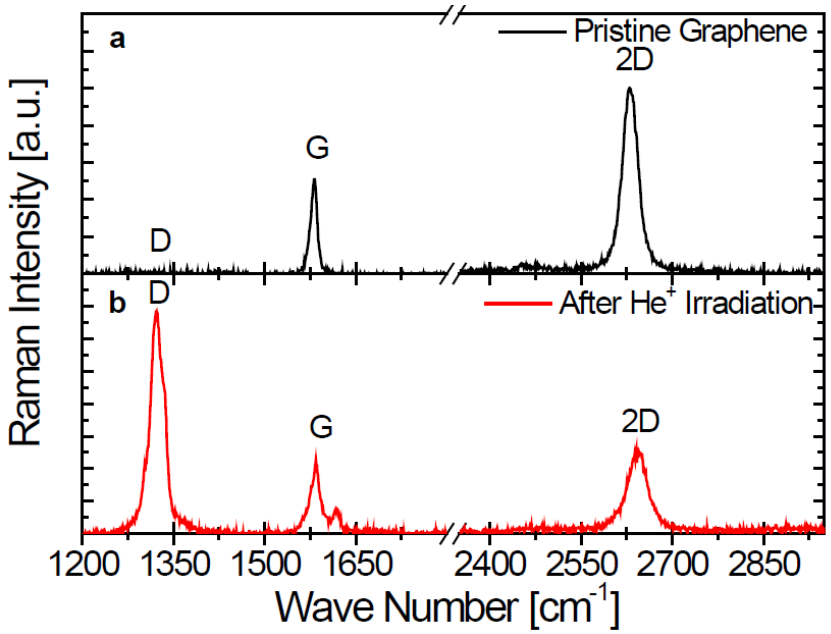

Figure 6: Raman expectra before **a** and after **b** irradion of graphene with He^+. Extracted from Ref. [1].

malization group (NRG) technique, another tool of major importance in the theoretical understanding of the Kondo effect.

The influence of the perpendicular magnetic field on the resistivity $\varrho(B)$ of the irra-

diated sample was investigated at $T = 300$mK and different gate levels, see Fig. 7 (top). Weak localization is observed at small B fields. This influence is best seen in Fig. 7 (bottom) which displays a detail of the magnetoresistance at small B at $T = 300$mK and $V_g - V_{g,min} = -65$V [1]. One should note that for fields close to $B = 1$T, weak localization is suppressed. At higher fields, the authors claim that SdH oscillations were also observed. Then, their strategy to skip the effects of WL and SdH oscillations was to measure the resistivity $\varrho(V_g, T)$ under a perpendicular magnetic field equal to $B = 1$T, large enough to dissipate the effect of WL but not so large for Shubnikov-de Haas (SdH) oscillations to manifest.

A strong experimental evidence for the Kondo effect is a logarithmic dependence of $\varrho(V_g, T)$ on T, hence the resistivity $\varrho(V_g, T)$ was measured as a function of temperature for different gate voltages while $B = 1$T, see Fig. 8. The authors [1] claim that in the region of temperatures close to 200K and beyond, phonon contributions become significant and positive $d\varrho/dT$ are seen[2] in the resistivities curves for V_g not to near $V_{g,min}$. However, for temperatures in the range of $10 - 100$K the derivative becomes negative and the resistivity follows a logarithmic increase as temperature is lowered. For even lower temperatures resistivity saturates.

The measured $\varrho(V_g, T)$ was compared with the expressions developed in theories of the "metallic" Kondo effect [57, 58]. For low temperatures (up to 10K) the data should obey the Fermi liquid behavior whose theory predicts the expression [57]:

$$\varrho(V_g, T) = \varrho_{c1}(V_g) + \varrho_{K,0}(V_g) \left[1 - \left(\frac{\pi}{2} \right)^4 \left(\frac{T}{T_K(V_g)} \right)^2 \right]. \tag{2.1}$$

At the intermediate temperature regime (from 10 to $\sim 100K$) where the logarithmic behavior presents, the derived expression is [58]:

$$\varrho(V_g, T) = \varrho_{c2}(V_g) + \frac{\varrho_{K,0}(V_g)}{2} \left[1 - 0.470 \ln \left(\frac{1.2T}{T_K(V_g)} \right) \right]. \tag{2.2}$$

In Eqs. (2.1) and (2.2) ϱ_{K0} is the Kondo resistivity at zero temperature, ϱ_{c1} and ϱ_{c2} are the resistivity temperature-independent contribution and T_K is the Kondo temperature. If the resistivity follows the universal Kondo form, $\varrho_{c1} = \varrho_{c2}$. This fact was explored in the paper to test the model consistency. Since $\varrho(V_g, T = 0)$ is known from the data, Eqs. (2.1) and (2.2) have actually three degrees of freedom for each V_g: ϱ_{c1}, ϱ_{c2} and T_K. The

[1] $V_{g,min}$ is the gate voltage at which the conductivity has a minimum. The encountered values were 8V, 5V and 5.3V; for pristine, irradiated and annealed graphene, respectively.

[2] This is better visualized in Fig. 10 bottom.

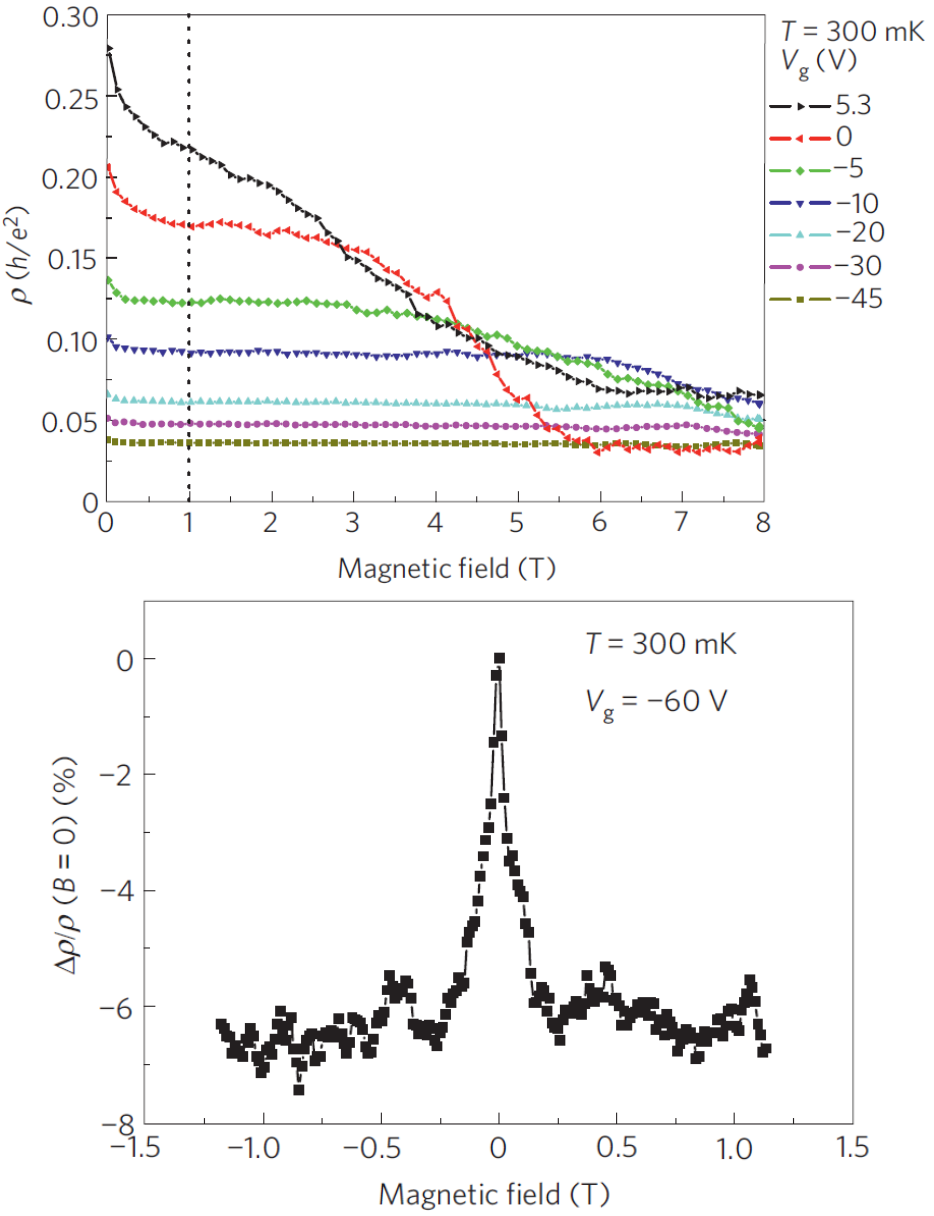

Figure 7: Top: Magnetoresistance as a function of perpendicular magnetic field for several dopings V_g for irradiated and annealed graphene. Bottom: Effect of the weak localization at small fields displayed in the magnetoresistance of the irradiated and annealed sample at $V_g - V_{g,min} \approx -65$V and $T = 300$mK. Extracted from Ref. [1].

remaining parameters were then estimated via a least squares fit to Eqs. (2.1) and (2.2). In Fig. 9 is presented the adjusted parameters, on the top are displayed the results for ϱ_{c1} and ϱ_{c2} and on the bottom the data for the Kondo resistivity subtracted by ϱ_{c1}. The behavior in the two plots is similar exhibiting a maximum near $V_g = 5.3$V, where the conductivity has a minimum. One can see that the agreement of the adjusted parameters ϱ_{c1} and ϱ_{c2} is very good supporting the conclusion that the logarithmic divergence and T^2 saturation originates from the same phenomenon: the Kondo effect.

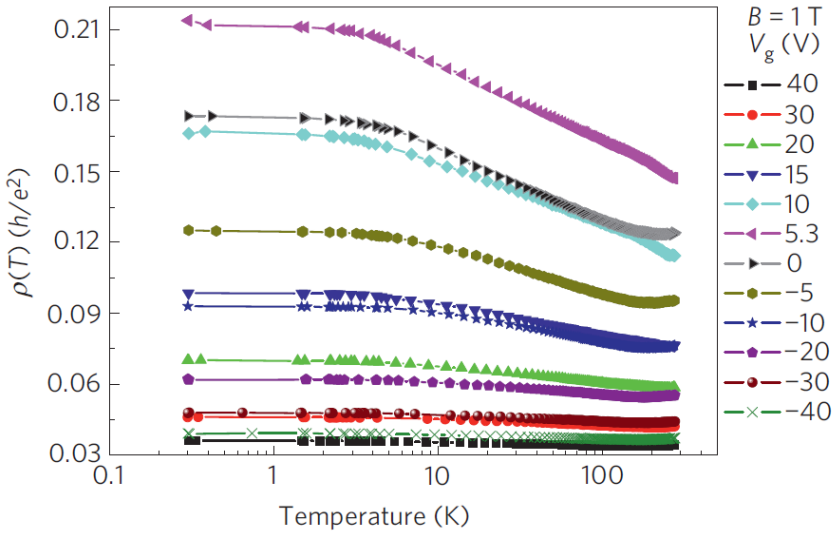

Figure 8: $\varrho(V_g, T)$ for different doping levels and perpendicular field equal to $B = 1$T. Extracted from Ref. [1].

The dependence of the estimated Kondo temperatures on the gate voltage is displayed in Fig. 10. The curve in black corresponds to data from the sample (Q6) from which were obtained the data discussed above. The blue curve was obtained from the analysis of another sample (L2). In both curves we observe similar aspects as: the gate dependency of T_K, which is slightly particle-hole asymmetric; minimum T_K occurring close to the minimum of conductivity and high values of T_K (of order 50K). The slightly lower values of T_K found in sample L2 were speculated as coming from two factors [1]: 1) after annealing the temperature base measurement of sample L2 was $T = 1.7$K against $T = 0.3$K for sample Q6. It was argued that the higher base measurement could result in smaller T_K estimates for each V_g as was observed for sample L2. 2) The second possibility pointed was disorder, which vary from sample to sample and could also influence the estimates.

Finally, the $\varrho(V_g, T)$ curves of Fig. 8 were scaled by the calculated parameters ϱ_{c1}, ϱ_{K0} and T_K, and the outcomes were compared to theoretical results calculated using the NRG method [58]. In Fig. 10 is plotted the normalized resistivity $(\varrho(V_g, T) - \varrho_{c1})/\varrho_{K0}$ versus renormalized temperature T/T_K for the different sets of curves of Fig. 8. The data collapse is very nice for the range between $0.003 < T/T_K \lesssim 3$. The match between the NRG curve and the experimental data is very impressive, indicating a very robust Kondo effect. In the range of temperatures where the data depart from the theoretical curve, phonon contributions should manifest which would increase the resistivity explaining the positive deviation for the higher fillings. On the other hand, the negative deviation encountered for lower fillings could be an effect of thermal activation of carriers [1].

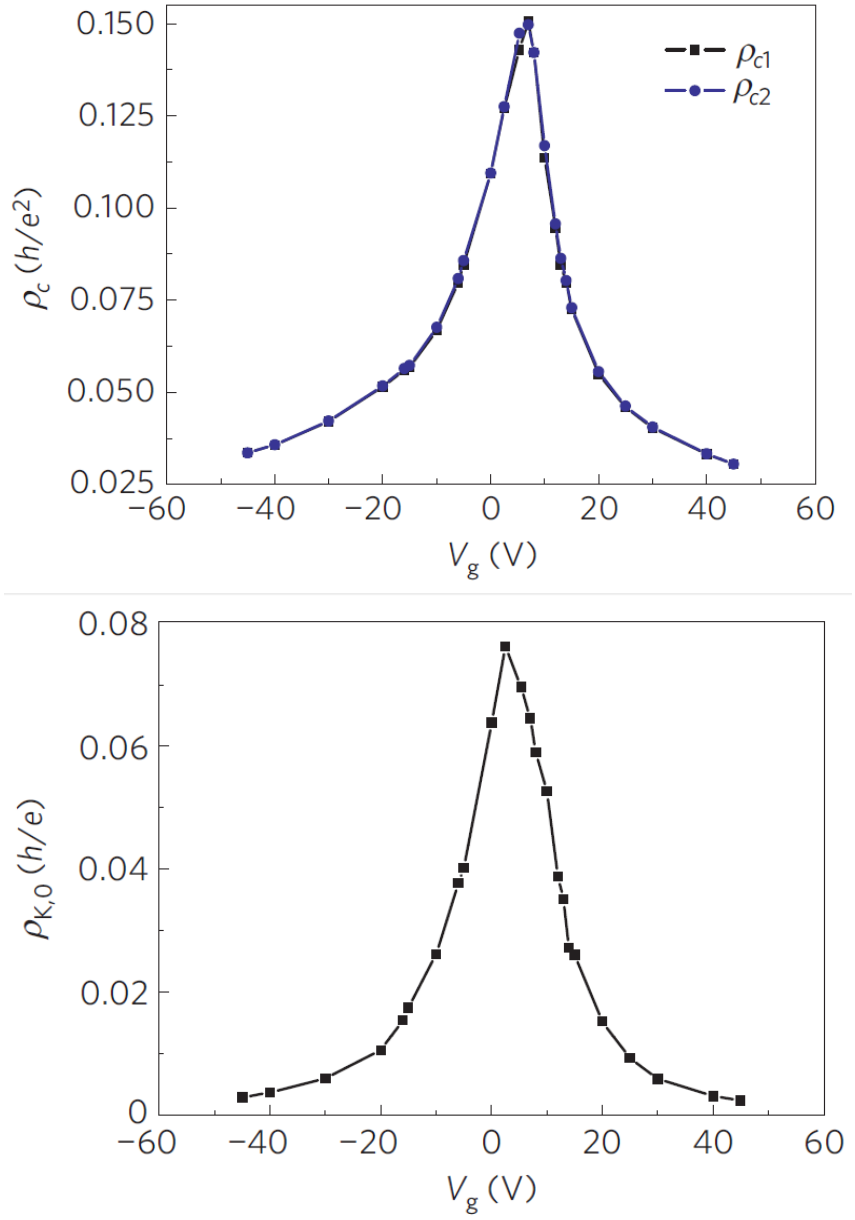

Figure 9: Top: Estimates of ϱ_{c1} and ϱ_{c2} obtained from least squares fits of Eqs. (2.1) and (2.2) at different doping levels V_g. Bottom: Estimates of zero temperature resistivity ϱ_{K0} at several V_g. Extracted from Ref. [1].

It is quite surprising that the experimental data fits so well a metallic Kondo theory. As we mentioned earlier, systems which have a density of states that vanishes at the Fermi level as $\varrho(\epsilon) \propto |\epsilon|^n$ are known as pseudogap systems. Graphene belongs to this class, $n = 1$ is expected in this case. The Kondo effect exhibited for pseudogaped systems differs substantially in many aspects by that presented in metallic systems which have a constant density of states [38]. This puzzle might be attributed to disorder which could be responsible for the "conversion" of graphene into a standard metal. In a later chapter we

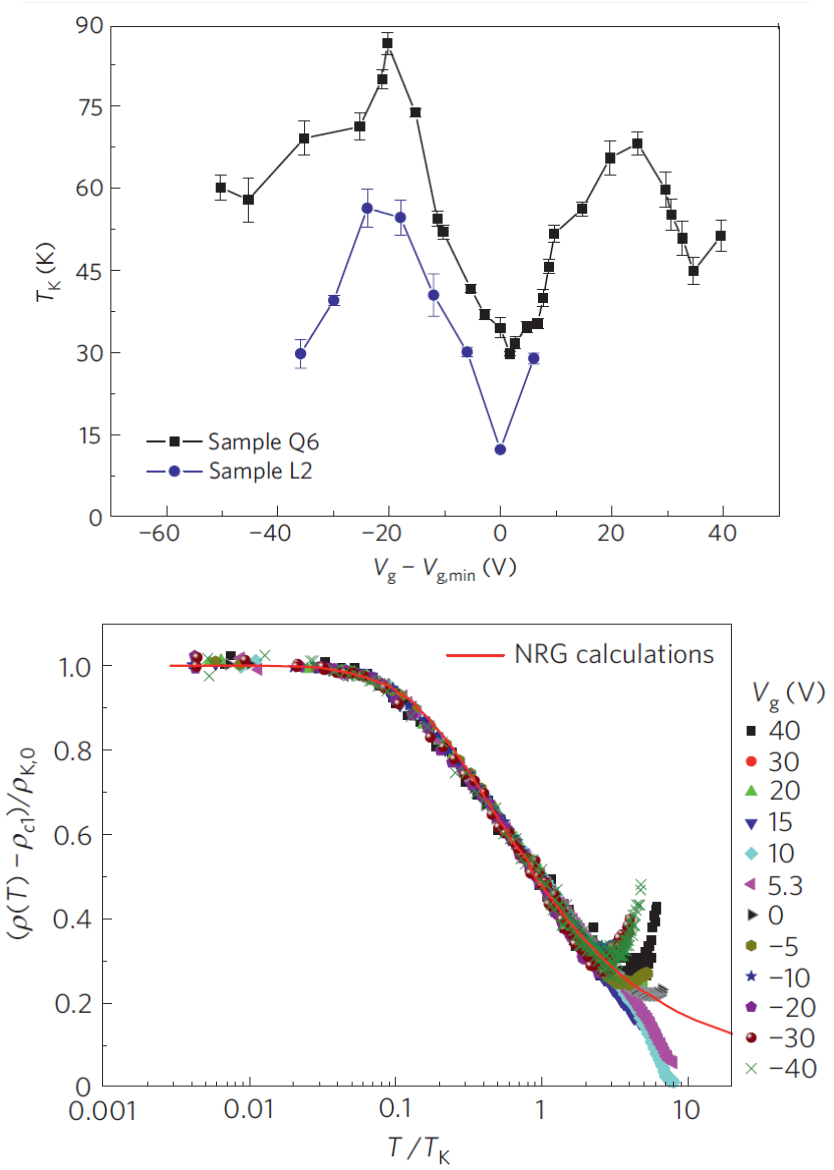

Figure 10: Top: Kondo temperatures estimated from least squares fits for two samples, Q6 (the one to which all the others analysis refer) and L2. Bottom: Comparison between scaled resistivity curves with the parameters adjusted for each V_g and theoretical result from NRG calculations. Extracted from Ref. [1].

will explore this influence and try to understand until what extent disorder is responsible for such "conversion".

Although the data is fitted by a "metallic" Kondo Theory, the predicted relation

$$k_B T_K \approx D e^{-1/J\varrho(\epsilon_F)}, \tag{2.3}$$

(where k_B is Boltzmann's constant, D the bandwidth, J the coupling constant between the localized state and conduction electrons, $\varrho(\epsilon_F)$ the metal's density of states at the

Fermi energy) which is valid for metals, fails in predicting the estimate of T_K at zero doping, which for neutral graphene implies $T_K = 0$ since it's density of states vanishes at the Dirac point. Another interesting aspect of Eq. (2.3) and the temperatures displayed in Fig. 10 is that temperatures $\sim 50K$ would imply a very strong coupling J between the localized state and the conduction electrons since the density of states is very small close to the Dirac point.

The interpretation of the logarithmic resistivity as a manifestation of Kondo effect has been contested [59]. It was argued that actually the logarithmic resistivity was due to electron-electron interactions in the presence of disorder [59, 60], which would cause the Altshueler-Aronov effect. The hypothesis of the Altshueler-Aronov effect was pointed in the Kondo experiment [1], but it was ruled out trough the argument that the Altshueler-Aronov effect should be present even at high fields, and that would imply in corrections to Hall coefficients which they did not observe [1]. This explanation was also contested by Jobst et al [59] who argued that universal conductance fluctuations or non-ideal alignment of the Hall leads could obscure the interpretation of the Hall data from Ref. [1]. Chen et al finally keep the interpretation of the Kondo effect as the correct explanation of the logarithmic resistivity by showing that the Altshuler-Aronov theory fails in overestimating their observed magnetoresistance and in the predictions of the saturation temperature of the resistivity [61].

We finish this section emphasising that the discussed experiment serves as a motivation for the model we use to study the Kondo effect in disordered graphene. Our goal is to provide qualitative understanding of the data. A quantitative analysis would involve a better knowledge of the defects in the sample, and, more importantly the description of a disordered Kondo lattice. This is beyond the scope of this study.

3 Theoretical Background on the Kondo effect

3.1 Anderson Model: Mean Field Solution

One of the prototype models for describing microscopically the interaction between a localized magnetic moment and a bath of conduction electrons is the so-called Anderson model, proposed by P. W. Anderson in 1961 [34]. This model shed light on an important question in condensed matter physics, namely: a metallic atom immersed in a nonmagnetic metallic host would still remain magnetic?

The Anderson model has very few elements. The conduction electrons of the host are represented by a band whose single-particle energies, measured with respect to the Fermi sea, are given by $\epsilon_{\mathbf{k}}$. The impurity is treated simply as a local single electronic orbital with an energy ϵ_d. Orbital degeneracy, typical of metallic five-fold degenerate impurities (Fe, for instance) is not considered. The additional ingredients of the model are the charging energy U, which is the cost for double occupancy of the localized orbital of the impurity due to the electrons Coulomb interaction, and the coupling matrix element $\gamma_{\mathbf{k}d}$, responsible for electrons of the conduction band hop into the impurity orbital and vice-versa. The model Hamiltonian reads [6]:

$$H_A = \sum_{\mathbf{k},\sigma} \epsilon_{\mathbf{k}} c^{\dagger}_{\mathbf{k}\sigma} c_{\mathbf{k}\sigma} + \sum_{\sigma} \epsilon_d c^{\dagger}_{d\sigma} c_{d\sigma} + \sum_{\mathbf{k},\sigma} (\gamma_{\mathbf{k}d} c^{\dagger}_{\mathbf{k}\sigma} c_{d\sigma} + \gamma^{*}_{\mathbf{k}d} c^{\dagger}_{d\sigma} c_{\mathbf{k}\sigma}) + U n_{d\uparrow} n_{d\downarrow}, \tag{3.1}$$

where, in Eq. (3.1), $c^{\dagger}_{\mathbf{k}\sigma}$ ($c_{\mathbf{k}\sigma}$) creates (destroys) electrons with spin σ in the conduction band and $c^{\dagger}_{d\sigma}$ ($c_{d\sigma}$) creates (destroys) electrons with spin σ in the impurity. $n_{d\sigma} = c^{\dagger}_{d\sigma} c_{d\sigma}$ is the number operator for a localized electron with spin σ.

Despite its simplicity, Eq. (3.1) poses a non-trivial many-body problem. The solution relies, for instance, in the numerical renormalization group method developed by [10, 36, 55], which we will describe in a future section.

In order to extract insightful physics from Eq. (3.1), Anderson made use of a mean field (or Hartree-Fock) approximation, namely [6]:

$$Un_{d\uparrow}n_{d\downarrow} \approx U\left\langle n_{d\uparrow}\right\rangle n_{d\downarrow} + Un_{d\uparrow}\left\langle n_{d\downarrow}\right\rangle . \tag{3.2}$$

The approximated Hamiltonian reads [6]:

$$H_A^{HF} = \sum_{\mathbf{k},\sigma} \epsilon_{\mathbf{k}} c_{\mathbf{k}\sigma}^{\dagger} c_{\mathbf{k}\sigma} + \sum_{\sigma} E_{d\sigma} c_{d\sigma}^{\dagger} c_{d\sigma} + \sum_{\mathbf{k},\sigma} (\gamma_{\mathbf{k}d} c_{\mathbf{k}\sigma}^{\dagger} c_{d\sigma} + \gamma_{\mathbf{k}d}^{*} c_{d\sigma}^{\dagger} c_{\mathbf{k}\sigma}), \tag{3.3}$$

where the impurity energy is renormalized as [6]

$$E_{d\sigma} = \epsilon_d + U\left\langle n_{d-\sigma}\right\rangle . \tag{3.4}$$

Here we will sketch the most important results obtained by the mean field solution. The complete derivation can be found in [6, 34].

By means of the Hartree-Fock approximation, the Anderson Hamiltonian is bilinear in the localized and band operators, therefore it can be diagonalized by an unitary transformation [6]:

$$c_{n\sigma}^{\dagger} = \sum_{\mathbf{k}} \langle n\sigma|\mathbf{k}\sigma\rangle c_{\mathbf{k}\sigma}^{\dagger} + \langle n\sigma|d\sigma\rangle c_{d\sigma}^{\dagger}, \tag{3.5}$$

$|d\sigma\rangle$ and $|\mathbf{k}\sigma\rangle$ are impurity and conduction states, respectively, and $|n\sigma\rangle$ denotes the states in the diagonal basis. In the eigenstates basis, the Hamiltonian can be written as a single-particle term [6]:

$$H_A^{HF} = \sum_{n\sigma} \epsilon_{n\sigma} c_{n\sigma}^{\dagger} c_{n\sigma}. \tag{3.6}$$

The single-particle energy levels $\epsilon_{n\sigma}$ can be determined through the equations of motion for operators.

The most important quantity required to understand the local moment formation is the net occupancy of the impurity states per spin [6]:

$$\langle n_{d\sigma}\rangle = \sum_{\epsilon_{n\sigma}\leq\epsilon_F} |\langle n\sigma|d\sigma\rangle|^2 = \int_{-\infty}^{\epsilon_F} d\epsilon \rho_{d\sigma}(\epsilon), \tag{3.7}$$

where $|\langle n\sigma|d\sigma\rangle|^2$ is the overlap probability of the system eigenstates with the impurity site, ϵ_F is the Fermi energy, and $\rho_{d\sigma}$ denotes the impurity density of states, that is [6]

$$\rho_{d\sigma}(\epsilon) = \sum_{n} \delta(\epsilon_{n\sigma} - \epsilon)|\langle n\sigma|d\sigma\rangle|^2. \tag{3.8}$$

Local moment will arise as long as $\langle n_{d\sigma}\rangle \neq \langle n_{d-\sigma}\rangle$. To establish whether this condition

is satisfied, the impurity density of states can be calculated through the impurity's Green function [6]:

$$\rho_{d\sigma}(\epsilon) = -\frac{1}{\pi}\lim_{\eta\to 0}\mathrm{Im}\, G^{\sigma}_{dd}(\epsilon + i\eta). \tag{3.9}$$

For the single-particle Hamiltonian H_A^{HF}, the matrix elements of G obey the relation [6]:

$$\sum_{\beta}(\epsilon + i\eta - H_A^{HF})_{\alpha\beta}G_{\beta\mu}(\epsilon + i\eta) = \delta_{\alpha\mu}. \tag{3.10}$$

Collecting terms in Eq. (3.10) and solving the resulting equations for G^{σ}_{dd} results [6]:

$$G^{\sigma}_{dd}(\epsilon + i\eta) = \left[\epsilon + i\eta - E_{d\sigma} - \sum_{\mathbf{k}}\frac{|\gamma_{\mathbf{k}d}|^2}{\epsilon + i\eta - \epsilon_{\mathbf{k}\sigma}}\right]^{-1}. \tag{3.11}$$

Rewriting the summation term in Eq. (3.11) as [6]

$$\sum_{\mathbf{k}}\frac{|\gamma_{\mathbf{k}d}|^2}{\epsilon + i\eta - \epsilon_{\mathbf{k}\sigma}} = \sum_{\mathbf{k}}|\gamma_{\mathbf{k}d}|^2\frac{\epsilon - \epsilon_{\mathbf{k}} - i\eta}{(\epsilon - \epsilon_{\mathbf{k}})^2 + \eta^2}, \tag{3.12}$$

and taking the limit $\eta \to 0$ [6]:

$$\lim_{\eta\to 0}\sum_{\mathbf{k}}\frac{|\gamma_{\mathbf{k}d}|^2}{\epsilon + i\eta - \epsilon_{\mathbf{k}\sigma}} = P\left(\sum_{\mathbf{k}}\frac{|\gamma_{\mathbf{k}d}|^2}{\epsilon - \epsilon_{\mathbf{k}}}\right) - i\pi\sum_{\mathbf{k}}|\gamma_{\mathbf{k}d}|^2\delta(\epsilon - \epsilon_{\mathbf{k}}). \tag{3.13}$$

The first term in Eq. (3.13) is the principal value of the function under parentheses and is a real quantity, therefore entailing a shift of the impurity energy level. For a constant density of states, which is a good model for the metallic host, in the range of variation of $E_{d\sigma}$ the fluctuation caused by this term is small, allowing it to be discarded [6]. The second term is a relevant contribution and $\pi\sum_{\mathbf{k}}|\gamma_{\mathbf{k}d}|^2\delta(\epsilon - \epsilon_{\mathbf{k}}) = \Gamma$ is denoted as the hybridization function. Its relevance transcends the mean field solution of the Anderson model, being of major importance in the implementation of the NRG method structure.

In the present context the hybridization function is responsible for a broadening of the impurity's level, which can be seen more clearly if we insert the result Eq. (3.13) back into Eq. (3.11) [6]:

$$G^{\sigma}_{dd}(\epsilon + i\eta) = \frac{1}{\epsilon + i\eta - E_{d\sigma} + i\Gamma}. \tag{3.14}$$

Finally, inserting result Eq. (3.14) into Eq. (3.9) we find [6]:

$$\rho_{d\sigma}(\epsilon) = \frac{1}{\pi}\frac{\Gamma}{(\epsilon - E_{d\sigma})^2 + (\Gamma)^2}. \tag{3.15}$$

Equation (3.15) is a Lorentzian distribution whose width is controlled by the parameter Γ. It should be noticed that in the limit of $\Gamma \to 0$ (no hybridization), Eq. (3.15)

approaches a Dirac δ-function. The effect of hybridization is now quite clear: when the hybridization is absent, the impurity states are eigenstates of the Hamiltonian separated by the charging energy U. One can then associate an infinite lifetime to this state. Once the hybridization is turned on, the effect of mixing is that the impurity states are no longer eigenstates, so an electron at one of these states will acquire a finite lifetime τ to decay into other states, this decay will be faster the larger is Γ, which can be established more rigorously through Fermi's golden rule resulting the relation $\tau = \hbar/2\Gamma$ [6].

The mean occupation per spin is evaluated as [6]:

$$\langle n_{d\sigma} \rangle = \int_{-\infty}^{\epsilon_F} d\epsilon \rho_{d\sigma}(\epsilon) = \frac{1}{\pi} \text{arccot} \left(\frac{E_{d\sigma}}{\Gamma} \right), \tag{3.16}$$

but, since $E_{d\sigma} = \epsilon_d + U\langle n_{d-\sigma} \rangle$ it follows that [6]:

$$\cot \left(\pi \langle n_{d\sigma} \rangle \right) = \frac{\epsilon_d + U\langle n_{d-\sigma} \rangle}{\Gamma}. \tag{3.17}$$

The pair of coupled equations (one for each σ) Eq. (3.16) defines the parameter regime at which the system will exhibit magnetic solutions. As expected, for $U = 0$ the system is nonmagnetic, since $\langle n_{d\uparrow} \rangle = \langle n_{d\downarrow} \rangle$. This is also the case for an infinite hybridization $\Gamma \to \infty$ which results in $\langle n_{d\uparrow} \rangle = \langle n_{d\downarrow} \rangle = 1/2$. As shown in Fig. 11, a magnetic regime is expected for the case in which the impurity lies below the Fermi energy $\epsilon_d < \epsilon_F$ (so that in thermal equilibrium the impurity will be at least singly occupied) and, besides, that the cost of doubly occupying the impurity exceeds the Fermi energy $\epsilon_d + U > \epsilon_F$ which inhibits the double occupation. The phase diagram for the complete range of magnetic parameters is displayed in Fig. 12, where use of the transformed dimensionless variables $x = -\epsilon_d/U$ and $y = U/\Gamma$ have been adopted. The points $x = 0$ and $x = 1$ are the limits for the magnetic region since $x = 0$ corresponds to $\epsilon_d = \epsilon_F = 0$ and $x = 1$ to $\epsilon_d + U = \epsilon_F = 0$. The most favorable case for magnetism to emerge is $x = 1/2$.

It should be noticed that the magnetic limit is valid in the range within which the impurity is weakly coupled to the electron gas and the charging energy is large $U/\Gamma \gg 1$. In such a limit the system presents only spin fluctuations, charge fluctuations are vanishing small. This spin dynamics was explored by Kondo in a famous study of the scattering of conduction electrons by a magnetic impurity [35] that we discuss in the following. In appendix A we show that, in the magnetic limit, the Anderson model can be mapped into the model analyzed by Kondo.

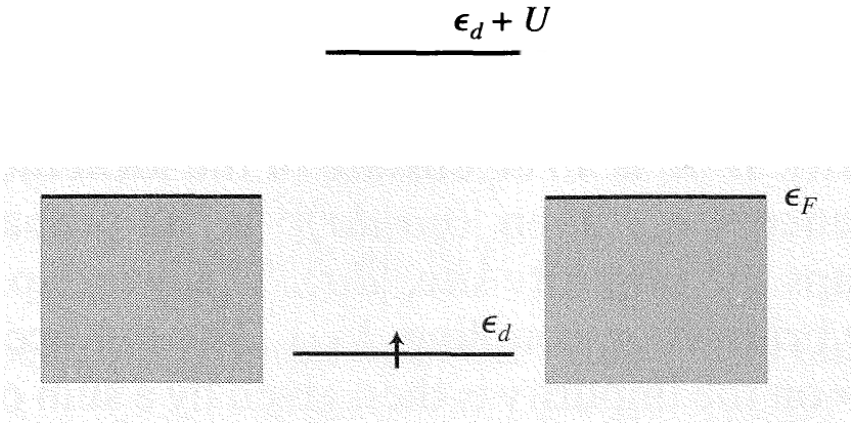

Figure 11: Schematics of the energy levels of the Anderson model in the magnetic case. Extracted from Ref. [6].

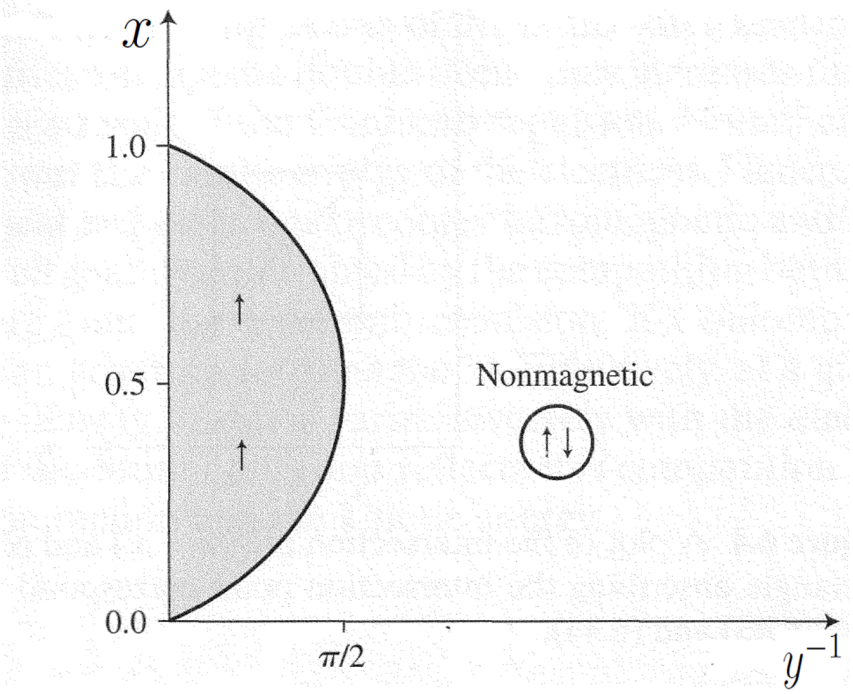

Figure 12: Phase diagram for the mean field solution of the Anderson model. Extracted from Ref. [6].

3.2 Kondo effect and Kondo problem

In his seminal paper [35], Kondo was interested in studying how the low temperature resistivity and magnetic properties of a host metal are affected by a magnetic impurity. He was motivated by experimental results due to Sarachick et al [7] who made a series of measurements of the resistivities of $Mo - Nb$ alloys containing Fe impurities. The

experimental data of the alloys resistivities is shown in Fig. 13. The measurements show that the resistivities decrease logarithmically as the temperature is lowered until they reach a minimum. When the temperature is reduced even more, the resistivity inverts its behavior and starts to grow (logarithmically) reaching a finite value. This result is in strong contrast to the resistivity of a pure metal that tends to zero monotonically as the temperature decreases [6].

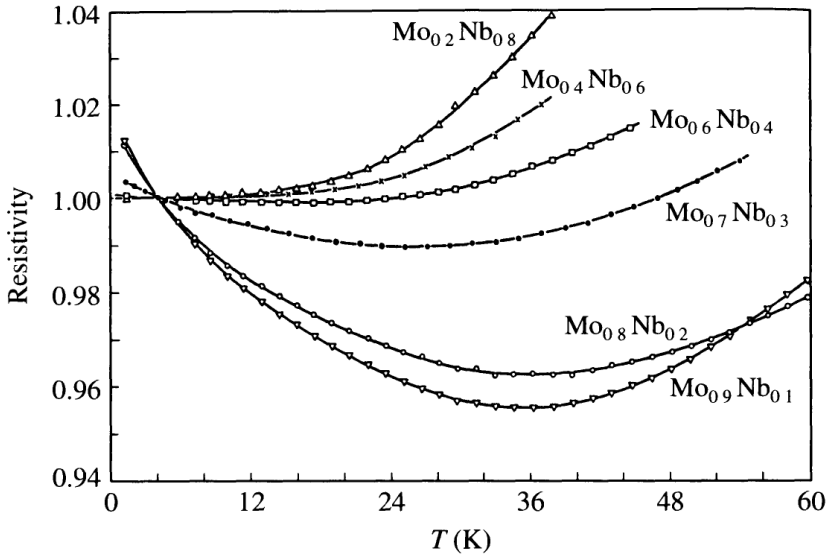

Figure 13: Resistance measurements for Fe in a series of $Mo-Nb$ alloys. Extracted from Ref. [7].

Kondo explored the interaction of the localized moment with the conduction electrons through the so-called Kondo (or s-d) Hamiltonian [8]:

$$H_K = -\frac{J}{\hbar}\sum_{\mathbf{k}\mathbf{k}'}\left[S^+ c^\dagger_{\mathbf{k}\downarrow}c_{\mathbf{k}'\uparrow} + S^- c^\dagger_{\mathbf{k}\uparrow}c_{\mathbf{k}'\downarrow} + S_z\left(c^\dagger_{\mathbf{k}\uparrow}c_{\mathbf{k}'\uparrow} - c^\dagger_{\mathbf{k}\downarrow}c_{\mathbf{k}'\downarrow}\right)\right], \tag{3.18}$$

where S^+ (S^-) denotes the raising (lowering) spin operator of the impurity and S_z is the z component of the impurity spin operator. $c^\dagger_{\mathbf{k}\sigma}$ ($c_{\mathbf{k}\sigma}$) creates (annihilates) a conduction electron in the state $\mathbf{k}$ with spin σ. J denotes the coupling between the impurity and conduction electrons. Besides, the simplification of a $\mathbf{k}$ independent interaction is assumed.

The Hamiltonian Eq. (3.18) describes the interaction of an impurity with an internal spin degree of freedom with the conduction electrons of the host. As we will present in the sequence, this setting involves the integration of the whole Fermi distribution in the scattering calculations of the conduction electrons by the impurity. The scattering problem therefore turns into a true many-body problem, with all electrons entering the

theory trough the Fermi function [62]. This is in marked contrast to the problem of electron scattering by nonmagnetic impurities, where the Fermi distribution does not appear in the calculations and the computation of the scattering cross section is a purely one-electron scattering one. This explains why Drude could construct a successful theory of electrical conductivity before the advent of quantum mechanics since the occurrence of the Fermi distribution is a consequence of Pauli's exclusion principle, which is a hallmark of quantum mechanics.

Kondo explained the connection between the existence of magnetic impurities and the occurrence of the resistance minimum calculating the scattering probability of the conduction electrons to second order[1] in the parameter J (H_K is treated as a perturbation to the conduction electrons Hamiltonian). To this order the logarithmic behavior of the resistivity appears as a consequence of the spin degrees of freedom of the impurity.

The calculation of the resistivity involves the knowledge of the elements of the $T(\epsilon^+)$ matrix, which is defined as [8]:

$$T\left(\epsilon^+\right) = H_{int} + H_{int}G_0^+H_{int} + H_{int}G_0^+H_{int}G_0^+H_{int} + \ldots, \tag{3.19}$$

where $\epsilon^+ = \epsilon + i\eta$ and G_0 denotes the Green function of the non-interacting system. Transport properties are obtained through the Boltzmann equation formalism which relates the inverse transport time and the T matrix through [8]:

$$\frac{1}{\tau(k)} = 2\pi c_{imp}\int \delta(\epsilon_k - \epsilon_{k'})|T_{\mathbf{k}\mathbf{k}'}|^2(1-\cos\theta')\frac{d\mathbf{k}'}{(2\pi)^3}, \tag{3.20}$$

where $\tau(k)$ denotes the transport time, c_{imp} is the impurity concentration, $T_{\mathbf{k}\mathbf{k}'}$ is the T matrix elements between the initial $\mathbf{k}$ and the final state $\mathbf{k}'$ and θ' is the angle between $\mathbf{k}$ and $\mathbf{k}'$. Access to the conductivity (resistivity) is given by [8]:

$$\sigma = \frac{ne^2\tau(k_F)}{m}, \tag{3.21}$$

where n is the number of electrons per unit volume, e the electron charge and m the electron mass.

To first order, $T\left(\epsilon^+\right) = H_{int} = H_K$. Calculating, for instance, the matrix element $\langle \mathbf{k}' \uparrow |T(\epsilon^+)|\mathbf{k} \uparrow\rangle_{(1)}$ (the subindex 1 denotes that this is a first order process) we obtain [8]:

$$\langle \mathbf{k}' \uparrow |T(\epsilon^+)|\mathbf{k} \uparrow\rangle_{(1)} = -\frac{JS_z}{\hbar}. \tag{3.22}$$

[1] Third order in the conductivity [8].

With similar terms for $\langle \mathbf{k}' \uparrow |T(\epsilon^+)|\mathbf{k} \downarrow\rangle_{(1)}$, $\langle \mathbf{k}' \downarrow |T(\epsilon^+)|\mathbf{k} \uparrow\rangle_{(1)}$ and $\langle \mathbf{k}' \downarrow |T(\epsilon^+)|\mathbf{k} \downarrow\rangle_{(1)}$, with S_z in Eq. (3.22) replaced by S^+, S^- and $-S_z$, respectively.

Collecting the above results and substituting into Eqs. (3.20) and (3.21), one obtains a temperature independent contribution to the resistivity, namely [8]:

$$\varrho_0 = \frac{3\pi m J^2 S\,(S+1)\,c_{imp}}{2e^2\hbar\epsilon_F}, \tag{3.23}$$

where use of the relation $2S_z^2 + S^+S^- + S^-S^+ = \hbar^2 S(S+1)$ has been made. S is the total spin of the impurity.

The extension of scattering calculations to second order Born approximation requires calculation of the matrix elements [8]:

$$\langle \mathbf{k}'\sigma'|H_K \frac{1}{\epsilon + i\eta - H_0} H_K|\mathbf{k}\sigma\rangle, \tag{3.24}$$

where $\mathbf{k}\sigma$ ($\mathbf{k}'\sigma'$) labels the conduction electrons initial (final) states.

Among all possible different process represented by Eq. (3.24), the most important terms are those in which the spins of the conduction and localized electrons are flipped during the scattering process. As we show below those terms are responsible for the rise of a temperature dependence of the resistivity. The diagrams representing these processes are displayed in Fig. 14 for the case in which the initial and final electron spin states are up.

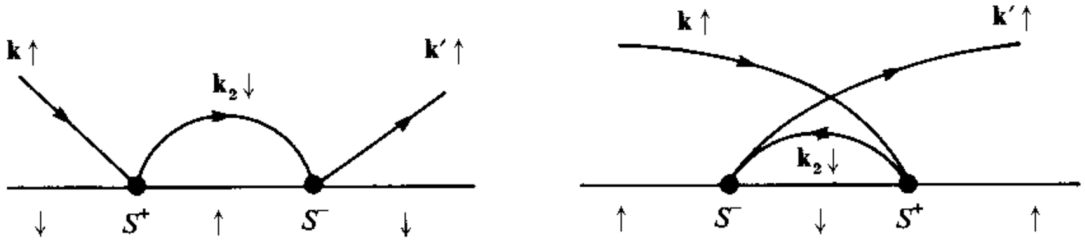

Figure 14: Spin flip diagrams for the second order scattering process in which the initial electron state is $\mathbf{k} \uparrow$ and the final is $\mathbf{k}' \uparrow$. The curved lines represents the electron and the straight line the impurity. In the left panel the intermediate state is an electron while in the right it is a hole, which is represented by the backward arrow. Extracted from Ref. [8].

In the scattering process represented in the left panel of Fig. 14, the $\mathbf{k} \uparrow$ conduction electron is first scattered into the unoccupied state $\mathbf{k}_2 \downarrow$ with a corresponding spin flip of the impurity. In the following, the electron is scattered with spin flip into the final state $\mathbf{k}'$ flipping the spin impurity again. This contribution to the element $\langle \mathbf{k}' \uparrow |T\,(\epsilon^+)\,|\mathbf{k} \uparrow\rangle_{(2)}$

(the subindex 2 denotes that this is a second order contribution) is written as [8]:

$$\frac{J^2}{\hbar^2}\sum_{\mathbf{k}_1,\mathbf{k}_1',\mathbf{k}_2,\mathbf{k}_2'}\langle\mathbf{k}'\uparrow|S^-c^\dagger_{\mathbf{k}_1\uparrow}c_{\mathbf{k}_1'\downarrow}\frac{1}{\epsilon+i\eta-H_0}S^+c^\dagger_{\mathbf{k}_2\downarrow}c_{\mathbf{k}_2'\uparrow}|\mathbf{k}\uparrow\rangle. \tag{3.25}$$

After some algebra this term reduces to [8]:

$$\frac{J^2}{\hbar^2}\sum_{\mathbf{k}_2}S^-S^+\frac{1-f\left(\epsilon_{\mathbf{k}_2}\right)}{\epsilon+i\eta-\epsilon_{\mathbf{k}_2}}. \tag{3.26}$$

In Eq. (3.26) the function $f\left(\epsilon_{\mathbf{k}_2}\right)$ is the Fermi distribution and the factor $1-f\left(\epsilon_{\mathbf{k}_2}\right)$ guarantees that the intermediate state is unoccupied.

The diagram in the right of Fig. 14 represents the second main scattering process. In this situation, an occupied state $\mathbf{k}_2\downarrow$ is scattered with spin flip into the final state $\mathbf{k}'\uparrow$ leaving a hole state behind, which is the reason why the $\mathbf{k}_2$ state is represented by a backward arrow in the diagram. In the sequence the $\mathbf{k}\uparrow$ initial state scatters into the $\mathbf{k}_2\downarrow$ state with a corresponding spin flip of the impurity. This process contributes to $\langle\mathbf{k}'\uparrow|T\left(\epsilon^+\right)|\mathbf{k}\uparrow\rangle_{(2)}$ through the term [8]:

$$\frac{J^2}{\hbar^2}\sum_{\mathbf{k}_2}S^+S^-\frac{f\left(\epsilon_{\mathbf{k}_2}\right)}{\epsilon+i\eta-\epsilon_{\mathbf{k}_2}}. \tag{3.27}$$

Now one notes the presence of the factor $f\left(\epsilon_{\mathbf{k}_2}\right)$ which accounts for the fact that the intermediate state should be occupied in this processes. The order in which the lowering and raising operators spin operators appear in Eq. (3.27) are opposite to the one in Eq. (3.26) reflecting the inversion in the order at which the impurity spin is lowered or raised in the two diagrams. Since S^+ and S^- do not commute, one shows that summing the terms in Eq. (3.26) and Eq. (3.27) results in a term which is still dependent on the Fermi distribution, namely:

$$\frac{J^2}{\hbar^2}S^2\sum_{\mathbf{k}_2}\frac{1}{\epsilon+i\eta-\epsilon_{\mathbf{k}_2}}+2\frac{J^2}{\hbar^2}S_z\sum_{\mathbf{k}_2}\frac{f\left(\epsilon_{\mathbf{k}_2}\right)-1/2}{\epsilon+i\eta-\epsilon_{\mathbf{k}_2}}. \tag{3.28}$$

In the derivation of Eq. 3.28, we made use of the relations $S^+S^-=S^-S^++2S_z$ and $S^-S^+=\hbar^2S^2-S_z^2-S_z$.

We now see that the appearance of the Fermi distribution is a result of the spin degree of freedom of the impurity since it is a consequence of the difference in the sequence of the S operators acting on the impurity states and the creation of particle intermediate states. The many-body aspects, which enter through the Fermi function, imply that all electrons contribute to the scattering matrix of a given conduction electron.

Collecting the first and the second order terms from the perturbative calculations, for the process where the initial and final conduction states have spin up, results [8]:

$$\langle \mathbf{k}' \uparrow | T\left(\epsilon^{+}\right) | \mathbf{k} \uparrow \rangle = -S_z \frac{J}{\hbar}\left[1 - 2\frac{J}{\hbar} g\left(\epsilon\right)\right], \tag{3.29}$$

where in passing from Eq. (3.28) to Eq. (3.29) only the temperature dependent term was retained. The other term can be neglected as its contribution corresponds to correction factors of order J/ϵ_F or higher to the resistivity [8], which are negligible in the standard physical situations corresponding to $J \ll \epsilon_F$. The function $g\left(\epsilon\right)$ reads [62]:

$$g\left(\epsilon\right) = \sum_{\mathbf{k}} \frac{f\left(\epsilon_{\mathbf{k}}\right) - 1/2}{\epsilon + i\eta - \epsilon_{\mathbf{k}}}. \tag{3.30}$$

When squaring expression Eq. (3.29) only the real part of $g(\epsilon)$ remains. This reads [62]:

$$\frac{\rho_0}{2} P \int_{-D}^{D} dx \frac{\tanh\left(\beta x/2\right)}{x - \epsilon} = \rho_0 \ln\left(\frac{D}{k_B T}\right), \tag{3.31}$$

where ρ_0 is a constant density of states and D is the bandwidth.

Calculating the other T-matrix elements $\langle \mathbf{k}' \downarrow | T\left(\epsilon^{+}\right) | \mathbf{k} \uparrow \rangle$, $\langle \mathbf{k}' \uparrow | T\left(\epsilon^{+}\right) | \mathbf{k} \downarrow \rangle$ and $\langle \mathbf{k}' \downarrow | T\left(\epsilon^{+}\right) | \mathbf{k} \downarrow \rangle$ results in terms similar to that found in Eq. (3.29), but with S_z substituted by S^{-}, S^{+} and $-S_z$, respectively. Collecting all these contributions, the resistivity to third order in J is given by [8]:

$$\varrho = \varrho_0 \left[1 + 4J\rho_0 \ln\left(k_B T/D\right)\right]. \tag{3.32}$$

Eq. (3.32) shows how the logarithmic dependence on the temperature emerges. In Eq. (3.32) ϱ_0 is the first order contribution encountered in Eq. (3.23). As opposed to the phonon contribution, the resistivity due to the impurity increases as the temperature is decreased for an antiferromagnetic coupling ($J < 0$). Combining the phonon contribution to the resistivity to the one due to the impurity, Kondo proposed a phenomenological expression for the total resistivity of the form [8]:

$$\varrho(T) = aT^5 + c_{imp} R_0 - c_{imp} R_1 \ln\left(k_B T/D\right), \tag{3.33}$$

where, a, R_0 and R_1 are positive constants, c_{imp} is the impurity concentration and the first term accounts for the phonons contribution and the remaining are the impurity contributions calculated above. Equation (3.33) has a minimum at a temperature T_{min}

and is given by [6]:

$$T_{min} = \left(\frac{R_1}{5a}\right)^{1/5} c_{imp}^{1/5}. \tag{3.34}$$

This is the main result derived by Kondo, who showed that this result fits the experimental observation nicely [35]. Because this successful explanation of the minimum of the resistivity in metallic alloys, this phenomenon was named the *Kondo Effect*[2].

However, the Kondo perturbative approach does not entirely solve the problem. Contrary to what is observed in the experiments (see Fig. 13), the resistivity predicted in Eq. (3.33) diverges logarithmically as temperature tends to zero. The search for a solution valid at low temperatures is the so-called *Kondo Problem*.

3.3 Poor Man's scaling

An important contribution for the understanding of this problem is the *poor man's scaling* analysis put forward by Anderson in the context of the Kondo[3] model [64].

It is expected that at low temperatures only those states close in energy to the Fermi level will be determinant for the system physical properties. The goal of the scaling analysis is to eliminate the high-energy excitations in a sequence of steps and describe the system within a limited region of the energy spectrum close to the Fermi level in such a way that the effect of the high-energy excitations is absorbed as a renormalization of the coupling terms of an effective Hamiltonian representing the "reduced" system.

For the implementation of the scaling proceeding, the method considers a band of width $2D$, centered at the Fermi energy ($\epsilon_F = 0$), and step-by-step reduces the cut-off energy D to $D - |\delta D|$, eliminating particle states lying at the upper band edge or holes in the lower band edges (see Fig. 15). These high-energy excitations are mapped into intermediate states in perturbation theory. Anderson carried the calculations up to second order in perturbation theory which is the reason of the name poor man's scaling [6]. The basic idea is to consider the scattering processes that enter in the second order transition amplitude and to determine how they change when the bandwidth is decreased by the amount $|\delta D|$. As result, the effect of the elimination of high-energy states is absorbed by a renormalization of the coupling constants of the reduced system. The poor man's scaling gives a set of equations relating the original couplings to those of the new system.

[2] In the literature this designation is also used to designate the quenching of the local moment by the conduction electrons.

[3] The approach was later developed for the Anderson single-impurity model by Haldane [8, 63]

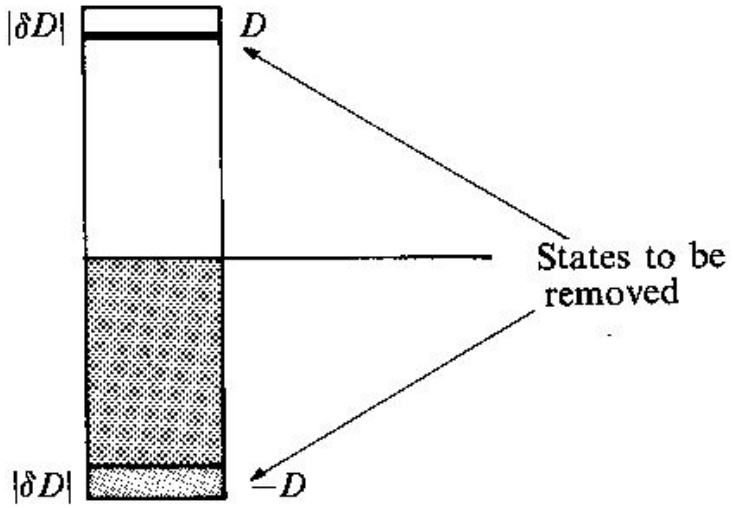

Figure 15: Schematics of the states that will be eliminated in the scaling procedure. Extracted from Ref. [8].

The starting point of the method considers the Kondo Hamiltonian with anisotropic exchange couplings [8]:

$$H' = H_K = -\frac{1}{\hbar^2}\sum_{\mathbf{k}\mathbf{k}'}\left[J_+ S^+ c^\dagger_{\mathbf{k}\downarrow}c_{\mathbf{k}'\uparrow} + J_- S^- c^\dagger_{\mathbf{k}\uparrow}c_{\mathbf{k}'\downarrow} + J_z S_z\left(c^\dagger_{\mathbf{k}\uparrow}c_{\mathbf{k}'\uparrow} - c^\dagger_{\mathbf{k}\downarrow}c_{\mathbf{k}'\downarrow}\right)\right]. \quad (3.35)$$

The diagrams representing the scattering process of conduction electrons into the band edges are essentially the same as those treated above in the calculations of the elements of the T matrix $\langle \mathbf{k}\sigma|T(\epsilon^+)|\mathbf{k}'\sigma'\rangle$ (see Fig. 14).

Considering first the scattering process of Fig. 16i, where a conduction electron $\mathbf{k}$ with spin up is scattered into the intermediate[4] state $\mathbf{q}\downarrow$ in the upper band edge and then to a final state $\mathbf{k}'\uparrow$, the contribution, to lowest order correction in H', of this diagram to the scattering process is given by [8]:

$$\frac{J_+ J_-}{\hbar^2}\sum_{\mathbf{q}} S^- c_{\mathbf{k}'\uparrow}c_{\mathbf{q}\downarrow}\left(E - H_0\right)^{-1}\sum_{\mathbf{q}'} S^+ c_{\mathbf{q}'\downarrow}c_{\mathbf{k}\uparrow}, \quad (3.36)$$

where H_0 is a single-particle conduction electron Hamiltonian.

Considering that the band edge state is unoccupied in the initial and final states, it implies that $c_{\mathbf{q}\downarrow}c^\dagger_{\mathbf{q}'\downarrow} = \delta_{\mathbf{q},\mathbf{q}'}$. With this in mind and remembering that the summations in $\mathbf{q}$ in Eq. (3.36) are restricted to states within an energy $|\delta D|$ of the band edge, after some

[4]The intermediate state is represented by a dashed line because this is the high-energy state which will be eliminated in the scaling process.

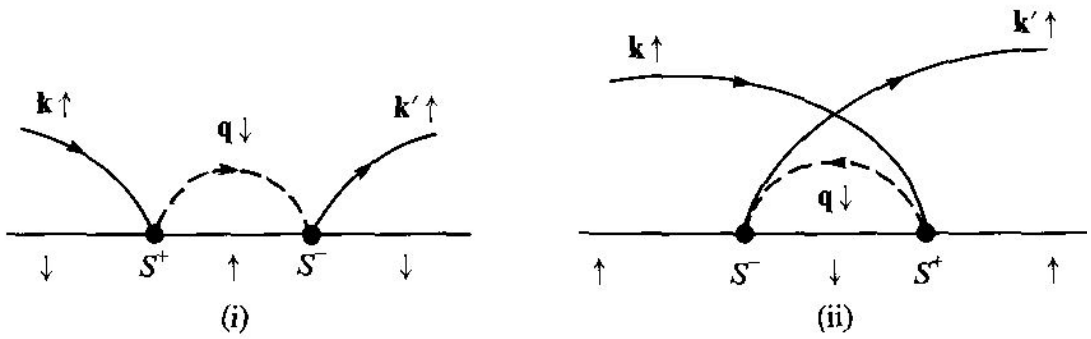

Figure 16: Two-spin-flip process in which particle (i) and hole (ii) high-energy excited states will be eliminated (dashed lines). Extracted from Ref. [8].

lengthy algebra (for more details see Ref. [6]) Eq. (3.36) can be cast in the form [8]:

$$\frac{J_+J_-}{\hbar^2}\rho_0|\delta D|\left(\frac{\hbar^2}{2}-\hbar S_z\right)c^\dagger_{\mathbf{k}\uparrow}c_{\mathbf{k}'\uparrow}\left(E-D+\epsilon_{\mathbf{k}}\right)^{-1}, \tag{3.37}$$

where ρ_0 is a constant density of states and use of the relation $S^-S^+ = \hbar^2/2 - \hbar S_z$ has been made.

The diagram in Fig. 16ii represents the scattering process in which the intermediate state to be eliminated is a hole state within a energy range δD of the bottom of the band $-D$. Similar approximations as those conducted above leads to the expression [8]:

$$\frac{J_+J_-}{\hbar^2}\rho_0|\delta D|\left(\frac{\hbar^2}{2}+\hbar S_z\right)c_{\mathbf{k}'\uparrow}c^\dagger_{\mathbf{k}\uparrow}\left(E-D-\epsilon_{\mathbf{k}'}\right)^{-1}, \tag{3.38}$$

where the identity $S^+S^- = \hbar^2/2 + \hbar S_z$ is used in deriving the result in Eq. (3.38).

Similar contributions arise when considering two-spin-flip process in which the initial and final states have spin down. One may see that Eqs. (3.37) and (3.38) have the same[5] structure as the longitudinal term in Eq. (3.35), hence elimination of high energy states through the process above leads to a renormalization of the longitudinal coupling given by $J_z \to J_z + \delta J_z$ where [8]:

$$\delta J_z = J_+J_-\rho_0|\delta D|\left[\frac{1}{E-D+\epsilon_{\mathbf{k}}}+\frac{1}{E-D-\epsilon_{\mathbf{k}'}}\right]. \tag{3.39}$$

Similarly, one obtains a renormalization of the transverse couplings when eliminating high-energy excitations through one-spin-flip process (see Fig. 17, for instance). Collecting the contributions from those kind of scattering process leads to a renormalization of

[5]The spin independent terms give rise to a scattering potential and a term responsible for shift the ground state energy. The former is discarded since its magnitude is small close to the Fermi energy. The latter is incorporated into H_0 in the scaling process [64]

the transverse couplings given by [8]:

$$\delta J_{\pm} = J_{\pm} J_z \rho_0 |\delta D| \left[\frac{1}{E - D + \epsilon_{\mathbf{k}}} + \frac{1}{E - D - \epsilon_{\mathbf{k}'}} \right]. \tag{3.40}$$

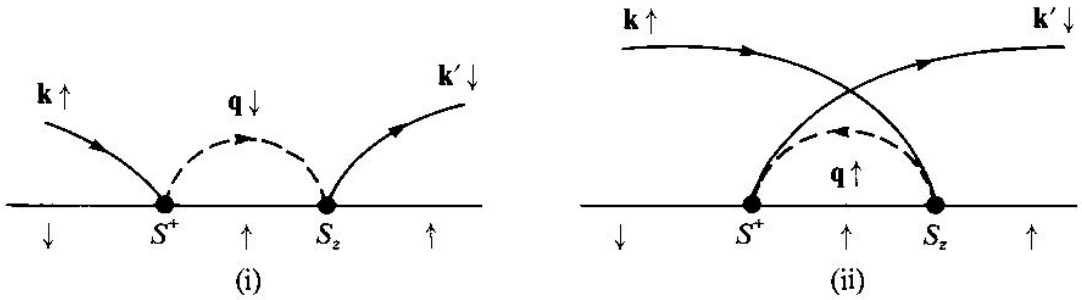

Figure 17: One-spin-flip process in which particle (i) and hole (ii) high-energy excited states will be eliminated (dashed lines). These process contribute to the renormalization of the transverse couplings. Extracted from Ref. [8].

Considering excitations low in energy with respect to D, and for scattering of conduction electrons near the Fermi level, Eqs. (3.39) and (3.40) can be written as [8]:

$$\frac{dJ_{\pm}}{d\ln D} = 2\rho_0 J_z J_{\pm} \quad \text{and} \quad \frac{dJ_z}{d\ln D} = 2\rho_0 J_{\pm}^2, \tag{3.41}$$

where we set $J_+ = J_- = J_{\pm}$ [6, 8].

The most important result of the scaling process is obtained through the solution of this pair of coupled equations which gives a family of hyperbolic curves [8]

$$J_z^2 - J_{\pm}^2 = \kappa, \tag{3.42}$$

with κ a constant.

Substituting Eq. (3.42) in the scaling equation for $J_{\pm}$ clarifies the interpretation of the results [6]:

$$\frac{dJ_{\pm}}{d|\ln D|} = \begin{cases} -2\rho_0 J_{\pm}\sqrt{\kappa + J_{\pm}^2} & \text{for} \quad J_z > 0 \quad \text{(ferromagnetic)}, \\ 2\rho_0 J_{\pm}\sqrt{\kappa + J_{\pm}^2} & \text{for} \quad J_z < 0 \quad \text{(antiferromagnetic)}. \end{cases} \tag{3.43}$$

Thus we see that for the ferromagnetic case the effect of scaling is to reduce the strength of the effective transverse coupling, meaning that $J_{\pm}$ flows to zero in this case. For the antiferromagnetic situation the opposite occurs and the renormalized couplings increase in magnitude as the scaling procedure is performed until $|J_{\pm}| \to \infty$ where the perturbative approach breaks down. This is the strong coupling regime in which the

Kondo effect occurs. This scaling analysis is illustrated in the diagram of Fig. 18.

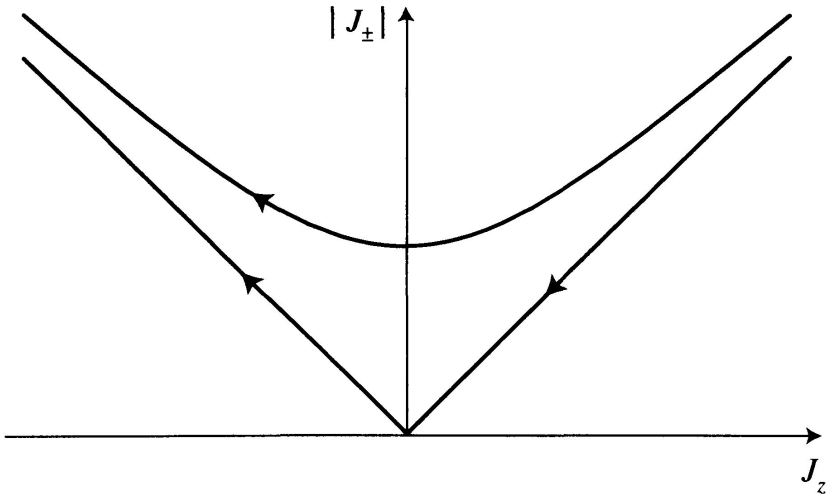

Figure 18: Scaling diagram obtained by the poor man's scaling. The straight line represents the situation in which coupling is isotropic. For positive coupling J_z (ferromagnetic case) the couplings renormalizes to zero while for $J_z < 0$ (antiferromagnetic case) the system flows to strong coupling regime. Extracted from Ref. [6].

For simplicity, the scale at which the perturbation theory breaks down is obtained for the antiferromagnetic model with $J_\pm = J_z = J$ through integration of the resulting differential equation Eq. (3.41) from an initial cut-off D and coupling J through the new cut-off $\tilde{D}$ and renormalized coupling $\tilde{J}$, this leads to [8]:

$$De^{-1/2J\rho_0} = \tilde{D}e^{-1/2\tilde{J}\rho_0} \sim k_B T_K, \tag{3.44}$$

where $T_K \sim e^{-1/2\tilde{J}\rho_0}$ is defined as the *Kondo temperature* and characterizes the trajectories resulting from the scaling process. In other words, systems with different parameters D, J that lie in the same trajectory are equivalent and have the same low energy behavior, which is determined by T_K. In this sense, T_K acts as a scale invariant of the theory and all the thermodynamics quantities depend only on the single energy scale T_K [8] (provided we are in the limit of validity of the scaling theory, which is the weak coupling where $\rho_0 J \ll 1$).

We see that for the ferromagnetic case a complete solution of the problem through scaling is provided since scaling can be conducted down to $\tilde{D} \to 0$. In this case, $\tilde{J} \to 0$ and the system has an uncoupled spin. Hence, the impurity spin becomes asymptotically free giving a Curie law contribution to the impurity susceptibility [8].

For the antiferromagnetic model, the reduction of the band width is only possible

until $\tilde{D} \sim k_B T_K$ beyond which perturbation theory breaks down.

A complete solution for this problem requires a non-perturbative approach capable of describing the thermodynamic properties of the impurity system in the strong coupling regime. This will be the topic we treat in the following.

3.4 The numerical renormalization group method (NRG) and the pseudogap impurity problem

3.4.1 Introductory remarks

An important advance in solving the Kondo problem was achieved in 1975 by K. G. Wilson [36], who developed a nonperturbative approach, called Numerical Renormalization Group (NRG) method, which managed to describe the low temperature behavior of the thermodynamic properties of the Kondo model. Initially, Wilson applied the method to calculate the zero temperature limit of the susceptibility and specific heat of the Kondo Hamiltonian [8, 36]. Later on, the method was extended to the Anderson model [10, 55]. In these works the authors give a clear and profound exposition of the method and apply it to determine the low temperature behavior of both the symmetric ($\epsilon_d = -U/2$) [10] and asymmetric ($\epsilon_d \neq -U/2$) [55] Anderson model.

Before presenting the NRG method, we first bring to light the special aspect about studying the Kondo effect in graphene. Even though the results presented in the above works contain some of the key ideas for the development of theoretical physics in the last century, they are not straightforwardly applicable to graphene. But why this is so? A most careful reader probably knows the answer: graphene's linear density of states that vanishes at the Dirac point.

So far all the results we have been discussing concern an impurity immersed in a nonmagnetic metal, whose density of states is a constant. These results are universal, that is, they are independent of the details of the microscopic models studied and the system specific features are encoded in T_K. The low energy band structure gives graphene a special status in the Kondo story, it belongs to the so-called pseudogap Kondo systems.

This kind of problem was first addressed in the early 90's by Withoff and Fradkin [37], whose theoretical approach considered a density of states which vanishes at the Fermi level

($\epsilon_F = 0$) and follos a power-law of the form [38]:

$$\rho(\epsilon) = \begin{cases} \rho_0|\epsilon|^r, & \text{for } |\epsilon| \leq D \\ 0, & \text{otherwise}\,. \end{cases} \tag{3.45}$$

where D is the band's half-width. Based on perturbative methods such as the poor man's scaling for the spin 1/2 Kondo model, the authors found important features of systems with power-law density of states such as the existence of a critical value for the coupling constant J_c under which no screening takes place. This is very different from the usual Kondo effect where the local moment is always screened. This result was supported by a large-N (N meaning the impurity's degeneracy) expansion to the Coqblin-Schrieffer model[6] that produced similar results to those derived for the Kondo model [37]. The study addressed a restricted range of r values, namely, $0 \leq r < 1/2$. Subsequent works [65, 66] expanded the validity of the results to all positive r.

Poor man's scaling was also used to analyse the Anderson model in the context of pseudogap systems [67]. Again it is found that in a finite region of the parameter space the impurity remains unscreened down to $T \to 0$. This behavior is associated with the occurrence of a quantum phase transition. It was identified that the size of the parameter space region of this "unscreened impurity" regime grows with r [67].

The quantum critical behavior of pseudogap systems and the important role played by particle-hole symmetry is fully explored in Ref. [38]. Under particle-hole symmetry, for instance, the critical coupling J_c is shown to be infinite for values of $r > 1/2$ [38, 68], meaning that the impurity spin is never screened in this cases. Such behavior is not seen in the asymmetric case where J_c remains finite for $r > 1/2$ [38, 68].

As in the regular Kondo problem a thorough study of a magnetic impurity in a pseudogap system requires the use of the NRG method. For that purpose Wilson's ideas were generalized to treat impurity models with an energy dependent hybridization function [38].

Our work does not contain a further development of the NRG method. However, we apply the method in a new context, namely, disordered pseudogap systems (results are presented in the next chapter).

We now turn to a brief discussion of the schematics of the NRG applied to the Anderson Hamiltonian already adapted for the pseudogap problem [38] and discuss some

[6] A description of this model is found in [8].

main results obtained from it for the pseudogap and usual impurity problems. The literature contains very nice and detailed accounts on the NRG method for both, the metallic [10, 36, 55] and pseudogap [9, 38] problems.

3.4.2 Schematics of the method

First it should be stated that the NRG is applied to systems which involve a quantum mechanical impurity with a small number of degrees of freedom coupled to a band of non-interacting electrons (extension to the bosonic system is also possible [9]). For models where the band electrons show correlations, the problem should be first mapped onto non-interacting impurity models through the dynamical mean field theory (DMFT) and then NRG is applied [9].

We now summarize the description of the NRG method for a pseudogap system for the Anderson Hamiltonian found in [38].

3.4.2.1 Structure of the Hamiltonian

The method addresses the Anderson Hamiltonian Eq. (3.1). Assuming, for simplicity, spatially isotropy one writes $\epsilon_{\mathbf{k}} \equiv \epsilon_{|\mathbf{k}|}$ and $\gamma_{\mathbf{k}} \equiv \gamma(\epsilon_{|\mathbf{k}|})$ which means that the impurity interacts only with s-wave states centered on the impurity site. This simplification allows to express the Anderson Hamiltonian in a one dimensional energy representation[7] [38].

$$\begin{aligned} H_{\text{state}} &= \sum_{\sigma} \epsilon_d \, n_{d\sigma} + U n_{d\uparrow} n_{d\downarrow} \\ H_{\text{band}} &= \int_{-D-\mu}^{D-\mu} d\omega \; \omega \; c^{\dagger}_{\omega\sigma} c_{\omega\sigma} \\ H_{\text{hop}} &= \int_{-D-\mu}^{D-\mu} d\omega \sqrt{\Gamma(\omega)/\pi} \left(c^{\dagger}_{d\sigma} c_{\omega\sigma} + \text{H.c.} \right) \; , \end{aligned} \tag{3.46}$$

where $H_A = H_{\text{state}} + H_{\text{band}} + H_{\text{hop}}$. It is assumed that the s-wave energies are contained in the interval $-D \leq \epsilon_{\mathbf{k}} \leq D$, and we introduce for convenience the variable $\omega \equiv \epsilon_{|\mathbf{k}|} - \mu$ to account the effect of a finite chemical potential μ. The operator $c^{\dagger}_{\omega\sigma}$ creates an electron in a s-wave state with energy ω and is supposed to be normalized as $\{c^{\dagger}_{\omega\sigma}, c_{\omega'\sigma'}\} = \delta(\omega - \omega')\delta_{\sigma\sigma'}$. The quantity $\Gamma(\omega) = \pi\rho(\omega)|\gamma(\omega)|^2$ is the hybridization function which we encountered earlier in the context of the mean field solution of the Anderson model.

The appearance of the hybridization function on the hopping Hamiltonian means that

[7] A detailed account on this procedure can be found in Ref. [10].

the interaction of the impurity with the band is mediated only by this quantity. In other words, the functional dependence of the density of states and the hopping integrals with energy as separated quantities are unimportant[8] as long as their combination gives the same hybridization function. Hence, different expressions of the Anderson Hamiltonian are allowed [9]. We keep Eq. (3.46) because it is suitable for the pseudogap problem. As in Ref. [38], we consider a power-law hybridization function

$$\Gamma(\omega) = \begin{cases} \Gamma_0|\omega|^r & \text{for } -D-\mu \leq \omega \leq D-\mu \\ 0 & \text{otherwise}\,. \end{cases} \tag{3.47}$$

where Γ_0 is a reference value [38]. In the next chapter we will analyse results obtained for a similar structure for the case of graphene.

In the subsequent derivations we use a dimensionless energy $\epsilon = \omega/D$ and chemical potential $\mu' = \mu/D$ following the treatment of Ref. [38].

3.4.2.2 Logarithmic discretization

Poor man's scaling shows how different band energy intervals contributes to the logarithmic divergences encountered in the resistivity obtained from the analysis of the Anderson Hamiltonian [8, 36, 63]. A suitable treatment of the band electron was proposed by Wilson, who put forth a logarithmic discretization of the ϵ space whose domain is spanned by a set of intervals controlled by a discretization parameter $\Lambda\,(>1)$ [10, 36] shown in Fig. 19a. This process guarantees that energy values close to the Fermi level, which determine the low temperature physics of the system, are well sampled [10] (see Fig. 19b).

The procedure consists in dividing the band into two sets of logarithmic bins, one for positive values $\epsilon^+_{m+1} < \epsilon \leq \epsilon^+_m$, where [38]

$$\epsilon^+_0 = 1-\mu', \quad \epsilon^+_m = (1-\mu')\Lambda^{1-z-m}, \quad m>0, \tag{3.48}$$

and another for negative energies $\epsilon^-_m \leq \epsilon < \epsilon^-_{m+1}$, where [38]

$$\epsilon^-_0 = -(1+\mu'), \quad \epsilon^-_m = -(1+\mu')\Lambda^{1-z-m}, \quad m>0. \tag{3.49}$$

The discretization parameter usually takes values $\Lambda \sim 2-3$. Originally Wilson used $\Lambda = 2.5$, $\mu' = 0$ and $z = 1$ [10, 36]. Introduction of the parameter $z \neq 1$ was

[8] The only exception to this is on the calculation of the host thermodynamic properties without the magnetic impurity, in which the precise form of the density of states should be considered [38].

proposed as a useful tool to approach the "exact" results of the continuum limit $\Lambda \to 1$ for thermodynamic [69] and dynamical [70] quantities, and also allows the use of larger Λ (for instance, $\Lambda = 9$ is used in Ref. [38]). This is accomplished by averaging the physical quantities over different z values for a fixed Λ. For more details on the use of this technique see Refs. [9, 69, 70, 71].

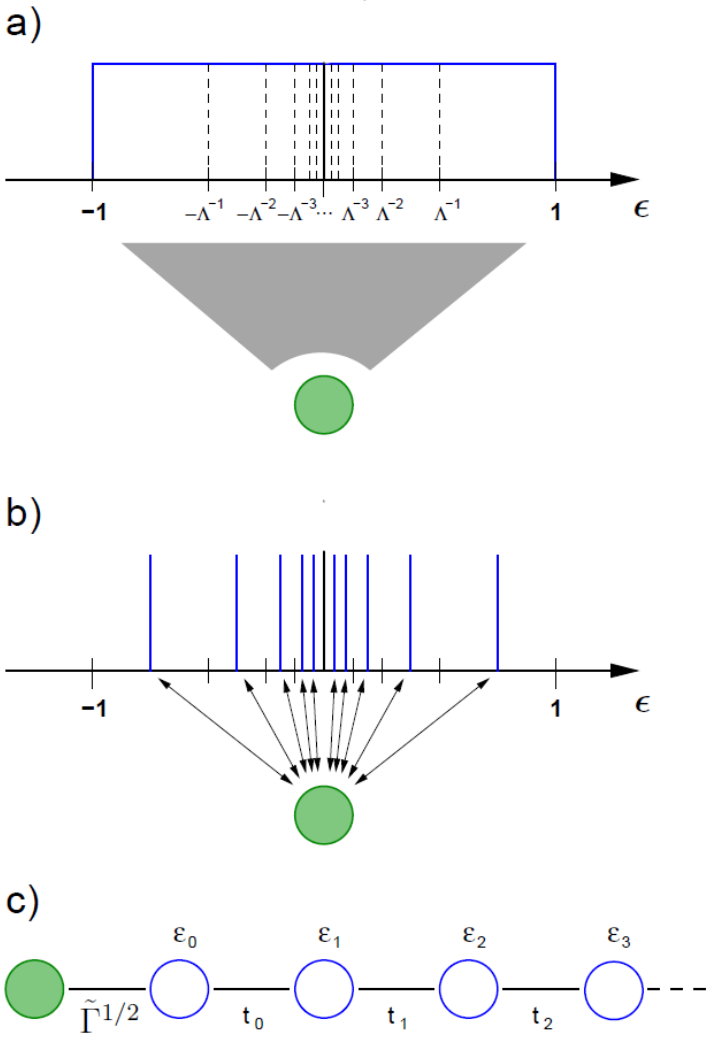

Figure 19: a) Logarithimic discretization of the conduction electron band. b) The continuum of states within each bin is substituted by a single value after discarding of the $q \neq 0$ modes. c) Semi-infinite chain form of the system. The first site (green circle) denotes the impurity which couples to the first conduction site through $\tilde{\Gamma}^{1/2}$. Each site is incorporated in one iterative step and couples to the last site of the smaller chain through the hoppings t_i, $i = 0, 1, \ldots$. Extracted from Ref. [9].

Within each positive (negative) nth interval is introduced a set of orthonormal functions $\psi_{an}^{(q)}(\epsilon)$ ($\psi_{bn}^{(q)}(\epsilon)$) and a set of destruction operators $a_{n\sigma}^{(q)}$ ($b_{n\sigma}^{(q)}$), where $q = 0, \pm 1, \pm 2, \ldots$. Outside the bins the functions are null. In this basis, the conduction band operators read

[38]:

$$c_{\epsilon\sigma} = \sum_{n=0}^{\infty} \sum_{q=-\infty}^{\infty} \left[\psi_{an}^{(q)}(\epsilon) a_{n\sigma}^{(q)} + \psi_{bn}^{(q)}(\epsilon) b_{n\sigma}^{(q)} \right]. \tag{3.50}$$

Originally, Wilson adopted the set of functions [9, 10]:

$$\psi_{an}^{(q)}(\epsilon) = \frac{1}{\sqrt{d_n}} e^{i\omega_n q \epsilon} \quad \text{and} \quad \frac{1}{\sqrt{d_n}} \psi_{bn}^{(q)}(\epsilon) = e^{-i\omega_n q \epsilon}, \tag{3.51}$$

with $\omega_n \propto 1/d_n$, d_n being the width of the n-th logarithmic bin. For a metallic system the hybridization function $\Gamma(\epsilon)$ is a constant. In this case, it is easy to see that due to the orthogonality of the ψ's, substitution of Eqs. (3.50) and (3.51) into the hopping Hamiltonian Eq. (3.46) filters only the $q = 0$ mode from the expansion Eq. (3.50).

A crucial piece in Wilson's reasoning for mapping the original problem into a semi-infinite chain form is to make the impurity couple only to the $q = 0$ mode of the conduction band states of every energy bin. For pseudogap systems it is also possible to proceed in the same way, but it requires the introduction of a weighting function. By defining the zero-mode functions in each bin as [38]:

$$\psi_{an}^{(0)}(\epsilon) = \begin{cases} \mathcal{W}(\epsilon)/F_{an}, & \text{for } \epsilon_{n+1}^{+} < \epsilon \leq \epsilon_n^{+} \\ 0, & \text{otherwise}\,; \end{cases} \tag{3.52}$$

$$\psi_{bn}^{(0)}(\epsilon) = \begin{cases} \mathcal{W}(\epsilon)/F_{bn}, & \text{for } \epsilon_n^{-} \leq \epsilon < \epsilon_{n+1}^{-} \\ 0, & \text{otherwise}\,, \end{cases} \tag{3.53}$$

and upon the definition of the weighting function $\mathcal{W}(\epsilon)$ as [38]:

$$\mathcal{W}(\epsilon) = \left[\Gamma(\epsilon D)/\Gamma_0 \right]^{1/2}, \tag{3.54}$$

(with $\Gamma(\epsilon)$ and Γ_0 defined in Eq. (3.47)) the zero mode wavefunctions $\psi_{an}^{(0)}(\epsilon)$ and $\psi_{bn}^{(0)}(\epsilon)$ possess the same energy dependence as the hybridization function in the Hamiltonian H_{hop} in Eq. (3.46). The orthonormality condition on the ψ functions implies [38]

$$F_{an}^2 = \int_{\epsilon_{n+1}^{+}}^{\epsilon_n^{+}} d\epsilon\, \mathcal{W}^2(\epsilon), \quad F_{bn}^2 = \int_{\epsilon_n^{-}}^{\epsilon_{n+1}^{-}} d\epsilon\, \mathcal{W}^2(\epsilon). \tag{3.55}$$

Due to the construction above, orthogonality guarantees that only the zero mode functions in the expansion Eq. (3.50) are retained[9] when this is inserted into H_{hop} in Eq.

[9] An alternative route to filter the zero-mode wavefunctions is proposed by Bulla and collaborators, arriving at the same physics [9].

(3.46). This process leads to the hopping Hamiltonian [38]:

$$H_{\rm hop} = \sqrt{\Gamma_0 D/\pi}\left[c^{\dagger}_{d\sigma}\sum_{n=0}^{\infty}\left(F_{an}a^{(0)}_{n\sigma} + F_{bn}b^{(0)}_{n\sigma}\right) + H.c.\right]. \tag{3.56}$$

In terms of the expansion Eq. (3.50), the conduction band Hamiltonian is written as [38]:

$$H_{band} = D\sum_{n,\sigma,q,q'}\int_{-(1+\mu')}^{1-\mu'} d\epsilon\,\epsilon\left[\psi^{(q)*}_{an}(\epsilon)\psi^{(q')}_{an}(\epsilon)a^{(q)\dagger}_{n\sigma}a^{(q')}_{n\sigma} + \psi^{(q)*}_{bn}(\epsilon)\psi^{(q')}_{bn}(\epsilon)b^{(q)\dagger}_{n\sigma}b^{(q')}_{n\sigma}\right]. \tag{3.57}$$

Until now the results presented are exact. From Eq. (3.57) we see that the higher q modes only couple to the impurity indirectly via the non-diagonal terms of Eq. (3.57) which involve the $q = 0$ mode. For a flat band, Wilson showed that the coupling between the modes $q \neq q'$ vanishes as the continuum limit $\Lambda \to 1$ is approached [9, 36] and made the approximation[10] of discarding those terms for $\Lambda > 1$. For pseudogap systems, one can show that the coefficients of the $q \neq q'$ terms of H_{band} in Eq. (3.57) are proportional to $1 - \Lambda^{-1}$ [9], also vanishing as $\Lambda \to 1$. Hence, the same reasoning applied by Wilson is employed. With this approximation, the $q \neq 0$ modes decouple from the impurity and contribute to the kinetic energy in Eq. (3.57) a constant term which is dropped [38]. This role process corresponds to substituting the continuum of energies within each bin by a single value as shown in Fig. 19b [9]. The resulting Hamiltonian is [38]:

$$H_{band} \cong D\sum_{n=0}^{\infty}\left(\epsilon_{an}a^{(0)\dagger}_{n\sigma}a^{(0)}_{n\sigma} + \epsilon_{bn}b^{(0)\dagger}_{n\sigma}b^{(0)}_{n\sigma}\right), \tag{3.58}$$

where the energies ϵ_{an} and ϵ_{bn} are given by [38]:

$$\epsilon_{an} = F^{-2}_{an}\int_{\epsilon^{+}_{n+1}}^{\epsilon^{+}_{n}} d\epsilon\,\epsilon\,\mathcal{W}^2(\epsilon),\ \ \epsilon_{bn} = F^{-2}_{bn}\int_{\epsilon^{-}_{n}}^{\epsilon^{-}_{n+1}} d\epsilon\,\epsilon\,\mathcal{W}^2(\epsilon). \tag{3.59}$$

3.4.2.3 Mapping on a semi-infinite chain

The logarithmic discretization leads to the hopping and band contributions of the Anderson Hamiltonian given by Eqs. (3.56) and (3.58), respectively. The following step of the method is to transform the resulting Anderson model into a semi-infinite chain

[10] An estimate of this "discretization" error is given in Sec. V of [38].

Hamiltonian. This is achieved in two stages. First, by defining the operator [38]

$$f_{0\sigma} = F^{-1} \sum_{n=0}^{\infty} \left[F_{an} a_{n\sigma}^{(0)} + F_{bn}^{(0)} b_{n\sigma}^{(0)} \right], \tag{3.60}$$

where the normalization factor F reads [38]:

$$F^2 = \int_{-(1+\mu')}^{1-\mu'} d\epsilon \, \mathcal{W}^2(\epsilon). \tag{3.61}$$

After the transformation, the hopping Hamiltonian Eq. (3.56) reads [38]:

$$H_{hop} = \sqrt{\Gamma_0 D/\pi} F \sum_{\sigma} \left(f_{0\sigma}^{\dagger} c_{d\sigma} + H.c \right). \tag{3.62}$$

Now, a new basis of operators $\{f_{n\sigma}\}$ orthogonal to $f_{0\sigma}$ should be constructed using the original operators $\left\{ a_{n\sigma}^{(0)}, b_{n\sigma}^{(0)} \right\}$. There are many ways of constructing such a basis, but each one would transform the band Hamiltonian Eq. (3.58) into a non-diagonal form. The most convenient choice is the basis where the new operators are only coupled to their nearest neighbors [38]:

$$H_{band} = D \sum_{n=0,\sigma}^{\infty} \left[\epsilon_n f_{n\sigma}^{\dagger} f_{n\sigma} + \tau_n \left(f_{n\sigma}^{\dagger} f_{n-1\sigma} + H.c \right) \right], \tag{3.63}$$

where in Eq. (3.63) the energies and hoppings are given by the recursive relations [38]:

$$\epsilon_n = \langle f_{n\sigma} | H_{band}/D | f_{n\sigma} \rangle, \tag{3.64}$$

$$\tau_{n+1} | f_{n+1,\sigma} \rangle = \left(H_{band}/D - \epsilon_n \right) | f_{n\sigma} \rangle - \tau_n | f_{n-1,\sigma} \rangle, \tag{3.65}$$

$$\langle f_{n+1\sigma} | f_{n+1\sigma} \rangle = 1, \tag{3.66}$$

$$| f_{n\sigma} \rangle = f_{n\sigma}^{\dagger} | \text{vacuum} \rangle. \tag{3.67}$$

$|\text{vacuum}\rangle$ is the system vacuum.

The operators $f_{n\sigma}$ are expressed in terms of the $\left\{ a_{n\sigma}^{(0)}, b_{n\sigma}^{(0)} \right\}$ basis as [38]:

$$f_{n\sigma} \equiv \sum_{n=0}^{\infty} \left(u_{nm} a_{m\sigma}^{(0)} + v_{nm} b_{m\sigma}^{(0)} \right), \tag{3.68}$$

with $u_{0m} = F_{am}/F$ and $v_{0m} = F_{bm}/F$. The remaining u_{nm} and v_{nm} being determined by the recursion equations Eqs. (3.64)-(3.67).

One can interpret the sites of the obtained semi-infinite chain as follows: the first site of the chain is the impurity and the others are conduction electron sites which are aggregated to the chain at each iterative step as shown in Fig. 19c. The physical meaning attributed to the conduction band sites by Wilson is that [36]: the first site of the conduction electron chain corresponds to the shell with maximum of its wavefunction close to the impurity. This shell couples to a shell further away from the impurity and so on (see Fig.20).

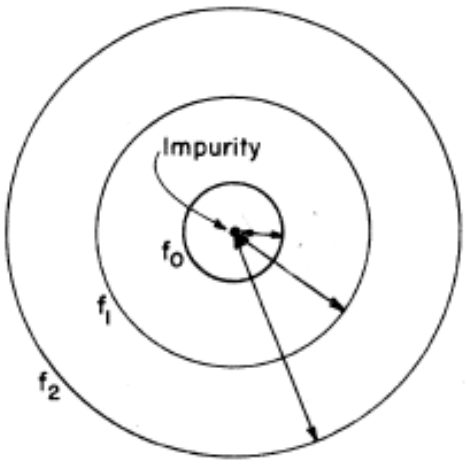

Figure 20: Schematic representation of the wavefunctions represented by the $f_{n\sigma}$ electron states. As n increases the states become more spread about the impurity position. Extracted from Ref. [10]

3.4.2.4 Iterative Diagonalization

A natural question to ask is why perform all this work and by the end be stuck to a Hamiltonian which still has infinite degrees of freedom? The first part of the answer relies on the fact that the semi-infinite chain impurity Hamiltonian is solved conveniently by iterative diagonalization, that is, a new conduction electron site is added to the chain at each iteration step and the enlarged Hamiltonian is diagonalized. The second point is that the hopping coefficients τ_n typically decrease as $\Lambda^{-n/2}$ for large n and ε_n drops off at least that fast [38][11].

The concept of the renormalization group enters in the context through this energy dependence of the τ_n: the introduction of a new site to the chain reduces the relevant

[11] Analytical expressions for these hoppings were derived for metallic and pseudogap cases in [36] and [72], respectively.

energy scale by $\Lambda^{1/2}$. Because the τ_n falls off exponentially, only states of the shorter chain within a comparatively reduced window are relevant for the interaction with the new site. This picture allows the truncation of the energy spectrum obtained at each step of the iterative process and the construction of the extended Hamiltonian from this truncated basis. We develop these ideas in the following.

The infinite chain Hamiltonian may be written as the limit of a sequence of Hamiltonians [38]:

$$H = \lim_{N\to\infty} \alpha D \Lambda^{-N/2} H_N, \tag{3.69}$$

where

$$\alpha = \frac{1}{2}\left(1+\Lambda^{-1}\right)\Lambda^{3/2-z} \tag{3.70}$$

is a conventional factor that approaches unity as $\Lambda \to 1$ [38].

The Hamiltonian H_N, defined for $N > 0$, denotes a $(N+2)$-site[12] chain Hamiltonian constructed from the sum of the discretized band Eq. (3.63) (restricting the sum to the maximum value $n = N$), the hopping term Eq. (3.62) and the impurity contribution H_{state} from Eq. (3.46). Hamiltonian H_{N-1} and H_N, resulting after the incorporation of a new site to H_{N-1}, are related by a recursion relation [38]:

$$H_N = \Lambda^{1/2} H_{N-1} + e_N f^\dagger_{N\sigma} f_{N\sigma} + t_N \left(f^\dagger_{N\sigma} f_{N-1,\sigma} + H.c. \right) - E_{G,N}, \tag{3.71}$$

where e_n and t_n are on-site and hopping energies [38]

$$e_n = \alpha^{-1}\Lambda^{n/2}\epsilon_n \quad \text{and} \quad t_n = \alpha^{-1}\Lambda^{n/2}\tau_n \tag{3.72}$$

scaled in such a way as to cancel the $\Lambda^{-n/2}$ decay of the original parameters (ε_n and τ_n) as n gets large.

Subtraction of the ground state $E_{G,N}$ assures that the ground state energy of H_N is set to zero in each step.

The starting point of the sequence Eq. (3.69) is given by the atomic limit of the impurity problem H_0 [38]:

$$H_0 = e_0 \sum_\sigma f^\dagger_{0\sigma} f_{0\sigma} + \tilde{\epsilon_d} n_d + \tilde{U} n_{d\uparrow} n_{d\downarrow} + \tilde{\Gamma}^{1/2} \sum_\sigma \left(f^\dagger_{0\sigma} c_{d\sigma} + H.c. \right) - E_{G,0} \tag{3.73}$$

with scaled parameters [38]:

$$\tilde{\epsilon_d} = \frac{\epsilon_d}{\alpha D}, \quad \tilde{U} = \frac{U}{\alpha D}, \quad \tilde{\Gamma} = \frac{F^2 \Gamma_0}{\pi \alpha^2 D}. \tag{3.74}$$

[12] $N+1$ conduction electrons sites plus the impurity one.

The character of the renormalization group shows up more clearly if we interpret the Hamiltonian H_N in Eq. (3.71) as a result of a renormalization group (RG) transformation R over H_{N-1} [9]:

$$H_N = R\left(H_{N-1}\right). \tag{3.75}$$

However this is not an usual RG transformation where one goes from an Hamiltonian $H(\mathbf{K})$ dependent on the set of parameters $\mathbf{K}$ to a transformed Hamiltonian $H(\mathbf{K}')$ with a new set of parameters $\mathbf{K}'$. This kind of representation is hardly obtained for the H_N resulting from NRG iterative process [9]. In this case, H_N and the RG flow are characterized directly by the many-particle energies $E_N(r)$ which obey the characteristic equation [9]

$$H_N|r\rangle_N = E_N(r)|r\rangle_N,\ r = 1, 2, ..., N_s, \tag{3.76}$$

with N_s the dimension of H_N.

Hence, once the Hamiltonian H_N has been diagonalized, its eigenstates in connection with a basis for the new site are used to construct one basis for H_{N+1} using Eq. (3.71) (for details of this process see Refs. [9] and [10]). The H_{N+1} obtained is diagonalized and its "eigenbasis" will be used for the construction of a basis for H_{N+2}.

As one can see from Eq. (3.71), before each step the Hamiltonian whose spectrum was already calculated H_{N-1} is rescaled by the factor $\Lambda^{1/2}$ in order to always keep the smallest energy scale in the spectrum of order unity [38].

A drawback of the method is that the Hilbert space increases exponentially ($\sim 2^{2(N+2)}$) when new sites are aggregated to the chain, transforming the diagonalization of such large-sized matrices numerically prohibitive. This problem is circumvented by setting a truncation scheme which only keeps the lowest M energy states of the spectrum of H_N[13].

Wilson justified this procedure arguing that for calculating low temperature properties of a system the low-lying energy states are the most relevant [10, 36]. In this way, an important observation is that neglecting the high-energy spectrum does not spoil the low-energy one in subsequent iterations [9]. Also, as the addition of a new site can be viewed as a perturbation of relative strength $\Lambda^{-1/2}$, high-energy states become less and less important as the number of sites increases. Of course on approaching the continuum limit $\Lambda \to 1$, an increasing number of states should be retained to ascertain liable results.

It should be noticed that the outputs of the method are obtained from a compromise between two conflicting goals: first, one wishes accurate results which implies the choice

[13] Alternatively one may keep the states within a range of energy E_c of the ground state energy [38].

of a "small" Λ (close to unity) to minimize *discretization error* and making M large to reduce *truncation error*, both requiring extensive computational demand; Second, a shorter computational time, implying to larger Λ and smaller M [38].

The procedure in going from step N to $N+1$ is summarized in Fig. 21. In a) is the truncated spectrum of H_N with its ground state set to zero. b) shows the same spectrum scaled by the factor $\Lambda^{1/2}$. The spectrum after the new site is added is shown in c) and d) presents what it looks like after truncation and setting the ground state energy to zero.

This closes our discussion on the basic scheme of the NRG method. In the next topic we approach on the interpretation of the NRG outputs.

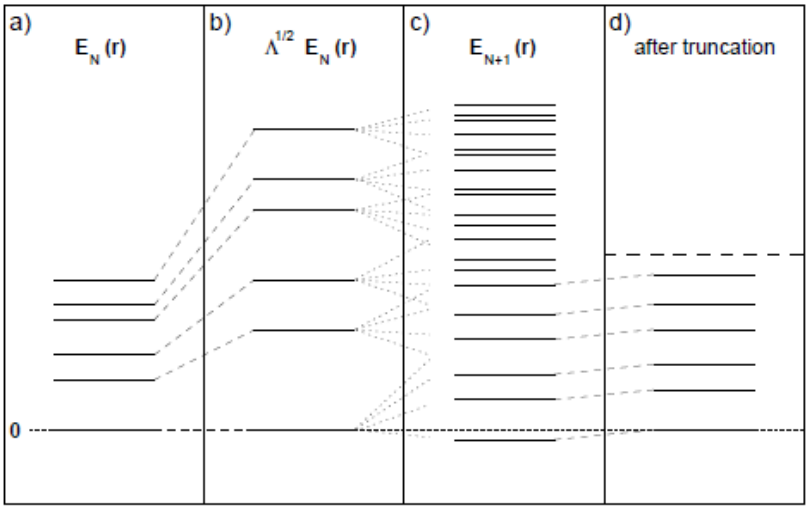

Figure 21: Illustration of how one passes from H_N to H_{N+1} in the NRG. a) Lowest energy levels of the chain Hamiltonian H_N. Note that the ground state is set to zero. b) Scaling of the states in a) by the factor $\Lambda^{1/2}$. c) Low-energy states of H_{N+1}. d) Spectrum of H_{N+1} after truncation and setting the ground state energy to zero. Extracted from Ref. [9].

3.4.3 Overview on the physics of fixed points

An example of the eigenvalues flow calculated through the iterative procedure by Krishna-Murthy et al [10] is shown in Fig. 22, for the symmetric Anderson model with a flat band. The plot is clearly characterized by three regions, separated by crossover regimes, where the solutions remain almost invariant as N changes. In this case the eigensolutions approach a so-called *fixed point* of the system.

A fixed point H^* of the transformation R^2 is defined by the condition[14] $R^2(H^*) = H^*$.

[14]The transformation R itself does not have fixed points because the spectra due to a chain with

The fixed points are numerically characterized by the condition that H_N and H_{N+2} have the same low-energy spectra and that matrix elements of any significant operator O obtained by the low-lying eigenstates of H_N coincide with the elements calculated using the low-lying eigenstates of H_{N+2} [10, 36].

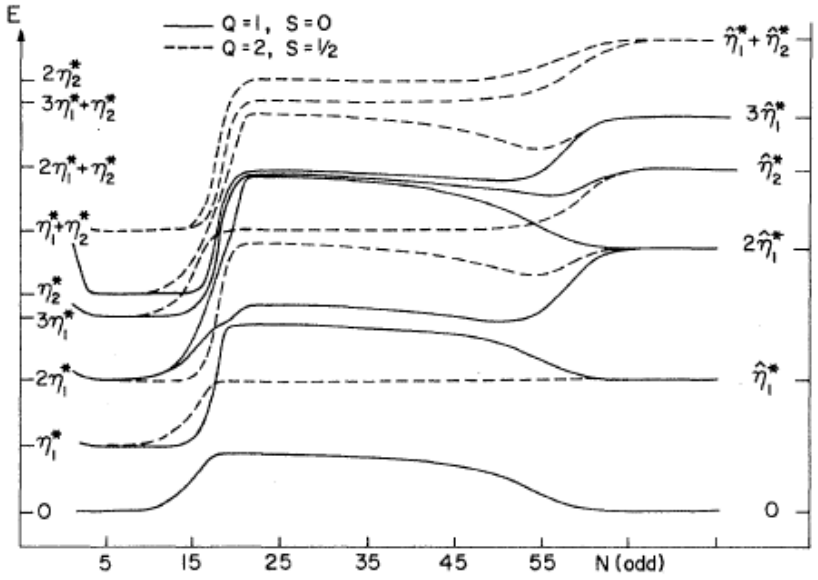

Figure 22: Eigenvalues flow for the lowest energy states of the symmetric Anderson model with a flat band from Ref. [10]. The vertical axis correspond the fixed point eigenstates shown in Fig. 23. Q and S are "good" quantum numbers that allows optimization in the diagonalization process (see Ref. [10] for further discussion). Extracted from Ref. [10].

By setting the parameters of the Anderson model $\tilde{\epsilon_d}$, $\tilde{U}$, $\tilde{\Gamma}$ in Eq. (3.74) either to zero or to infinity one obtains the weak- and strong-coupling fixed points of the model. These particular fixed points are very important in the analysis and understanding of the NRG results for two main reasons: i) They can be represented by a sum of effective single particle Hamiltonians due to the impurity and to the conduction band, whose contribution writes [38]:

$$H_N^{(L)} = \sum_{n=L}^{N} \Lambda^{(N-n)/2} \left[e_n f_{n\sigma}^\dagger f_{n\sigma} + t_n \left(f_{n\sigma}^\dagger f_{n-1\sigma} + H.c. \right) \right], \tag{3.77}$$

where L determines the innermost shell f_L onto which conduction electrons can hop, which implies $t_L = 0$;

ii) The spectrum flow and thermodynamic properties of the semi-infinite chain Hamiltonian in the intermediate coupling regime (general values of $\tilde{\epsilon_d}$, $\tilde{U}$, $\tilde{\Gamma}$) are, in almost all

even and odd number of sites do not coincide. A good example is given in [38] which cites particle-hole symmetry as responsible for the existence of a zero eigenvalue in a chain with odd sites that does not exist for the even situation.

situations, well described in terms of the results of the weak- and strong-coupling fixed points[15].

The realization that the physics of the weak and strong-coupling fixed points could be extracted from the understanding of the structure of the conduction band Hamiltonian is one of the many clever insights in Wilson's approach: because $H_N^{(L)}$ has a quadratic form, the Hamiltonian Eq. (3.77) can be diagonalized exactly. Since Eq. (3.77) satisfies the recursive relation Eq. (3.71), fixed point condition is attained through numerical diagonalization of Eq. (3.77) and observation that for large N the eigenvalues approach a limiting set[16] invariant with N.

Figure 23 shows the lowest order eigenvalues for the weak- and strong-coupling fixed points of the symmetric Anderson model obtained by Krishna-Murthy et al in Ref. [10] for a flat band ($r = 0$). The fixed point Hamiltonians H_{FO}, H_{LM} and H_{SC} denote the free orbital (also named free impurity [38]), local moment and strong coupling fixed points, respectively [10].

Charge Q	Spin S	Index r	Energy in $H^*_{\rm FO}$	$H^*_{\rm LM}$	$\hat{H}^*_{\rm SC}$
1	0	1	0	η_1^*	0
		2	η_1^*	$3\eta_1^*$	$\hat{\eta}_1^*$
		3	$2\eta_1^*$	η_2^*	$2\hat{\eta}_1^*$
		4	$2\eta_1^*$	$2\eta_1^* + \eta_2^*$	$2\hat{\eta}_1^*$
		5	$3\eta_1^*$	$2\eta_1^* + \eta_2^*$	$3\hat{\eta}_1^*$
		6	η_2^*	$2\eta_1^* + \eta_2^*$	$\hat{\eta}_2^*$
2	$\frac{1}{2}$	1	η_1^*	$2\eta_1^*$	$\hat{\eta}_1^*$
		2	$2\eta_1^*$	$\eta_1^* + \eta_2^*$	$2\hat{\eta}_1^*$
		3	$3\eta_1^*$	$\eta_1^* + \eta_2^*$	$3\hat{\eta}_1^*$
		4	η_2^*	$3\eta_1^* + \eta_2^*$	$\hat{\eta}_2^*$
		5	$\eta_1^* + \eta_2^*$	$3\eta_1^* + \eta_2^*$	$\hat{\eta}_1^* + \hat{\eta}_2^*$
		6	$\eta_1^* + \eta_2^*$	$2\eta_2^*$	$\hat{\eta}_1^* + \hat{\eta}_2^*$

Figure 23: Lowest energy states for the free orbital, local moment, and strong coupling odd-N fixed point Hamiltonians of the symmetric Anderson model with a flat band, $r = 0$. Extracted from Ref. [10].

The Symmetric Anderson model has three fixed points. The free orbital fixed point

[15]This is true for the metallic case. However, for pseudogap systems there are intermediate coupling fixed points that are only accessible by a full implementation of the NRG [38].

[16]Actually there will be two sets of limiting values, for odd and even N.

corresponds to the choice $\tilde{\epsilon_d} = \tilde{U} = \tilde{\Gamma} = 0$ in Eq. (3.73) and is described by the sum of $H_N^{(0)}$ in Eq. (3.77) and a free impurity orbital of zero energy [10, 38, 55]. The Local-moment fixed point corresponds to the configuration $\tilde{\Gamma} = 0$ and $\tilde{U} = -2\tilde{\epsilon_d} = \infty$. The effective Hamiltonian describing this process is again given by the conduction electron term $H_N^{(0)}$, but now the impurity state is restricted to the single occupied configuration [10, 38, 55]. The symmetric[17] strong coupling fixed point occurs when $\tilde{\Gamma} \to \infty$, $\tilde{U}$ and $\tilde{\Gamma}$ remains finite. In this case an infinite gap separates the ground state and excited states, whose energies $\sim \tilde{\Gamma}^{1/2}$ (see Table I in [10]), of the atomic Hamiltonian. In this situation the coupling between the impurity state and the conduction electrons is so strong at the impurity site that hopping of conduction electrons onto or off shell 0 is completely suppressed. As a consequence the f_0 degrees of freedom are "frozen out" [38]. Hence, the conduction-band excitations of this system are described by $H_N^{(1)}$ in Eq. (3.77).

We now have the tools to understand the eigenvalue flow diagram of Fig. 22. The data was obtained from NRG calculations by setting $U/D = 10^{-3}$, $U/\pi\Gamma = 12.66$ and $\epsilon_d = -U/2$ [10]. Comparing the eigenvalues in Fig. 23 and the energy values in the vertical axis of Fig. 22 we recognize that the system starts in the free orbital regime ($5 < N < 15$) and, as the system evolves, it enters the local moment regime ($15 < N < 55$) and ends at the strong coupling phase ($61 < N$).

Understanding the energy flow such as the one in Fig. 22 is very helpful for the interpretation of the behavior of the thermodynamics quantities calculated through the NRG, since they resemble the same features as the energy flow. This is illustrated in Fig. 24 where the numerical results for the impurity susceptibility corresponding to the flux in Fig. 22 are given by the curve denoted by A.

This picture suggests that the iterative process sets up a temperature scale where higher values of the iterative step N is associated to lower temperatures. With this in mind we immediately identify the pattern of Fig. 22 in curve A of Fig. 24: for high temperatures the system is in the free orbital regime whose susceptibility approaches $k_B T\chi/(g\mu_B)^2 = 1/8$, where g is the gyromagnetic factor and μ_B is the Bohr magneton [10]. As the temperature is decreased, the system crosses over to the local moment phase and the susceptibility is increased to the value $k_B T\chi/(g\mu_B)^2 = 1/4$ characteristic of a free spin-1/2 impurity. A further temperature decrease drives the system to the strong-coupling regime where the local moment is screened, a signature of the Kondo effect, and $k_B T\chi/(g\mu_B)^2$ vanishes.

[17] There still exists an asymmetric strong coupling fixed point for the asymmetric version of the Anderson Hamiltonian [38].

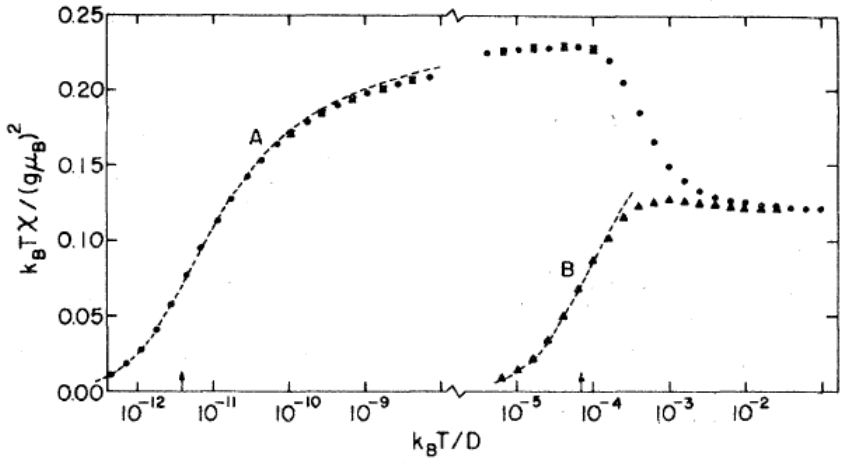

Figure 24: Impurity susceptibility for the metallic symmetric Anderson model calculated in Ref. [10]. We see that the pattern presented in the energy flow in Fig. 22 is reproduced in curve A. Extracted from Ref. [10].

We note that the curve denoted B has a very different behavior, crossing from the free orbital phase straight to the strong coupling one. In this case $U/D = 10^{-3}$ and $\epsilon_d = -U/2$ as in curve A, but the ratio $U/\pi\Gamma = 1.013$. In this case, the increase in the coupling inhibits the existence of a local moment and hence this phase is not present in the susceptibility curve B in Fig 24 (a similar pattern is seen in the energy flow, see Fig. 6 of Ref. [10]).

An important difference between curves "A" and "B" is that, as long as there is no local moment to be screened in "B", the vanishing of the susceptibility in this case is not attributable to the Kondo effect.

This discussion shows that the symmetric Anderson model is very useful for introducing the main ideas in the analysis of the NRG results. However, the susceptibilities calculations that we perform consider the most general situation where $\epsilon_d \neq U/2$, this leads to the asymmetric version of Anderson's model.

The analysis of the NRG results for the asymmetric Anderson model is similar to the symmetric case. However, now the physics is enriched by the appearance of other weak- and strong-coupling fixed points [38, 55]. Besides the free impurity, local-moment and strong-coupling encountered earlier, we also have a valence fluctuation fixed point, which consists in choosing $\tilde{\epsilon_d} = \tilde{\Gamma} = 0$ and $\tilde{U} = \infty$. It is described by the effective Hamiltonian $H_N^{(0)}$ and an impurity part where doubly occupied configurations are ruled out the Hilbert space. Another novelty is the frozen-impurity fixed point which is obtained when $\tilde{\epsilon_d} = \infty$. Under this condition the impurity level is completely depopulated. The

electronic excitations are again represented by $H_N^{(0)}$ in Eq. (3.77). There also exists an asymmetric strong coupling fixed point [38] obtained by adding to the conditions of symmetric strong-coupling the requirement that $e_1 \to \infty$ in Eq. (3.71). In this case the f_1 degree of freedom is also frozen and the effective Hamiltonian describing the system will be given by $H_N^{(2)}$ [38]. In Ref. [38] it is argued that the frozen impurity and asymmetric strong-coupling are physically equivalent. Hence analysis of the Anderson Hamiltonian properties can be focused only on the frozen impurity one.

Another aspect of major importance in the analysis of the NRG results is the discussion of the stability of the fixed points [10, 36, 38, 55]. As we saw from Figs. 22 and 24, as the Hamiltonians H_N were iterated the system passed through the free orbital regime, local-moment and apparently remained still in the strong-coupling phase. The immediate questions that rise are: why the solutions evolve in this way and how can one guarantee that the solutions will not evolve forever?

Suppose that H_N is close to a fixed point solution H^*. It has been shown [10] that the deviation from the fixed point Hamiltonian can be written as a linear combination of operators O_i associated with the active degrees of freedom at the fixed point [38]

$$\delta H_N = H_N - H^* = \sum_i c_i \lambda_i O_i, \tag{3.78}$$

where c_i denotes the coefficients of the expansion and λ_i are the eigenvalues associated to the operators O_i. The eigenvalues λ_i will determine whether the fixed point will be stable or not. The operators O_i may be classified according to the eigenvalues associated to them as: relevant ($\lambda_i > 1$), irrelevant ($\lambda_i < 1$) or marginal ($\lambda_i = 1$)[18]. A fixed point that has relevant perturbations is unstable, this implies that if the solution is close to this fixed point the perturbations will drive the system away from it. If the fixed point has only irrelevant perturbations the opposite occurs and this fixed point is denoted as stable. For the case of marginal perturbation the analysis is not so simple and the system may be stable or unstable[19].

Coming back to our example of Figs. 22 and 24, we see that the flux flow indicates that the free-orbital and local-moment fixed points are unstable and the strong-coupling is stable, consistent with the more detailed analysis presented in Ref. [10].

Marked differences appear in the analysis of the fixed points for pseudogap systems as compared to the metallic case. For instance, the local moment is always stable, ir-

[18] See Ref. [10] for a more complete discussion.
[19] See Ref. [36] for a full account of this problem.

respective of the sign of the Kondo model coupling J, for the pseudogap while for an antiferromagnet coupling the fixed point is always unstable for a flat band [38]. Another significant departure occurs for the symmetric strong-coupling fixed point that is only stable under very restricted conditions (for $r > 1/2$ it is always unstable, for example) for the pseudogap and is always marginally stable for $r = 0$ [38].

The differences presented in the stability of the fixed points for the pseudogap model have profound consequences and put this impurity problem in a distinct universality class than the "conventional" $r = 0$ problem.

Next we address in more detail some manifestations of the distinct character of these systems, in particular, the impurity susceptibilities.

3.4.4 Numerical evaluation of thermodynamic properties. A comparitive analysis between the metallic and pseudogap cases.

Experimentally, the contribution of an impurity to the thermodynamic property $\mathcal{A}$ of a system is given by the comparison of the measured property for the whole system where the impurity is immersed and a reference system without impurity. Based on this, the effect on the quantity $\mathcal{A}$ of adding a single impurity to a host is defined as [38]:

$$\mathcal{A}_{imp} = \langle \mathcal{A} \rangle_{imp} = \langle \mathcal{A} \rangle - \langle \mathcal{A} \rangle_0 = \lim_{N \to \infty} \left[Tr \left(\mathcal{A} e^{-\beta_N H_N} \right) - Tr_0 \left(\mathcal{A} e^{-\beta_N H_N^{(0)}} \right) \right], \qquad (3.79)$$

where $\mathcal{A}$ is an operator which depends on the property of interest, "Tr_0" means a trace over an impurity-free system and the factor β_N is defined as [38]:

$$\beta_N = \alpha D \Lambda^{-N/2} (k_B T)^{-1} = \beta \alpha D \Lambda^{-N/2}. \qquad (3.80)$$

Wilson showed that the error committed in estimating $\mathcal{A}_{imp}$ for a finite N is of order β_N/Λ [10, 36]. Hence, to compute thermodynamic properties for a whole sequence of temperatures T_N, associated with the Hamiltonians H_N, within a certain degree of precision, all one needs is to select an appropriate $\bar{\beta}$ and make $\beta_N = \bar{\beta}$ in Eq. (3.80). A logarithmic temperature scale T_N is obtained from the T's given by Eq. (3.80) for each NRG step. The $\mathcal{A}_{imp}$ calculated from Eq. (3.79), for a given N, is associated with the temperature T_N. Naively one can be tempted to take $\bar{\beta}$ vanishingly small aiming at high precision estimates. However, another factor "forbids" this choice: the truncation scheme on the energy spectra of H_N (which throws out the high energy states). To minimize the contribution of missing states to $\mathcal{A}_{imp}$, one should make $\bar{\beta} E_c$ as large as possible, where

E_c is the maximum energy kept with respect to the ground state. In practice, $\bar{\beta}$ used for the NRG simulations takes a value slightly smaller than unity [10, 38].

Measuring the quantity $\mathcal{A}_{imp}$ for the same temperature calculated using different $\bar{\beta}$ is a rough indicative of the accuracy of the numerical results [10]. More discussion on the estimate of the discretization error is found in Sec. V. C. of Ref. [38].

Now we focus on the analysis of the numerical results for the impurity contribution to the zero-field magnetic susceptibility, which is expressed as [38]:

$$\frac{k_B T \chi_{imp}}{(g\mu_B)^2} = \lim_{N\to\infty} \left[\frac{Tr\left(S_z^2 e^{-\beta_N H_N}\right)}{Z_N} - \frac{Tr_0\left(S_z^2 e^{-\beta_N H_N^{(0)}}\right)}{Z_N^{(0)}} \right], \tag{3.81}$$

where μ_B is the Bohr magneton, g is the Landé g factor, Z_N denotes the system partition function and S_Z is the z component of the total spin of the system. In the remaining of this section we set $k_B = g = \mu_B = 1$ in order to adopt a more compact notation for the susceptibility.

It should be mentioned that close to the fixed points an analytical approach of the impurity properties is available based on a perturbative treatment of the fixed point effective Hamiltonians we mentioned earlier. These results give an important support in the analysis of the numerical data. A good account of the analytical treatment for the Anderson model is encountered in [10, 55] for the metallic case and in [38] for the pseudogap one.

Besides the susceptibility study, the ground state occupation of the system is an important tool to complement the fixed point analysis, which is based on low-energy excitations relative to the ground state. As expected, at high temperatures the Anderson model exhibits charge fluctuations due to population of different n_d subspaces. However, these fluctuations are strongly suppressed as temperature drops below a value $T_F = max(|\epsilon_d|, \Gamma)$ ($U > \Gamma, |\varepsilon_d|$) [38]. In this case the ground state occupation is well described by one of the three configurations [38]: i) local moment $\langle n_d \rangle \approx 1$; ii) empty impurity $\langle n_d \rangle \approx 0$; iii) mixed-valence which involves significant occupation of more than one n_d value. As we will show, a system can flow to the same fixed point but with different ground state occupations.

Figure 25 shows the results obtained from NRG calculations of the magnetic susceptibility for the pseudogap Anderson model for the case of graphene ($r = 1$), with $U = 0.5D$, $\Gamma_0 = 0.016D$ and varying level position ϵ_d (see Fig. 26).

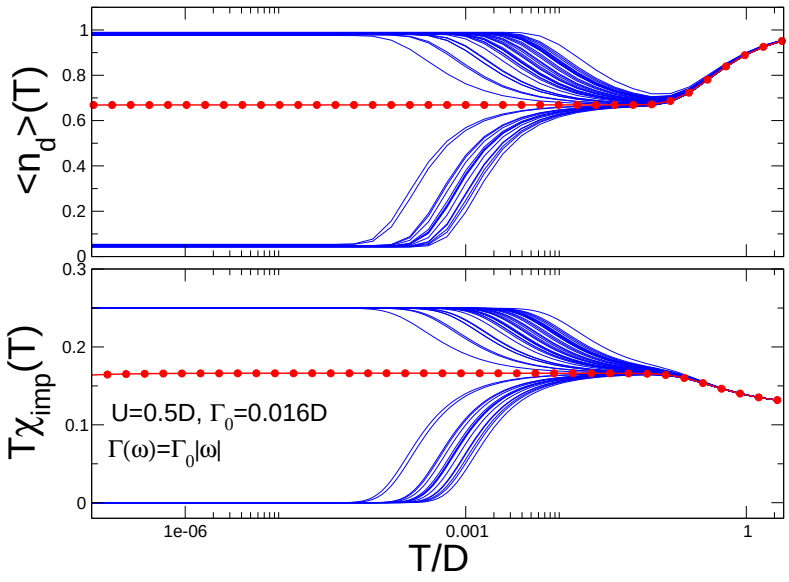

Figure 25: Ground state occupation (top) and impurity susceptibility (bottom) of the pseudogap Anderson model with $r = 1$, $U = 0.5D$, $\Gamma_0 = 0.016D$ and varying level position ϵ_d (see Fig. 26) .

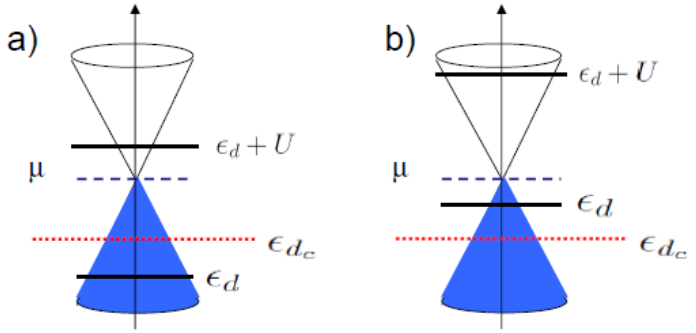

Figure 26: Illustration of the levels positions for the pseudogap model of Fig. 25 for ϵ_d below a) and above b) the critical level ϵ_d.

Here, the low temperature dependency is remarkably distinct from the metallic case (see Figs. 24 and 27 for a comparison). At high temperatures, the system is close to the free orbital fixed point and $T\chi_{imp} \approx 1/8$. As the temperature is lowered, the susceptibility behavior becomes dependent on the position of the impurity level relative to the Fermi energy. Clearly, two distinct regimes appear separated by a curve obtained for the level at the critical energy ϵ_{d_c}.

For $\epsilon_d > \epsilon_{d_c}$, the system flows to the frozen impurity fixed point where $T\chi_{imp} \to 0$. However, no Kondo screening occurs in this situation because the ground state occupation is null and there is no local moment to be screened (see the ground state occupation curves

for $\varepsilon_d > \varepsilon_{d_c}$ in Fig. 25).

The susceptibilities curves for which $\epsilon_d < \epsilon_{d_c}$ flow to $T\chi_{imp} = 1/4$ which is the characteristic value of a free spin 1/2. This is supported by the occupancy curves in Fig. 25 which confirm that a free spin survives all the way down to $T = 0$. This "weak-coupling" limit in which the local moment fixed point is stable is a special aspect of the pseudogap systems [38], as we mentioned when discussing the fixed points of the Anderson model.

Another novelty is the "intermediate-coupling" fixed point at $\epsilon_d = \epsilon_{d_c}$. This characterizes a quantum phase transition which has no counterpart in the metallic case. Also, its behavior is not compatible with any of the other fixed points we discussed and is only obtained through a fine tuning[20] of ϵ_d. Gonzalez-Buxton and Ingersent [38] identified this fixed point as a manifestation in the Anderson model of the fixed point discovered by Withoff and Fradkin in the Kondo model expressed by the critical coupling $J = J_c$ [37].

An extensive study on the importance of the value of the exponent r of the hybridization function and the role played by particle-hole symmetry is found in Ref. [38]. The authors confirm the prediction, originally derived from scaling theory [67], that the local moment ground state configurations is favored by an increase in r at the expense of a shrinking of the parameter space for which the mixed valence phase is attainable. This can be observed in the results of Fig. 25 where the system goes straight from the free-impurity regime to the local moment one (see also Fig. 3 in Ref. [67] and Figs. 7-9 and 12 in Ref. [38]).

For situations of particle-hole symmetry, it was observed that for $r \geq 1/2$ the value of the critical coupling J_c, which the system has to overcome in order to Kondo screen a local moment, diverges (see Fig. 1 of Ref. [68]). If the symmetry is broken, the critical coupling is finite, but Kondo screening gets harder to achieve for increasing r [38, 67, 68]. According to scaling arguments, increasing r implies in a reduction of the coupling J and the condition for Kondo screening $\rho_0 J_c \approx r$ [37] (ρ_0 given in Eq. (3.45)) is restricted to smaller parameters windows for growing r. For $r \geq 1$ scaling indicates that the condition is hardly satisfied (see Fig. 2 in Ref [67]). Numerical results in Refs. [38, 67] give support to those results.

Another important aspect is the observation of two distinct intermediate-coupling fixed points associated to the existence or absence of particle-hole symmetry, denoted as SCR and ACR, respectively. The physics is significantly different whether $r < r^* = 0.3754$

[20] It can also be achieved by fixing ϵ_d and varying U or Γ_0 instead, see Sec. VI in Ref. [38].

where particle-hole symmetry is marginally irrelevant and only SCR exists [38], or $r > r*$ where ACR emerges (see Refs. [38, 39] for a thorough discussion).

We now turn to the analysis of the results of Fig. 27. We see here how the above picture changes in a metallic system.

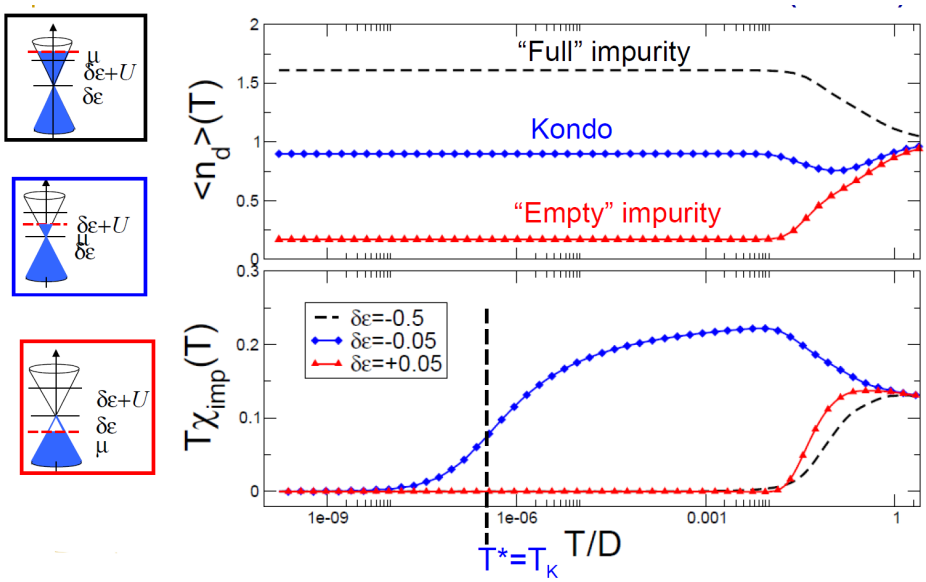

Figure 27: Left: "level" position associated to the "full impurity" (top), "Kondo" (middle) and "empty impurity" (bottom) curves. Right: ground state occupation (top) and impurity susceptibility (bottom) for the metallic Anderson model with $U = 0.5D$, $\Gamma_0 = 0.15D$ and varying "level position" $\delta\epsilon$.

We see that susceptibilities always vanishes in this "vanilla" (conventional) case signalizing that the system always flows to a strong-coupling regime, where any net moment formed is screened.

The importance of the analysis of the ground state occupancy is key here: even though the three curves flow to the strong-coupling regime, each one presents a different ground state configuration[21]. This observation allows one to understand the different behaviors of the curves in Fig. 27.

We first consider the situation represented by the blue curve labeled "Kondo". In this case the impurity is placed at an energy $\delta\epsilon$ $(= \epsilon_d - \mu)$ below the Fermi energy but in such a way that $\delta\epsilon + U$ lies above the Fermi energy $(\epsilon_d + U > 0)$ Fig. 27. The manifold of states for the Anderson Hamiltonian in this configuration is represented in Fig. 28a where the unoccupied and double occupied states are high excited states with respect to the single occupied one.

[21] See also Fig. 1 and discussion on sec. Vl A. 1. in Ref [38].

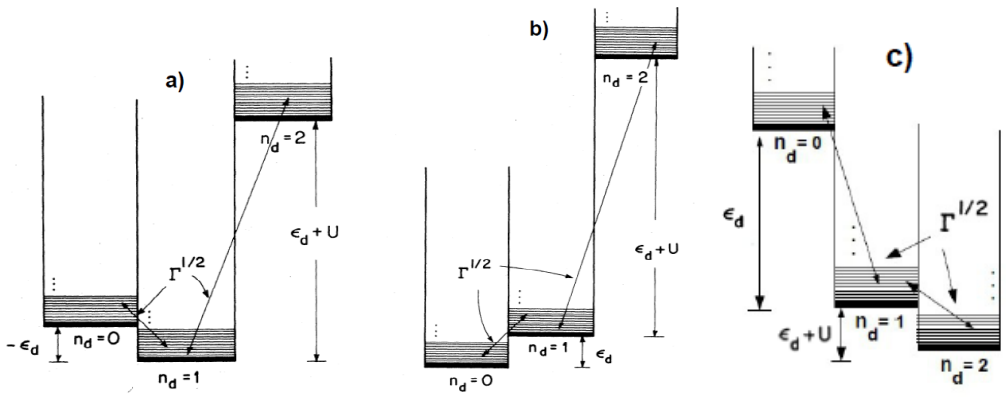

Figure 28: Manifold of states for the "Kondo" a), "empty-empurity" b) and "full-impurity" c) configurations in Fig. 27.

For very high temperatures ($T \gg U$), the three impurity states are effectively degenerate, due to hybridization with conduction electrons, and the free-orbital regime is observed (the region with $T\chi_{imp} \approx 1/8$ in Fig. 27). As temperature drops slightly below D, the $n_d = 2$ subspace is thermally depopulated but $n_d = 0$ and $n_d = 1$ are still equally thermally populated leading the system to the valence-fluctuation regime where $T\chi_{imp} \approx 1/6$. This fixed point is highly unstable and for the parameters used the system is not strongly attracted to this, only touching $T\chi_{imp} \approx 1/6$ and rapidly flowing away from it. Further decrease of temperature depopulates the $n_d = 0$ subspace leaving only $n_d = 1$ subspace thermally available (which explains why the ground state has occupation $\langle n_d \rangle = 1$) and resulting in the formation of a local-moment regime characterized by the climb of the susceptibility until $T\chi_{imp} \approx 1/4$, characteristic of a free spin-1/2. Finally, cooling the system even more leads to the strong-coupling regime where the conduction electrons "freeze" the local moment resulting in a vanishing susceptibility due to the Kondo effect.

The other two curves in Fig. 27 show a high temperature behavior similar to the Kondo curve, the physics is the same as the one we have just discussed above. We focus on the analysis of the low temperature physics.

The black curve, which we call "empty-impurity" for reasons that will be clear soon, corresponds to the choice of a positive value of $\delta\epsilon$ in such a way that the single occupation level will lie above the Fermi sea (Fig. 27 bottom left). The impurity configuration in which $n_d = 0$ now is lower in energy than the $n_d = 1$ case. The manifold of states for the Anderson model is represented in Fig. 28b.

When the system temperature is lowered, the only thermally populated configuration

is the $n_d = 0$ one (which explains the origin of the "empty-impurity" term). This is the reason for the absence of a local moment regime in this case. Instead, the system flows directly from the free-orbital to the frozen-impurity phase. Even though $T\chi_{imp} \to 0$ at low temperatures, the Kondo Effect does not occur since there is no moment to be screened.

The last scenario is the one described by the "full impurity" curve, which represents the situation at which the impurity level is drown in the Fermi sea as shown in Fig. 27 top left.

The level configuration in which $n_d = 2$, whose energy is $2\epsilon_d + U$, now becomes the lowest in energy (see Fig. 28c). If the level is not immersed very deeply, single and double occupancy might be close in energy and eventually become hybridized if the level difference is $\lesssim \Gamma$. This explains why the ground state mean occupancy takes the value close to 1.5. Further immersion of the level into the Fermi sea rise the energy difference between $n_d = 1$ and $n_d = 2$ configurations and the ground state mean occupancy approaches 2 as temperature is lowered.

Here again, as there is no significant net moment, the local moment regime does not develop and the system flow from the free-orbital phase to the strong-coupling without presenting the Kondo Effect.

The Kondo temperature T_K is determined through the criterion $T_K\chi_{imp}(T_K) = 0.0701$ [10]. For the cases where the Kondo screening does not occur, like in the full and empty impurity susceptibility curves of Fig. 27 and in the pseudogap results of Fig. 25, the temperature satisfying the above criterion ($T^*\chi_{imp}(T*) = 0.0701$) is denominated as a crossing temperature T^* which is dissociated from the Kondo Effect.

We now call the attention for two aspects of major relevance concerning the results of Fig. 27. First, it should be noted that, as represented in the left panels of this figure, the metallic Kondo encountered is not associated to a flat band, but to graphene's linear density of states. Obviously, the special features of the pseudogap are "lost"[22] when the Fermi level is displaced away from the Dirac point resulting in a system whose properties resemble those of a metallic system. This observation sheds some light in the fact that the resistivities encountered by the Maryland's group in Fig. 10 fit so well the NRG results derived for the metallic system in Ref. [58].

The second point is that, contrary to the pseudogap susceptibilities that were obtained by varying the level position respective to the Fermi level, the "Kondo", "empty-impurity"

[22] According to Ref. [11], the influence of the pseudogap still has very important consequences on this system.

and "full-impurity" configurations in Fig 27 results from the variation of the Fermi level while keeping the impurity level fixed. This "tunability" of the Kondo effect in graphene is another unusual aspect of this material. It stems from the allowance of the system in being electron/hole doped easily over an appreciable energy range [13].

The issue of the Kondo problem for a system with a linear density of states such as graphene was already addressed in the context of d-wave superconductors [37, 38, 65, 66, 67]. However the tunable character of the Kondo effect in graphene is a unique property (over many other special ones) of this system.

The matter of a tunable Kondo effect was previously addressed by Vojta et al [11] who considered the effect of the gate potential to dope graphene and explored its consequences for the Kondo physics near criticality, which in terms of the Kondo coupling is expressed by the relation $J \approx J_c$.

According to the authors [11], the influence of the asymmetrical critical (ACR) fixed point, encountered for the pseudogap Kondo Model, for $r > r^* = 0.375$ at $\mu = 0$ [38], should also appear in the results obtained for $\mu \neq 0$ as well [11, 39] for the case of graphene, $r = 1$, as shown in the phase diagram of Fig. 29.

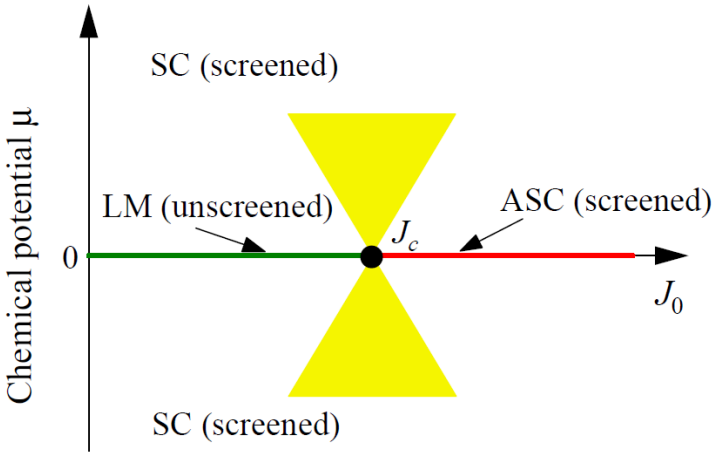

Figure 29: Phase diagram for the pseudogap Kondo impurity with $r = 1$ as a function of doping μ and Kondo coupling J. Close to criticality the doped system still suffers influence from the pseudogap. Extracted from Ref. [11].

They performed an analytical study of the dependence of T_K on μ through a field theory technique applied to a model equivalent to a maximally asymmetric ($U = \infty$) Anderson model, suitable for the description of the ACR fixed point physics [11, 39].

For $r < 1$ the Kondo temperature was found to obey the relation $T_K = \kappa_{\pm}|\mu|$ where

$\kappa_{\pm}$ is a constant factor valid for $\mu \gtrless 0$ [11]. Except for the particle-hole character of the relation, this result keeps great similarity to one derived by scaling arguments which gives $T_K = \kappa|\mu|$ [42] with κ a universal prefactor depending on r [11, 39].

The situation changes drastically for $r = 1$ where a large particle-hole asymmetry manifests in T_K according to the sign of μ. For $\mu < 0$ the former relation still applies, but for positive μ T_K was found to obey $T_K \propto |\mu|^x$ where $x \approx 2.6$ is a universal constant [11, 39].

The special behavior of $r = 1$ is associated to the fact that this case plays the role of an upper critical dimension of the pseudogap Kondo problem (hybridization is relevant (irrelevant) for $r < 1$ ($r > 1$)) and in this case the RG flow presents logarithmic corrections that lead to the distinct behavior of T_K [11, 39].

Support to the analytical treatment results was obtained through the use of NRG calculations [11]. The susceptibilities shown in Fig. 30a are consistent with particle-hole asymmetry showing Kondo screening for $\mu > 0$ and a behavior similar to the full impurity or empty-impurity, we discussed earlier, for $\mu < 0$ [11].

The authors mention that this particle-hole asymmetry is closely related to the asymmetry of the critical fixed point ACR with little influence of particle-hole asymmetry of the hybridization function [11]. It is also argued that due to the relation $T_K \propto |\mu|^x$, the low-energy physics is governed by two distinct scales: μ and T_K [11].

Motivated by the possibility of adsorption of magnetic atoms at the graphene surface and considering DFT results for a Co atom in the center of a graphene hexagon, Ref. [11] constructs a microscopic model and tests their predictions for this model.

The asymmetric behavior of T_K at the critical coupling was confirmed with the observation of linear and power-law dependency of T_K on μ for negative and positive bias, respectively (see Fig. 30b). The system behavior near criticality was also explored and reveals close similarity to the critical one, but with the minimum of T_K at positive bias for $J \neq J_c$ [11].

Although the theory of Kondo effect in doped graphene developed in Ref. [11] presents very interesting results, they are not in accordance with the experimental data of Ref. [1] which presents only a small particle-hole asymmetry in the T_K estimates and these do not show power-law dependency on μ (see Fig. 10). Also, the data fits a single parameter scale which is not consistent with Ref. [11] which predicts the breakdown of single parameter scaling.

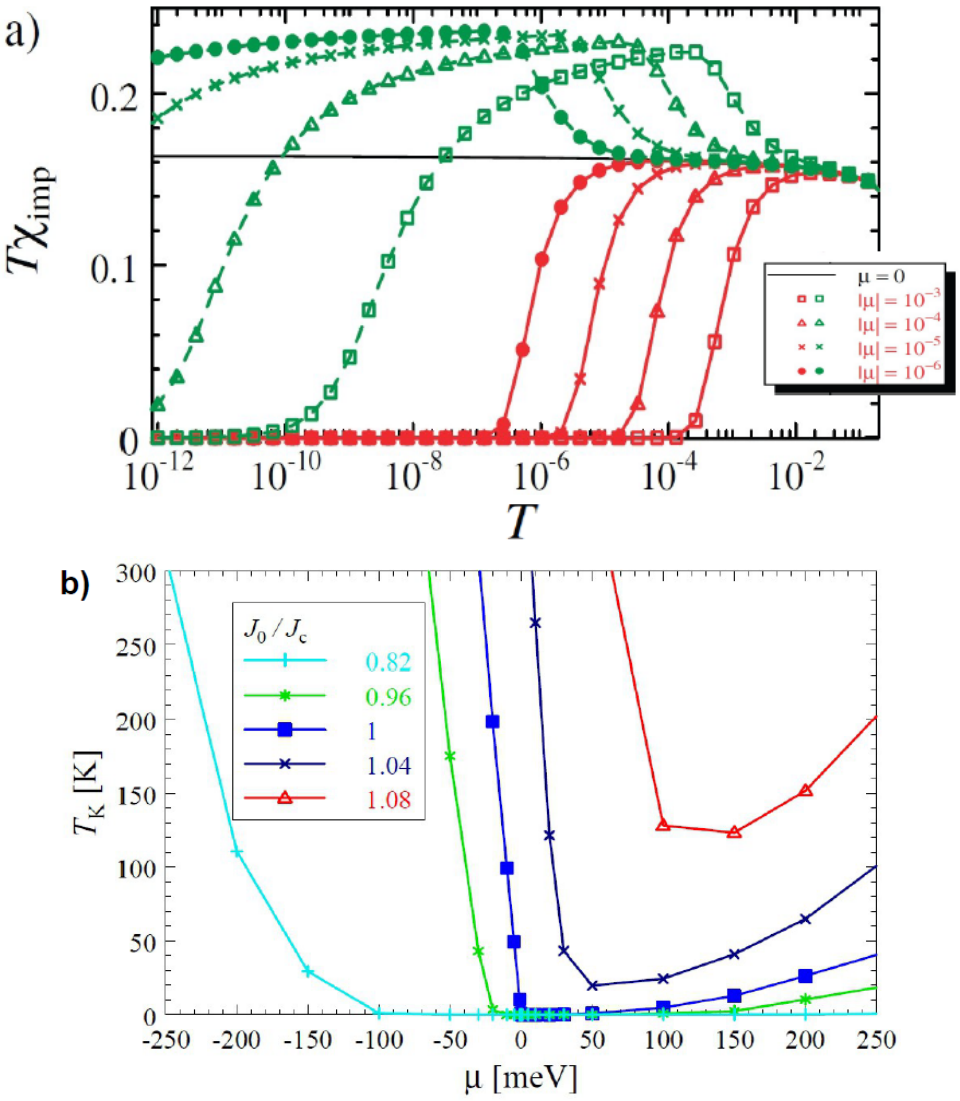

Figure 30: a) Susceptibility curves obtained from NRG for the critical coupling for different chemical potential μ. b) NRG calculated Kondo temperatures as a function of doping for Kondo couplings near criticality. Extracted from Ref. [11].

In the next chapter we put forward an alternative model for studying the effects of vacancies on the Kondo physics of graphene. As we show, there is an important piece which was not considered so far: disorder.

4 *Kondo effect in disordered graphene*

4.1 Nature of the defects

The induction of magnetism in graphene through the introduction of defects in the graphene sheet is a matter of long debate [17, 49, 50]. A particular case of such defects is a vacancy, which is characterized by the removal of a carbon atom from the honeycomb lattice structure (see Fig. 31). This can be achieved through ion irradiation as conducted by the Maryland's group experiment, discussed in Sec. 2. The same setup has been used by other experimental groups [2, 53, 54, 73].

The appearance of magnetic moments due to vacancies was experimentally confirmed [1, 2, 53, 54, 73, 74]. However, the explanations for the origin of this magnetism are still controversial [2, 12, 50, 51, 52, 75, 76, 77, 78], and much of this stems from the complex structure of the vacancy.

In real graphene, the removal of a carbon atom originates three dangling bonds composed of "orphan" σ orbitals which were part of the bond between the removed atom and its nearest neighbors (see Fig. 31a). This structure is highly unstable, and can give origin to different kinds of lattice reconstructions [12, 50, 51, 52, 75, 76, 77, 78], depending whether the graphene is suspended or deposited over a substrate whose mutual interactions play an important contribution to reconstruction. Besides, the dangling bonds are extremely reactive and can easily be passivated by foreign species such as H. Because all these variables, a complete theoretical description of such structure requires extensive ab-initio (DFT) studies.

Many works based on DFT calculations have been put forward to study this issue, but the results are contentious. One of the major discrepancies, for instance, is that magnetic moment varies in estimates in the range $m_B = 1\mu_B - 2\mu_B$ [50, 51, 52, 75, 76, 77, 78]. Magnetic moments greater than $1\mu_B$ are attributed to π and σ contributions to the va-

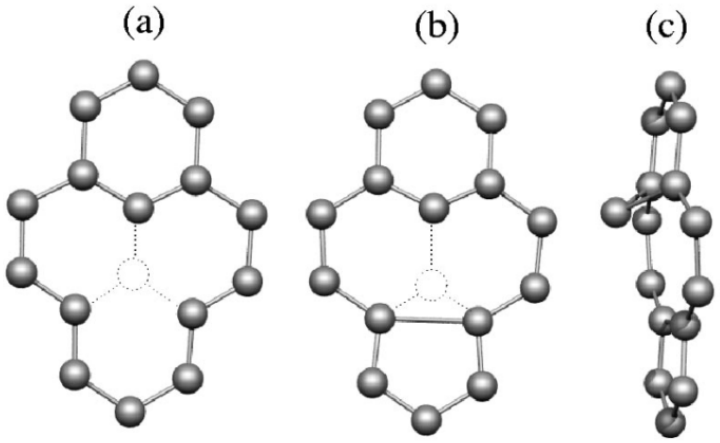

Figure 31: (a) Illustration of a carbon vacancy; (b) Reconstruction after the Jahn-Teller distortion forming a pentagonal structure; (c) Out-of-plane displacement of the apical atom. Extracted from Ref. [12].

cancy magnetism [51, 75, 76, 77, 78]. Other calculations indicate that π magnetism should vanish for any concentration of vacancies realizable in experiments unless the three σ dangling bonds are fully passivated by H [52]. On the other hand, recent experimental results support the scenario of vacancy magnetism as having a twofold contribution emanating from σ and π orbitals [2].

According to DFT, due to Jahn-Teller distortions, two of the dangling bonds reconstruct forming a pentagonal structure (see Fig. 31b). The remaining dangling bond hosts the localized σ orbital and, hence, is responsible for the emergence of the σ magnetism [51]. Whether the apical atom stands in the sheet plane or forms a non-planar structure (see Fig. 31c) is another issue where the DFT results diverge. Most of the more recent DFT results claim that the equilibrium solution is the planar configuration [51, 52, 75, 76] but a very recent study argue that those solutions are very close in energy and the ground state could also be the non-planar configuration [77].

The above discussion is crucial in the context of the Kondo effect, since several works [79, 80, 81, 82] attribute the occurrence of the effect to the quench of the localized σ moment. However, coupling of the conduction π electrons and the σ orbital is only possible in the non-planar scenario [51], the reason is that those studies do not consider other disorder mechanisms, hence, due to orthogonality the coupling does not occur. Also, it was pointed out that magnetism survives only under small distortions of the lattice [75, 78], making the Kondo effect due to σ orbitals more improbable.

The other contribution to vacancy magnetism is the one from the π states. Theory

predicts that the effect of the vacancy in the π band is to create a resonant state in the midgap region which is localized in the majority sublattice and whose wave-function decays like the inverse distance from the vacancy position [51, 83] (a further discussion of this result is given in the next section). The formation of a local moment associated to this state is supported by DFT results [51]. π magnetism is also predicted theoretically by a tight-binding model which shows that after removal of a carbon atom, a substantial amount of magnetization is transferred to the vacancy neighbors [45], however, the study claims that in clean graphene a local moment should remain unscreened down to low temperatures [45].

Once a local moment is formed, by including the Coulomb repulsion and coupling[1] with the conduction band, the ingredients necessary for the rise of the Kondo effect are all set.

Below we propose a model to study the Kondo effect in the context of π local moments. We do not attempt to consider lattice reconstructions. In this way, our modelling amounts to the ideal case where the lattice remains undistorted or, more realistically, that the dangling bonds are all passivated for foreign species such as H. Although this seems to be a great simplification, it is energetically favourable due to the high reactivity of the dangling bonds as was found in the literature [76].

4.2 The model

We investigate the occurrence of Kondo effect due to a single monovacancy in a graphene sheet. The relevance of the model to the experiment [1] is supported by the fact that the irradiated samples used in the experiments were submitted to a irradiation time chosen to guarantee a very diluted concentration of vacancies [1, 2, 53, 56]. Besides, molecular dynamics studies have been developed to simulate and model the behavior of graphene patterned by focused ion beams (FIBs). According to these calculations, irradiation of graphene monolayers by Ne and He up to 1 keV only monovacancies are formed [85].

As we discuss in the sequence, a vacancy gives raise to a localized state that is coupled by disorder to the graphene electronic extended states with a non-uniform DoS.

[1] Although the Kondo effect found in the experiment of Ref. [1] requires a antiferromagnetic coupling, a study based on dynamical mean field theory found a Curie-type susceptibility and attributed that to a ferromagnetic coupling of the impurity and the conduction band [84].

The remaining of this section justifies the elements of the model Hamiltonian we adopt. For that purpose we switch the notation to first quantization.

4.2.1 Localized state

We begin considering a nearest neighbor tight-binding Hamiltonian for a pristine monolayer graphene sheet with a single vacancy at the site v, that reads

$$H_{\mathrm{v}} = -t \sum_{\langle i,j \rangle} |i\rangle\langle j| + t \sum_{\langle \mathrm{v},i \rangle} |\mathrm{v}\rangle\langle i| + \mathrm{H.c.}, \tag{4.1}$$

where $\langle \cdots \rangle$ indicates a sum over nearest-neighbor atomic sites and t is the hopping term. The second term decouples the v-site from the honeycomb lattice. We remove the resulting state from the Hilbert space, mimicking a vacancy.

The solution to the eigenvalue problem

$$H_{\mathrm{v}}|\phi\rangle = \epsilon_{\phi}|\phi\rangle \tag{4.2}$$

gives extended states with non-zero energy $\{|\nu\rangle\}$ and a single zero-energy localized state $|0\rangle$ [4], see Fig. 32. We solve Eq. (4.2) numerically using periodic boundary conditions with supercell sizes $N_i \gg 1$. Since the supercell is very large we consider that the Brillouin zone can be well represented by a single value $\boldsymbol{k} = 0$. In Fig. 32 we show the localized and a typical extended state obtained from our numerical calculations, this is in good agreement with earlier results reported in the literature (see Fig. 4 in Ref. [4]). The black dot in the center of the lattice is the vacancy position and the circles radius on each lattice site are proportional to the wavefunction amplitude at the corresponding site. Thus, larger circles correspond to higher amplitudes. Blue (red) circles denote positive (negative) signs of the amplitude at each site.

For the model Hamiltonian Eq. (4.1), the presence of the zero mode is mathematically guaranteed by a theorem demonstrated in Ref. [4]. According to this theorem, for any bipartite lattice with nearest neighbor interactions plus a local energy (ϵ_A, ϵ_B) for each sublattice, whenever there is an imbalance in the number of sites of the two sublattices $n = N_A - N_B > 0$, there are n degenerate eigensolutions associated to the eigenvalue ϵ_A, the on-site energy of the majority lattice. For neutral graphene $\epsilon_A = 0$, this is the origin of the zero modes, also known as midgap states since they are localized precisely at the Fermi level. Another important characteristic resulting from the theorem is that the zero modes are localized only on the majority sublattice A [4] (an alternative derivation for this

characteristic is found in Ref. [51]). This can be observed in the wavefunction associated to the eigenvalue $\epsilon_0 = 0$, obtained from exact diagonalization of the Hamiltonian Eq. (4.1), displayed in the right panel of Fig. 32.

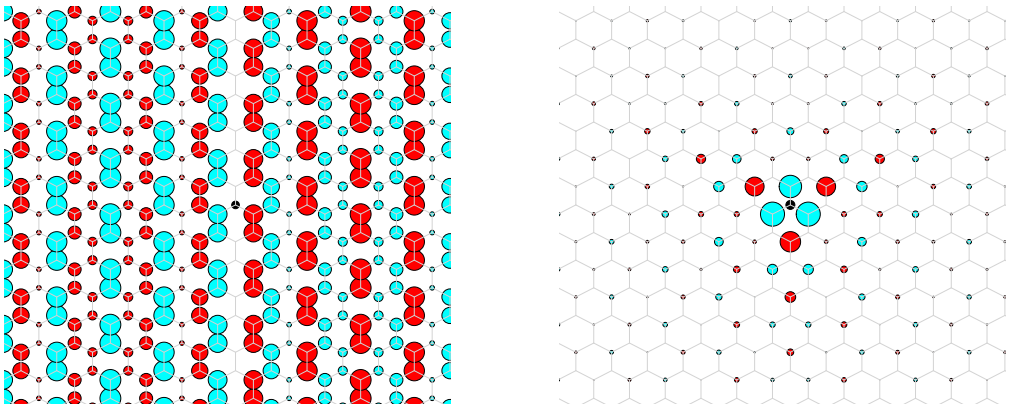

Figure 32: Wave functions of a typical delocalized state (left) and the quasi-localized state (right). The black dot in the center of the lattice denotes the vacancy.

The wave function associated to the midgap state has an approximate analytical form, first derived in Ref. [83], which in coordinate representation reads:

$$\psi_0(x,y) \approx \frac{e^{i\boldsymbol{K'}\cdot\boldsymbol{r}}}{x+iy} + \frac{e^{i\boldsymbol{K}\cdot\boldsymbol{r}}}{x-iy}\,. \tag{4.3}$$

This result was further improved to account for the oscillatory behavior of the wave function due to the interference of the two Dirac cones using the Lippmann-Schwinger equation formalism and modelling the vacancy as (the infinite limit of) a localized impurity potential [51]:

$$\psi_0(\boldsymbol{r}) = \mathcal{N}\frac{\sin\left[(\boldsymbol{K}-\boldsymbol{K'})\cdot\boldsymbol{r}/2 - \theta_r\right]\cos\left[(\boldsymbol{K}+\boldsymbol{K'})\cdot\boldsymbol{r}/2 - \pi/3\right]}{r}, \tag{4.4}$$

where in Eqs. (4.3) and (4.4), $\boldsymbol{K} = 2\pi a^{-1}3^{-3/2}(-1,\sqrt{3})$, $\boldsymbol{K'} = 2\pi a^{-1}3^{-3/2}(1,\sqrt{3})$ denotes the two inequivalent Dirac points in the first Brillouin zone, $\boldsymbol{r}$ is a coordinate vector with origin at the vacancy site, and for the remaining terms in Eq. (4.4), $\mathcal{N}$ is the normalization constant and $\theta_r = \arctan(x/y)$ with x and y denoting the coordinates of the vector $\boldsymbol{r}$.

Our numerics agree with the results derived from Eq. 4.4 making us confident with the supercell size choice.

The important point about the zero-mode wavefunction is that it decays with the

distance from the vacancy as $\sim 1/r$ [see Eqs. (4.3) and (4.4)] and thus has a "quasilocalized" character. This designation was given by the authors of Refs. [4, 83] because, due to the $1/r$ decay, ψ_0 is not normalizable in the limit of infinitely large lattice sizes. The remaining states are delocalized as demonstrated by measurements of the inverse participation ratio (IPR)[2] for those states in Ref. [4] (for more details see Fig. 5a in this work), in good conformation with similar calculations that we performed.

The fact that the eigenstates associated with the vacancy Hamiltonian Eq. (4.1) are represented by a localized state in the Fermi level and the set of extended states has a density of states with a linear dependence is key in the Anderson-like model we construct in the following.

Before introducing interaction and disorder to map Hamiltonian Eq. (4.1) into an Anderson-like one, we should keep in mind that in this study we treat the case of a single vacancy and the experiments deal with diluted vacancies. To make contact with the experiment we assume that hybridization effects between quasilocalized states centered at distinct vacancies are very small due to the $1/r$ decay. Hence, one expects states very similar to the ones given by Eq. (4.3) centered at each vacancy, namely, $\psi_0(\boldsymbol{r}-\boldsymbol{R}_i)$, where $\boldsymbol{R}_i$ is a lattice site.

4.2.2 Mapping into the Anderson Hamiltonian

According to the Hamiltonian Eq. (4.1) the creation of a vacancy provides us a single localized state and a "band" continuum of extended states. Recalling the reasoning of the Anderson modelling we discussed in Sec. 3.1, upon coupling of the localized state with the band and inclusion of Coulomb interactions we have all the necessary ingredients for the onset of localized moments. As we show below, the mapping into the Anderson model is not a straightforward matter because the extended states $\{|\nu\rangle\}$ and the localized one $|0\rangle$ are not coupled. This is easily by seen by introducing projection operators into the extended and localized subspaces, defined as:

$$P = \sum_{\nu \neq 0} |\nu\rangle\langle\nu| \quad \text{and} \quad Q = |0\rangle\langle 0|. \tag{4.5}$$

(P and Q have the usual projector operator properties, namely, $P^2 = P, Q^2 = Q$, and $PQ = QP = 0$) P and Q span the whole Hilbert space and define the completeness

[2]The IPR is a tool to measure the degree of localization of a wavefunction. It is defined as $\mathcal{P}(E_N) = \sum_i |\Psi_n(r_i)|^4$, where n labels the eigenenergies and respective states, and i denotes the sites position. If a state is delocalized $\mathcal{P}(E_N) \sim 1/N$ whereas for a localized state it approaches unity.

relation $P + Q = 1$. Since $H_{\rm v}$ is diagonal in the $\{|\nu\rangle\}, |0\rangle$ basis, $PH_{\rm v}Q = QH_{\rm v}P = 0$. This is one of the ways the algebra tells us that $|0\rangle$ and $|\nu\rangle$ are uncoupled.

If we wish this model to display any Kondo effect, we need a mechanism that couples the vacancy-induced localized state and the π-band states (otherwise the local moment will never be quenched). At this point the contact to the experiment's "real" world plays in our favour once one realize that real samples are disordered. As we show, disorder provides a natural mechanism to couple the localized state $|0\rangle$ to the extended ones, $\{|\nu\rangle\}$. For simplicity we avoid disorder mechanisms that can give additional localized states, potentially obscuring our analysis. For that reason we consider only long range disorder due, for instance, to charge puddles, ripples etc [16].

The modified Hamiltonian that accounts for the presence of disorder is given by

$$H = H_{\rm v} + U_{\rm dis} \tag{4.6}$$

where $U_{\rm dis}$ accounts for long range disorder sources ($U_{\rm dis}$ is addressed in detail in Sec. 4.2.3). The disorder potential $U_{\rm dis}$ can be represented in a site basis. For simplicity, let us assume that $U_{\rm dis}$ is local and write

$$U_{\rm dis} = \sum_{i \neq {\rm v}} |i\rangle U_i \langle i| \tag{4.7}$$

in the site basis.

The Hamiltonian H, Eq. (4.6), can be expressed in terms of P and Q, namely

$$H = (P+Q)H(P+Q) \equiv H_{PP} + H_{PQ} + H_{QP} + H_{QQ}, \tag{4.8}$$

with obvious notational convenience. The projector operator decomposition of Eq. (4.8) separates the single-particle Hamiltonian into three parts. We associate H_{PP} with a band, H_{QQ} with the localized state, and H_{PQ} (H_{QP}) to their coupling.

The Hamiltonian corresponding to the localized state reads

$$H_{QQ} = |0\rangle\langle 0|(H_{\rm v} + U_{\rm dis})|0\rangle\langle 0| = |0\rangle \epsilon_0^{\rm dis} \langle 0| \tag{4.9}$$

since $H_{\rm v}|0\rangle = 0$, $\epsilon_0^{\rm dis} = \langle 0|U_{\rm dis}|0\rangle$. The energy shift of the localized state energy, $\epsilon_0^{\rm dis}$, can be either positive or negative, depending on the disorder realization potential.

The coupling term is written as

$$H_{PQ} = \sum_{\nu} |\nu\rangle\langle\nu|U_{\rm dis}|0\rangle\langle 0|, \tag{4.10}$$

since $H_{\rm v}|0\rangle = 0$.

The projection into extended states reads

$$H_{PP} = \sum_{\nu} |\nu\rangle\epsilon_{\nu}\langle\nu| + \sum_{\nu,\nu'} |\nu\rangle\langle\nu|U_{\rm dis}|\nu'\rangle\langle\nu'|. \tag{4.11}$$

In general $\langle\nu|U_{\rm dis}|\nu'\rangle \neq 0$. Hence, H_{PP} is not diagonal in the $\{|\nu\rangle\}$ basis. To map our model into the single-impurity Anderson model, we still need to diagonalize H_{PP},

$$H_{PP}|\beta\rangle = \epsilon_{\beta}^{\rm dis}|\beta\rangle \tag{4.12}$$

and write the Hamiltonian H in the "new" $\{|\beta\rangle\}$ basis. For that purpose, we introduce the projection operator

$$P' = \sum_{\beta} |\beta\rangle\langle\beta| \tag{4.13}$$

and write the single-particle model hamiltonian as

$$H = H_{P'P'} + H_{P'Q} + H_{QP'} + H_{QQ}. \tag{4.14}$$

While H_{QQ} remains unchanged, the projection of H into extended states now reads

$$H_{P'P'}|\beta\rangle = \epsilon_{\beta}^{\rm dis}|\beta\rangle. \tag{4.15}$$

The β states are all extended by construction, a property that is desirable for the band states. The modified coupling term is

$$H_{P'Q} = \sum_{\beta} |\beta\rangle\langle\beta|U_{\rm dis}|0\rangle\langle 0| \equiv \sum_{\beta} |\beta\rangle t_{\beta 0}\langle 0|, \tag{4.16}$$

where the hopping coefficients $t_{\beta 0} \equiv \langle\beta|U_{\rm dis}|0\rangle$ fluctuate with β and disorder realization.

The terms in Eqs. (4.9), (4.15) and (4.16) can be identified (upon switching to second quantization) with the impurity, hopping and band terms entering the Anderson Hamiltonian in Eq. (3.1). The mapping is complete after inclusion of the charging term U addressed below.

4.2.2.1 Charging energy U

The charging energy U corresponds to the Coulomb energy associated with a double occupation of the localized state $|0\rangle$. It is rather tempting to use the localized wave function $\psi_0(\boldsymbol{r})$ to evaluate U, namely[3] [79]

$$U = e^2 \int d^2r \int d^2r' \, \frac{|\psi_0(\boldsymbol{r})|^2 |\psi_0(\boldsymbol{r}')|^2}{|\boldsymbol{r} - \boldsymbol{r}'|}. \tag{4.17}$$

As we show below this is not correct.

Equation (4.17) gives U in terms of a two-dimensional integral of the electronic density. The latter is expressed as a function of the envelop function $\psi_0(\boldsymbol{r})$ [see Eq. (4.4)]. In what follows we show how the Coulomb interaction obtained from a three-dimensional integral over the charge density is not reduced to Eq. (4.17).

In general, the tight-binding basis is given by [26]:

$$\chi_{\boldsymbol{k}\ell i}(\boldsymbol{r}) = \frac{1}{\sqrt{N}} \sum_{\boldsymbol{R}'} e^{i\boldsymbol{k}\cdot\boldsymbol{R}'} \phi_\ell(\boldsymbol{r} - \boldsymbol{t}_i - \boldsymbol{R}'), \tag{4.18}$$

where $\boldsymbol{t}_i$ is one element of the N_i-dimensional primitive unit cell (PUC) basis and denotes the position of the i-th atom in the PUC, $\boldsymbol{R}'$ is the translation vector, N is the number of unit cells, and $\phi_\ell(\boldsymbol{r})$ is the ℓ-th atomic orbital wave function. Accordingly, the crystal electronic single-particle eigenstates read [26]:

$$\varphi^{(n)}_{\boldsymbol{k}}(\boldsymbol{r}) = \sum_{\ell,i} c^{(n)}_{\boldsymbol{k}\ell i} \, \chi_{\boldsymbol{k}\ell i} \; . \tag{4.19}$$

where n labels the N_i system states.

As standard, we use a single orbital, $\ell = p_z$, to describe the low-energy graphene electronic structure. To address disorder effects, we consider large supercells, $N_i \gg 1$, with periodic boundary conditions. Hence, any $\boldsymbol{k}$ point is representative of the Brillouin zone. We take $\boldsymbol{k} = 0$ to write

$$\chi_i(\boldsymbol{r}) = \frac{1}{\sqrt{N}} \sum_{\boldsymbol{R}'} \phi_{p_z}(\boldsymbol{r} - \boldsymbol{t}_i - \boldsymbol{R}') \tag{4.20}$$

[3] In the calculations of this section, for notation compactness, we write the charging energy U in the vacuum. If graphene is in contact with another medium the calculated expressions should be divided by the corresponding dielectric constant ϵ_0.

(from now on we will omit the index p_z in the orbital ϕ) and

$$\varphi^{(n)}(\boldsymbol{r}) = \sum_i c_i^{(n)} \chi_i(\boldsymbol{r}), \tag{4.21}$$

where

$$c_i^{(n)} = \begin{cases} \langle i|\nu\rangle = \sqrt{\mathcal{A}}\,\psi_\nu(\boldsymbol{r}_i) & \text{for} \quad n = \nu \neq 0, \\ \langle i|0\rangle = \sqrt{\mathcal{A}}\,\psi_0(\boldsymbol{r}_i) & \text{for} \quad n = 0 \end{cases} \tag{4.22}$$

are the wave functions amplitudes on each lattice site obtained from the eigenstates of H_v and $\mathcal{A}$ is the supercell area.

In the tight-binding basis, the charge density associated to the localized state is

$$\rho(\boldsymbol{r}) = e\left|\sum_i c_i^{(0)} \chi_i(\boldsymbol{r})\right|^2 = e\sum_{i,j} c_i^{(0)} \left(c_j^{(0)}\right)^* \chi_i(\boldsymbol{r})\chi_j^*(\boldsymbol{r}). \tag{4.23}$$

Using the tight-binding orthogonal basis approximation

$$\rho(\boldsymbol{r}) \approx e\sum_i \left|c_i^{(0)}\right|^2 |\chi_i(\boldsymbol{r})|^2 \tag{4.24}$$

the charging energy U is written as

$$U = e^2 \sum_{i,j} \left|c_i^{(0)} c_j^{(0)}\right|^2 \int d^3r \int d^3r' \, \frac{|\chi_i(\boldsymbol{r})|^2 |\chi_j(\boldsymbol{r}')|^2}{|\boldsymbol{r} - \boldsymbol{r}'|} \, . \tag{4.25}$$

Next we insert the explicit expression for the tight-binding basis, given by Eq. (4.20), into Eq. (4.25), namely

$$\begin{aligned} \int d^3r \int d^3r' \, \frac{|\chi_i(\boldsymbol{r})|^2 |\chi_j(\boldsymbol{r}')|^2}{|\boldsymbol{r} - \boldsymbol{r}'|} = \int d^3r \int d^3r' \left|\frac{1}{\sqrt{N}} \sum_{\boldsymbol{R}} \phi(\boldsymbol{r} - \boldsymbol{t}_i - \boldsymbol{R})\right|^2 \times \\ \times \frac{1}{|\boldsymbol{r} - \boldsymbol{r}'|} \times \left|\frac{1}{\sqrt{N}} \sum_{\boldsymbol{R}'} \phi(\boldsymbol{r}' - \boldsymbol{t}_j - \boldsymbol{R}')\right|^2 . \end{aligned} \tag{4.26}$$

For $N_i \gg 1$, we neglect contributions of order $1/\sqrt{N_i}$ from atomic orbitals located at the edges of neighboring supercells and assume that the atomic orbital overlap vanishes, unless $\boldsymbol{R} = \boldsymbol{R}'$.

Thus,

$$U = e^2 \sum_{i,j} \left|c_i^{(0)} c_j^{(0)}\right|^2 \int d^3r \int d^3r' \, \frac{|\phi(\boldsymbol{r} - \boldsymbol{t}_i)|^2 |\phi(\boldsymbol{r}' - \boldsymbol{t}_j)|^2}{|\boldsymbol{r} - \boldsymbol{r}'|} \, , \tag{4.27}$$

which, by introducing the change on integration variables $\boldsymbol{r} \to \boldsymbol{r} - \boldsymbol{t}_i$ and $\boldsymbol{r}' \to \boldsymbol{r}' - \boldsymbol{t}_j$, is

more conveniently written as

$$U = e^2 \sum_{i,j} \left| c_i^{(0)} c_j^{(0)} \right|^2 \int d^3r \int d^3r' \, \frac{|\phi(\boldsymbol{r})|^2 |\phi(\boldsymbol{r'})|^2}{|\boldsymbol{r} - \boldsymbol{r'} + \boldsymbol{t}_i - \boldsymbol{t}_j|}. \tag{4.28}$$

We are now ready to relate Eq. (4.17) to Eq. (4.28). Let us explicitly separate the diagonal and the off-diagonal contributions to the sum at the r.h.s. of Eq. (4.28), namely

$$\begin{aligned} U &= U_{\text{diag}} + U_{\text{off}} \\ &= e^2 \sum_i \left| c_i^{(0)} \right|^4 \int d^3r \int d^3r' \, \frac{|\phi(\boldsymbol{r})|^2 |\phi(\boldsymbol{r'})|^2}{|\boldsymbol{r} - \boldsymbol{r'}|} + \\ &+ e^2 \sum_{i \neq j} \left| c_i^{(0)} c_j^{(0)} \right|^2 \int d^3r \int d^3r' \, \frac{|\phi(\boldsymbol{r})|^2 |\phi(\boldsymbol{r'})|^2}{|\boldsymbol{r} - \boldsymbol{r'} + \boldsymbol{t}_i - \boldsymbol{t}_j|}. \end{aligned} \tag{4.29}$$

The diagonal contribution is

$$U_{\text{diag}} = U_{\text{orbital}} \sum_i \left| c_i^{(0)} \right|^4, \tag{4.30}$$

where U_{orbital} is the p-orbital charging energy given by

$$U_{\text{orbital}} = e^2 \int d^3r \int d^3r' \, \frac{|\phi(\boldsymbol{r})|^2 |\phi(\boldsymbol{r'})|^2}{|\boldsymbol{r} - \boldsymbol{r'}|}. \tag{4.31}$$

On the other hand, according to Pereira and collaborators[4] [4],

$$\sum_i \left| c_i^{(0)} \right|^4 \sim \frac{1}{(\log N_i)^2}, \tag{4.32}$$

and thus

$$U_{\text{diag}} \sim \frac{U_{\text{orbital}}}{(\log N_i)^2}. \tag{4.33}$$

The off-diagonal contribution can be written as

$$U_{\text{off}} = e^2 \sum_{i \neq j} \frac{\left| c_i^{(0)} c_j^{(0)} \right|^2}{|\boldsymbol{t}_i - \boldsymbol{t}_j|} \int d^3r \int d^3r' \frac{|\phi(\boldsymbol{r})|^2 |\phi(\boldsymbol{r'})|^2}{\sqrt{1 + \dfrac{|\delta \boldsymbol{r}|^2}{|\boldsymbol{t}_i - \boldsymbol{t}_j|^2} + \dfrac{2 \delta \boldsymbol{r} \cdot (\boldsymbol{t}_i - \boldsymbol{t}_j)}{|\boldsymbol{t}_i - \boldsymbol{t}_j|^2}}}, \tag{4.34}$$

where $\delta \boldsymbol{r} = \boldsymbol{r} - \boldsymbol{r'}$.

The orbital wave functions amplitudes $\phi(\boldsymbol{r})$ decay very quickly for $r/a \gtrsim 1$ (a being the carbon-carbon distance in graphene) and more so the overlaps of the wave functions

[4] Cazalilla et al [79] expresses the scaling in a different manner as $\sim (\ln L)^{-2}$, with L the system's linear size. As $N_i \sim L^2$, due to the ln factor the scaling will be the same for both quantities. When studying the scaling of the charging energy we will adopt the second form, in accordance with Ref. [79]

evaluated at distances $|\boldsymbol{r}-\boldsymbol{r}'|/a \gtrsim 1$. These observations suggest that U_{off} can be approximated by the lowest order Taylor expansion in powers of $|\delta\boldsymbol{r}|/|\delta\boldsymbol{t}|$ of the square root at the r.h.s. of Eq. (4.34). Hence,

$$\begin{aligned} U_{\text{off}} &\approx e^2 \sum_{i\neq j} \frac{\left|c_i^{(0)} c_j^{(0)}\right|^2}{|\delta\boldsymbol{t}|} \int d^3r \int d^3r' \, |\phi(\boldsymbol{r})|^2 |\phi(\boldsymbol{r'})|^2 \\ &\approx e^2 \sum_{i\neq j} \frac{\left|c_i^{(0)} c_j^{(0)}\right|^2}{|\boldsymbol{t}_i-\boldsymbol{t}_j|} \,, \end{aligned} \tag{4.35}$$

since the orbitals are normalized.

By identifying the coefficients $c_i^{(0)}$ with the localized wave function amplitudes given by Eq. (4.4) and using the long wavelength approximation, we obtain the desired result, namely

$$U_{\text{off}} \approx e^2 \int d^2r \int d^2r' \, \frac{|\psi_0(\boldsymbol{r})|^2 |\psi_0(\boldsymbol{r'})|^2}{|\boldsymbol{r}-\boldsymbol{r}'|} \tag{4.36}$$

Note that, as long as $|\delta\boldsymbol{t}| = |\boldsymbol{t}_i - \boldsymbol{t}_j| \gg a$ (distant atoms), the higher order powers of the Taylor expansion are negligible compared to the zeroth order term, and the approximation is accurate. If the atoms are close, higher order terms should be considered to increase the estimates precision.

Hence we have shown that the charging energy U is given by Eq. (4.17) as originally proposed in Ref. [79], plus an additional on-site contribution term given by Eq. (4.33) which has been overlooked so far.

4.2.2.2 Numerical estimates of U_{diag} and U_{off}

Since the typical system sizes achievable in our numerical calculations are much smaller than real graphene flakes, an important issue to consider is how the charging energy scales with the system size. Cazalilla et al [79] propose that U scales with system linear size as[5]:

$$U \sim \frac{e^2}{\epsilon_0 a_0} \left(\frac{1}{2\pi \ln L}\right)^2 \text{ with } \quad \frac{e^2}{\epsilon_0 a_0} \approx 10\text{eV}, \tag{4.37}$$

where in Eq. (4.37) L is the system's linear size and $a_0 \simeq 0.248\,\text{nm}$ is the lattice parameter. The influence of the medium in which graphene is immersed is taken into account through the dielectric constant ϵ_0. The estimate given by Eq. (4.37) is consistent with the dielectric

[5]Strictly speaking this relation is wrong since the argument of the ln should be dimensionless and L has the dimension of a length. A more appropriate manner of writing this term is $\ln(L/a)$, where the linear size is expressed in terms of a reference length such as the carbon-carbon distance a. Note that this do not change the scaling behavior.

constant obtained for graphene deposited on top of SiO_2, $\epsilon = 4$ [17].

We check explicitly the scaling of the system by numerically calculating the diagonal Eq. (4.30) and off-diagonal Eq. (4.35) contributions of the charging energy U for different lattice sizes. Since the experiments of Refs. [1, 2] were realized on top of SiO_2, we take this into account and introduce the dielectric constant of this material into our estimates.

We consider a vacancy at the center of the lattice and the system size is varied from $L = 100, ..., 1000$ in steps of 20 (100 for the larger sizes). The amplitudes at each site, $c_i^{(0)}$, are evaluated from Eq. (4.4) and we recall that distances are measured relative to the vacancy site v. The use of the envelope function Eq. (4.4) is necessary in order to obtain estimates for large system sizes which are not accessible through exact diagonalization of our tight binding Hamiltonian. We have compared the wave functions due to exact diagonalization for small lattice sizes with the envelope functions Eq. (4.4), and we have obtained a very good agreement between them. This result make us confident of adopting the envelope functions for the large system sizes estimates of the charging energy.

Considering first the diagonal term U_{diag} we find that the estimates of $\sum_i |c_i|^4$ in Eq. (4.30) lie in the range $0.017 \leq \sum_i |c_i|^4 \leq 0.037$. The lower (upper) bound corresponds to the size $L = 1000$ ($L = 100$). The term U_{orbital} in Eq. (4.30) has been estimated in the literature as $U_{\text{orbital}} \approx 3.3t = 8.18\,\text{eV}$ for $t \approx 2.8\,\text{eV}$ [86]. This leads to an estimate of U_{diag}:

$$0.139eV \leq U_{\text{diag}} \leq 0.302eV. \tag{4.38}$$

For the off-diagonal term, our numerical calculations find:

$$0.0431 \leq \sum_{i \neq j} \frac{\left| c_i^{(0)} c_j^{(0)} \right|^2}{|\boldsymbol{t}_i - \boldsymbol{t}_j|} \leq 0.0885, \tag{4.39}$$

where the lower (upper) bound corresponds to $L = 1000$ ($L = 100$).

The estimates of U_{off} are obtained multiplying the values we find in Eq. (4.39) by e^2/ϵ_0, where $\epsilon_0 = 4$ for SiO_2 [17]. This leads to:

$$1.859eV \leq U_{\text{off}} \leq 3.723eV. \tag{4.40}$$

In Fig. 33 we plot the separate contribution of each term U_{diag} and U_{off} as a function of the system linear size L. Figure 33 confirms that both contributions to the charging energy follow the scaling predicted in Ref. [79]. According to this, the charging energy vanishes in the $L \to \infty$ limit. This behavior is a consequence of the $1/r$ decay of the

localized state. However, according to our results this decay is slow and we find values of order 1 eV for system sizes up to $L = 1000$ which are already of the order of typical samples (10^6 atoms).

These estimates are consistent with a recent study [86] based on the Hubbard model which points the value $U = 1.6t$ as the value adequate to describe Coulomb interactions in defective graphene. This is also consistent with U estimates found in Refs. [45, 87]. In our calculations we will adopt the value $U = 0.5D$, where $D \sim 3t$ is the half bandwidth, in agreement with the value suggested in Ref. [86] and the estimates we calculate. It should be mentioned that our results are in contrast to those found in Ref. [79], which found $U \sim 1$meV for $L = 10^7$ through evaluation of Eq. (4.37). Values of the same order of magnitude are found for $L = 1000$.

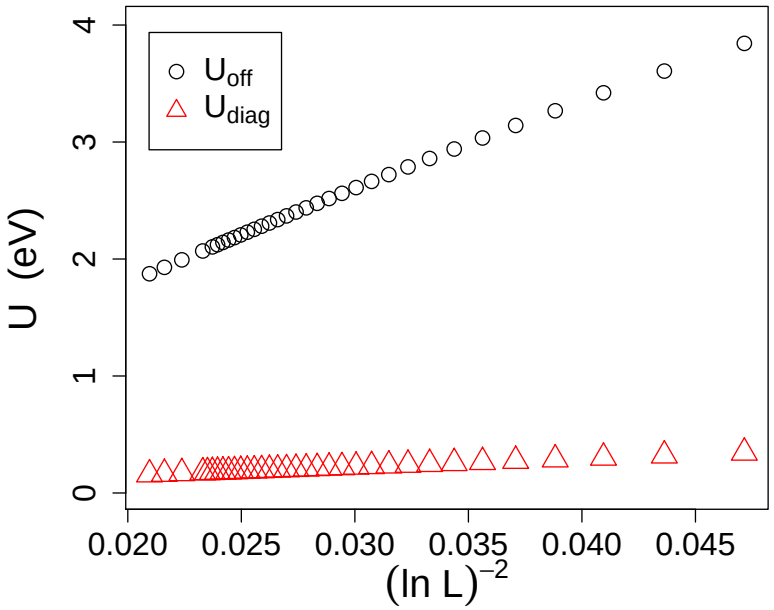

Figure 33: Scaling of the diagonal and off-diagonal charging terms U_{off} and U_{diag} as a function of system size. Circles: off-diagonal contribution. Triangles: estimates of the diagonal term. Values are in eV.

4.2.3 Long Range Disorder Model

In this topic we detail the disorder model we have adopted in our calculations. We assume that the disorder in the graphene sheet, in addition to the single-vacancy, is predominantly due to long-ranged scattering processes. Accordingly, we model the disorder by a random superposition of N_{imp} scattering centers of range $\xi > a$. For simplicity we

model the scatterers by uncorrelated Gaussian-shaped local potentials. The local disorder potential Eq. (4.6) at site i reads

$$U_i \equiv U_{\rm dis}(\boldsymbol{r}_i) = \sum_{j=1}^{N_{\rm imp}} W_j \, e^{\dfrac{-(\boldsymbol{r}_i - \boldsymbol{R}_j)^2}{2\xi^2}}, \tag{4.41}$$

where the jth potential center is placed at $\boldsymbol{R}_j$ corresponding to the position of a lattice site picked at random, while the potential strengths W_j follow a Gaussian distribution with

$$\langle W_i \rangle = 0, \quad \text{and} \quad \langle W_i W_j \rangle = (\delta W)^2 \delta_{ij}. \tag{4.42}$$

Typical values of the parameters ξ, δW and $N_{\rm imp}$ are $\xi \gtrsim 3a$, $\delta W < t$ and $N_{\rm imp} \approx N_i/10$, where a is the carbon-carbon distance in graphene.

The disorder potential covariance reads

$$\langle U_{\rm dis}(\boldsymbol{r}) U_{\rm dis}(\boldsymbol{r}') \rangle = \sum_{i,j=1}^{N_{\rm imp}} \langle W_i W_j \rangle_W \left\langle \exp\left(-\frac{|\boldsymbol{r} - \boldsymbol{R_i}|^2 + |\boldsymbol{r}' - \boldsymbol{R}_j|^2}{2\xi^2} \right) \right\rangle_{\boldsymbol{R}}, \tag{4.43}$$

where $\langle \cdots \rangle_W$ and $\langle \cdots \rangle_{\boldsymbol{R}}$ denote averages over the potential strengths and positions, respectively.

The average over W is straightforward. Using Eq. (4.42) we obtain

$$\langle U_{\rm dis}(\boldsymbol{r}) U_{\rm dis}(\boldsymbol{r}') \rangle = \sum_{i=1}^{N_{\rm imp}} (\delta W)^2 \left\langle \exp\left(-\frac{|\boldsymbol{r} - \boldsymbol{R}_i|^2 + |\boldsymbol{r}' - \boldsymbol{R}_i|^2}{2\xi^2} \right) \right\rangle_{\boldsymbol{R}}. \tag{4.44}$$

Let us now evaluate the average over the positions $\boldsymbol{R}_i$. To this end, it is convenient to write

$$\begin{aligned} |\boldsymbol{r} - \boldsymbol{R}_i|^2 + |\boldsymbol{r}' - \boldsymbol{R}_i|^2 &= 2|\boldsymbol{R}_i|^2 + |\boldsymbol{r}|^2 + |\boldsymbol{r}'|^2 - 2\boldsymbol{R}_i \cdot (\boldsymbol{r} + \boldsymbol{r}') \\ &= 2 \left| \boldsymbol{R}_i - \frac{(\boldsymbol{r} + \boldsymbol{r}')}{2} \right|^2 + \frac{|\boldsymbol{r} - \boldsymbol{r}'|^2}{2}. \end{aligned} \tag{4.45}$$

and to insert Eq. (4.45) into Eq. (4.44), namely,

$$\langle U_{\rm dis}(\boldsymbol{r}) U_{\rm dis}(\boldsymbol{r}') \rangle = (\delta W)^2 \, e^{-\dfrac{|\boldsymbol{r} - \boldsymbol{r}'|^2}{4\xi^2}} \sum_{i=1}^{N_{\rm imp}} \left\langle e^{-\dfrac{2\,|\boldsymbol{R}_i - (\boldsymbol{r} + \boldsymbol{r}')/2|^2}{2\xi^2}} \right\rangle_{\boldsymbol{R}}. \tag{4.46}$$

Since the $\{\boldsymbol{R}_i\}$ follow an uniform distribution over the graphene sheet area $\mathcal{A}$, we write

$$\left\langle e^{-\frac{|\boldsymbol{R}_i-(\boldsymbol{r}+\boldsymbol{r}')/2|^2}{\xi^2}}\right\rangle_{\boldsymbol{R}} = \frac{1}{\mathcal{A}}\int_{\mathcal{A}} d\boldsymbol{R}_i\, e^{-\frac{|\boldsymbol{R}_i-(\boldsymbol{r}+\boldsymbol{r}')/2|^2}{\xi^2}}. \tag{4.47}$$

The above integral is simplified by changing the integration variables, namely, $\boldsymbol{R}_i' = \boldsymbol{R}_i - (\boldsymbol{r}+\boldsymbol{r}')/2$. Equation (4.47) now reads

$$\left\langle e^{-\frac{|\boldsymbol{R}_i-(\boldsymbol{r}+\boldsymbol{r}')/2|^2}{\xi^2}}\right\rangle_{\boldsymbol{R}} = \frac{1}{\mathcal{A}}\int_{\mathcal{A}} d\boldsymbol{R}_i'\, e^{-\frac{|\boldsymbol{R}_i'|^2}{\xi^2}}. \tag{4.48}$$

Since $\xi/\mathcal{A}^{1/2} \ll 1$, the Gaussian scattering centers close to the graphene sheet edges give only a small contribution to Eq. (4.48). Hence, it is accurate to write

$$\frac{1}{\mathcal{A}}\int_{\mathcal{A}} d\boldsymbol{R}_i'\, e^{-\frac{|\boldsymbol{R}_i'|^2}{\xi^2}} \approx \frac{1}{\mathcal{A}}\left[\int_{-\infty}^{\infty} dx\, e^{-\frac{x^2}{\xi^2}}\right]^2 = \frac{1}{\mathcal{A}}(\sqrt{\pi}\xi)^2 = \frac{\pi\xi^2}{\mathcal{A}}. \tag{4.49}$$

Finally, collecting the result Eq. (4.49) and inserting into Eq. (4.46), we obtain

$$\langle U_{\rm dis}(\boldsymbol{r})U_{\rm dis}(\boldsymbol{r}')\rangle = \pi\xi^2(\delta W)^2\frac{N_{\rm imp}}{\mathcal{A}}\, e^{-\frac{|\boldsymbol{r}-\boldsymbol{r}'|^2}{4\xi^2}}. \tag{4.50}$$

The above equation justifies why this model is frequently called Gaussian correlated disorder model.

4.2.4 NRG inputs

The tight-binding model Eq. (4.6) provides the inputs necessary for the implementation of the NRG method, namely, localized state energy $\epsilon_0^{\rm dis}$, the hoppings $t_{\beta 0}$ and the β-states eigenvalues ϵ_β. The eigenvalues ϵ_β will be used to construct the density of states of the disordered system $\rho_{\rm dis}(\omega)$ (ω being the energy measured from the Fermi level[6]) which is key in the calculation of the hybridization function $\Gamma_{\rm dis}(\omega) = \pi\sum_\beta |t_{\beta 0}|^2\delta(\omega-\epsilon_\beta)$, the central quantity in the NRG.

As we saw in Sec. 3.4, the NRG method is the tool that allows to calculate the impurity (here represented by the vacancy) properties. In our approach, input parameters necessary for the NRG implementation are generated after each disorder realization and

[6]This notation will be useful when we introduce the chemical potential in our NRG simulations discussed in Sec. 4.3.

the calculations of these inputs are described below.

4.2.4.1 Calculation of $\epsilon_0^{\mathbf{dis}}$

The localized state energy $\epsilon_0^{\rm dis}$ reads

$$\epsilon_0^{\rm dis} = \langle 0|U_{\rm dis}|0\rangle = \sum_i \langle 0|i\rangle U_i \langle i|0\rangle \tag{4.51}$$

In Fig. 34 we plot the distribution of the localized energies $\epsilon_0^{\rm dis}$ obtained after $N_r = 10^3$ disorder realizations with $\delta W = t/10$, range $\xi = 3a$ and two distinct numbers of scattering centers: $N_{imp} = N_i/10$ (top panel) and $N_{imp} = N_i/100$ (bottom panel), where $N_i = 20\,\mathrm{x}\,20$. The results show that the localized energies typically follow a Gaussian-like distribution. This same behavior is observed with different disorder parameters.

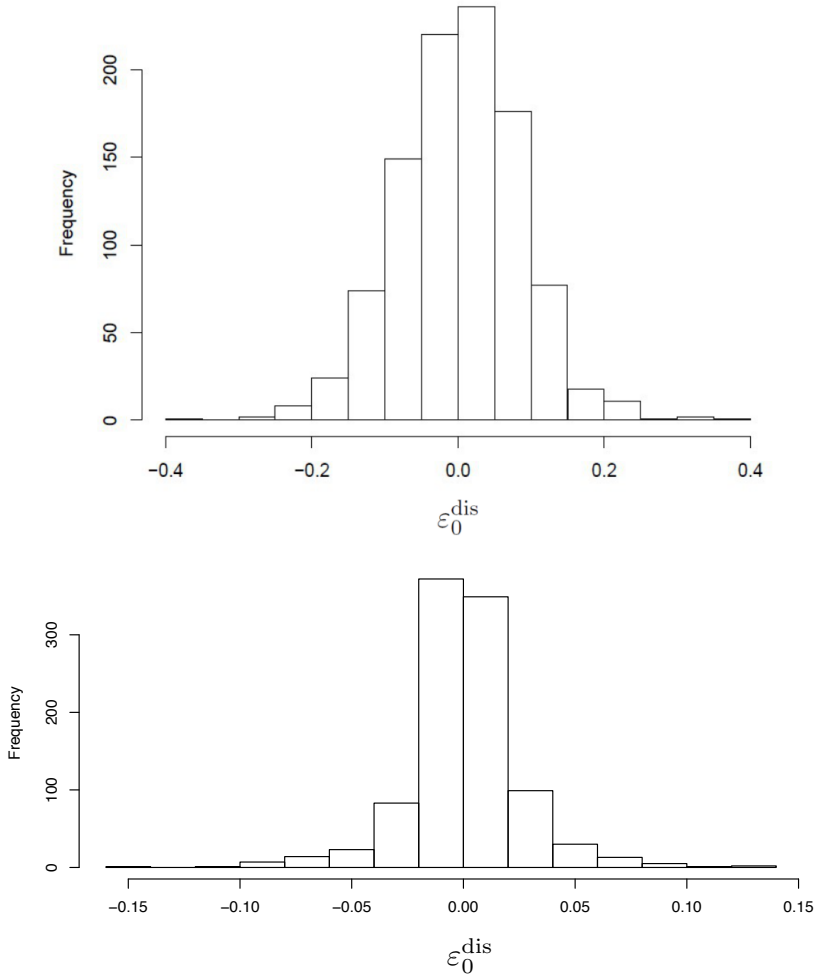

Figure 34: Distribution (not normalized) of localized state energy $\epsilon_0^{\rm dis}$ (in eV). Histograms obtained for two distinct sets of parameters, $\delta W = t/10$, $\xi = 3a$ and $N_{\rm imp} = N_i/10$ (top) and $N_{\rm imp} = N_i/10$ (bottom). We also run simulations with other parameters and always observed Gaussian-like distributions (obviously) with different widths.

4.2.4.2 Calculation of $\rho_{\mathrm{dis}}(\omega)$

We obtain the density of states $\rho_{\mathrm{dis}}(\omega) = \sum_\beta \delta(\omega - \epsilon_\beta)$ of the disordered system by directly calculating the number of tight-binding states[7] $N(\omega)$ between energies $E - \Delta E/2$ and $E + \Delta E/2$ and then approximating $\rho_{\mathrm{dis}}(\omega) \approx N(\omega)/\Delta E$. Due to the finite size effects (finite PUC and few k-points), the spectrum of the ϵ_β has a small gap at low energies (see, e.g., Fig. 36). Therefore, the choice of ΔE is a compromise between the enhancement of the fluctuations due to disorder and the smearing of the finite-size gap. As shown in Fig. 35, choosing $\Delta E = 0.1D$ ($D \sim 3t$ the half bandwidth) gives reasonable results, displaying the familiar linear behavior of the graphene density of states at low energies (see the inset of Fig. 35).

We note that due to the small gap at low energies it is essential the calculation of the continuous curve of $\rho_{\mathrm{dis}}(\omega)$. This stems from the fact that the NRG requires access to very low energy values to construct a Wilson chain with a suitable number of sites to allow a full characterization of the low energy behavior of the system. The chain obtained straight from the tight-binding eigenvalues contains only a reduced number of sites, hence the necessity for the continuous approximation of $\rho_{\mathrm{dis}}(\omega)$.

4.2.4.3 Calculation of $t_{\beta 0}$

Recalling that U_{dis} is represented in the atomic sites basis, it is useful to write the states $|\beta\rangle$ and $|0\rangle$ in terms of $|i\rangle$. As a result of the diagonalization of H_{v}, the transformations

$$|\nu\rangle = \sum_i |i\rangle\langle i|\nu\rangle \quad \text{and} \quad |0\rangle = \sum_i |i\rangle\langle i|0\rangle \tag{4.52}$$

are known. Likewise, the unitary transformation

$$|\beta\rangle = \sum_\nu |\nu\rangle\langle\nu|\beta\rangle \tag{4.53}$$

is obtained from the diagonalization of H_{PP}.

Hence,

$$\begin{aligned} t_{\beta 0} =& \langle\beta|U_{\mathrm{dis}}|0\rangle \\ =& \sum_{i,i'} \langle\beta|i\rangle\langle i|U_{\mathrm{dis}}|i'\rangle\langle i'|0\rangle = \sum_i \langle\beta|i\rangle U_i \langle i|0\rangle. \end{aligned} \tag{4.54}$$

[7] The eigenvalues ϵ_β are calculated through diagonalization of the band term Eq. (4.11). In this process, the largest supercell we used has size $N = 40 \times 40$ and we used a single $\boldsymbol{k} = 0$ point.

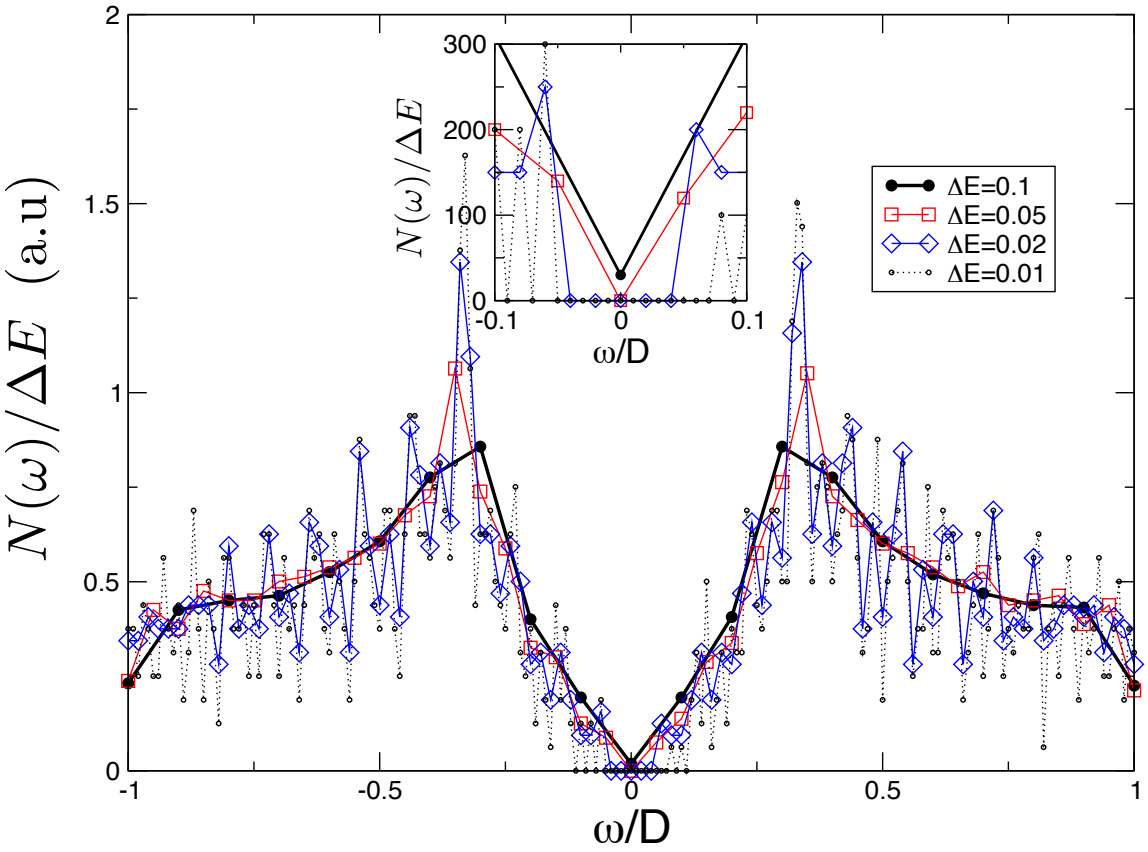

Figure 35: Density of states $N(\omega)/\Delta E$ (normalized by the total number of states) for a single realization and different choices of ΔE

The coefficients $\langle\beta|i\rangle$ are obtained from Eq. (4.53), namely

$$\langle i|\beta\rangle = \sum_{\nu}\langle i|\nu\rangle\langle\nu|\beta\rangle \tag{4.55}$$

In Fig. 36 two typical outcomes of the squared hoppings $|t_{\beta 0}|^2$ are displayed. The small energy gap discussed above is seen close to zero energy and is attributable to finite size effects. The results show that disorder couples the midgap state with states overall the energy range of band. The smoothed curve represented by the filled squares in the top panel of Fig. 36 denotes the quantity $|t(\omega)|^2$, defined as the average of $|t_{\beta 0}|^2$ in the window $\omega - \Delta E/2 \leq \epsilon_\beta \leq \omega + \Delta E/2$ using the same ΔE adopted in the calculation of $\rho_{\rm dis}(\omega)$. The result shows that $|t(\omega)|^2$ is essentially independent of energy for large ω but quite sensitive to the fluctuations in small energy windows (compare panels (a) and (b) in Fig. 37), since the number of states in this region is relatively small, leading to important consequences for the Kondo physics once this is the region of interest for the effect.

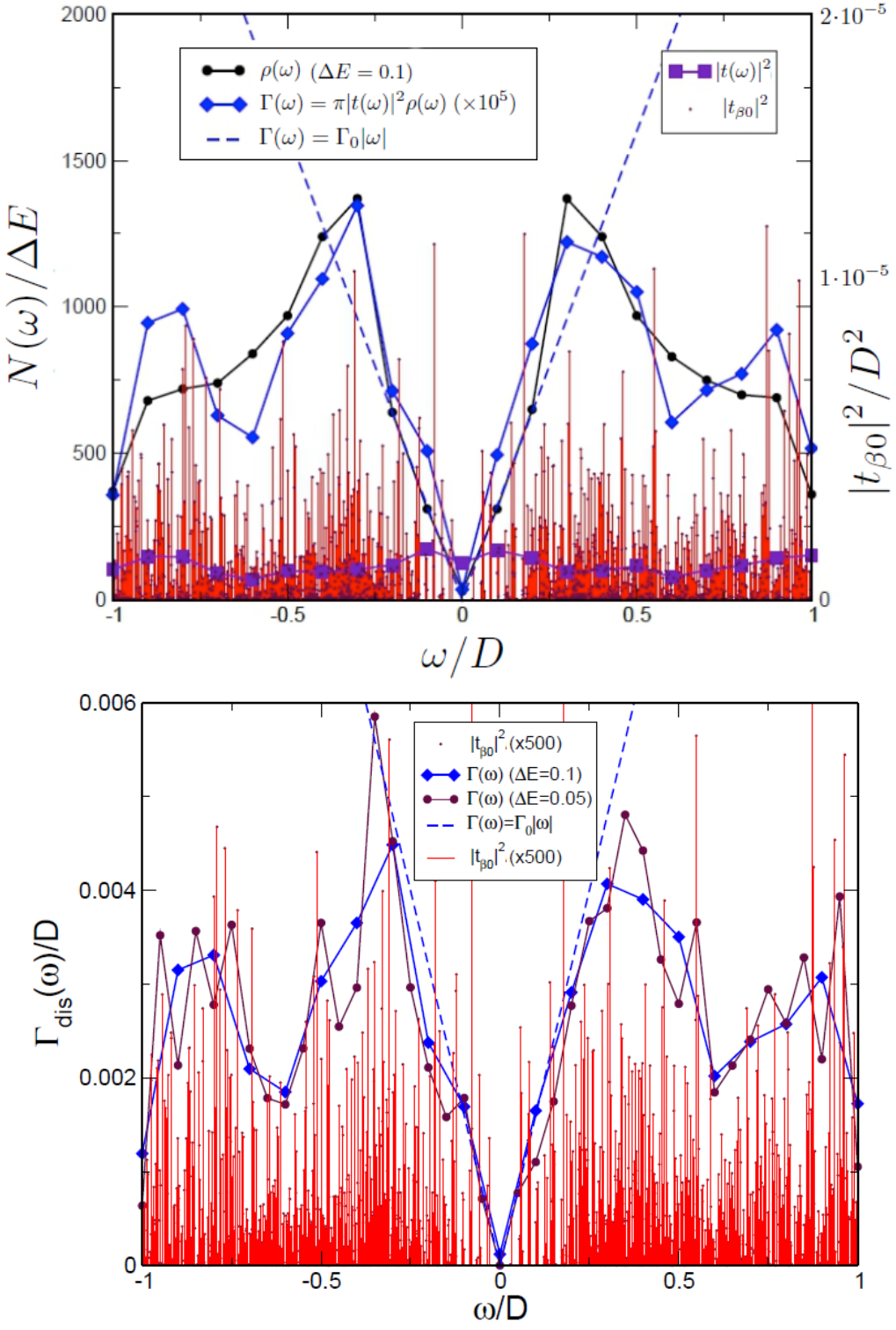

Figure 36: (a) Raw data for $|t_{\beta 0}|^2$ in a single realization (dots) and the corresponding energy-averaged $|t(\omega)|^2$ (filled squares). Also shown: density of states $\rho_{\rm dis}(\omega)$ and the resulting hybridization function $\Gamma_{\rm dis}(\omega) \equiv \pi|t(\omega)|^2\rho_{\rm dis}(\omega)$. (b) $\Gamma_{\rm dis}(\omega)$ for different choices of ΔE.

With the necessary parameters to implement the NRG at hand, in the following we discuss the results obtained by this method.

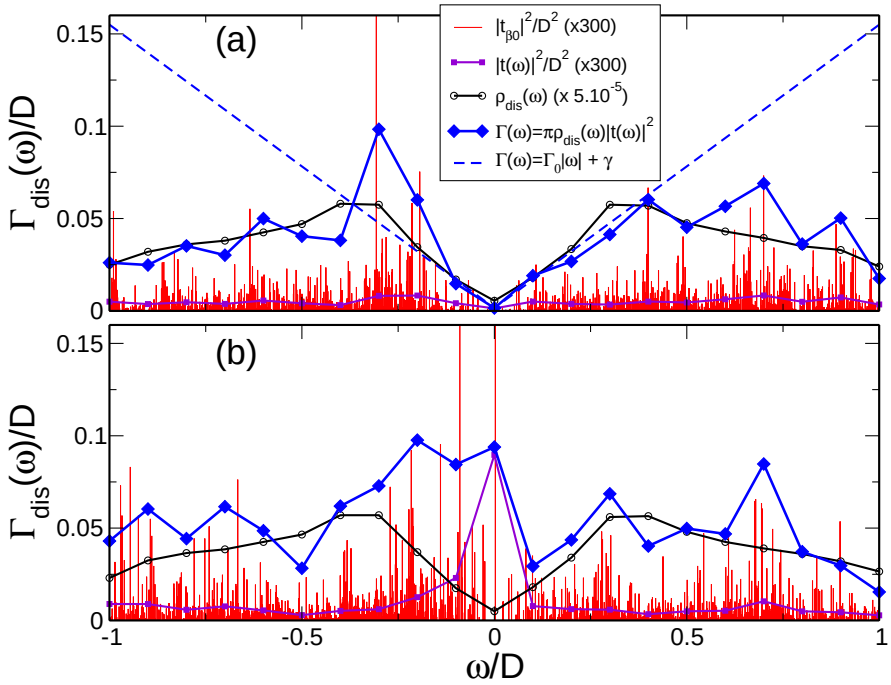

Figure 37: Illustration of the low energy fluctuations on the hoppings $|t(\omega)|^2$ and how this influences the hybridization function estimates in this region. For some realizations, panel (b), strong fluctuations leads to a non-linear behavior in $\Gamma(\omega)$. In this cases, the "metallic" character $\Gamma_{\rm dis}(\omega = 0) \neq 0$ of the system is emphasized.

4.3 NRG calculations

The arguments presented in the previous section justify the use of the Anderson-like model of a localized state coupled to a continuum band with a density of states $\rho_{\rm dis}(\omega)$. The variable $\omega = \epsilon - \mu(V_g)$ is suitable for treating the cases with nonzero doping. The energy ω varies within the range $-D - \Delta\mu \leq \omega \leq D - \Delta\mu$, where $\Delta\mu = \mu(V_g) - \mu_0$ is the change in the Fermi level energy, set by the introduction of gate voltage V_g, relative to charge neutrality and D is the half-bandwidth.

The model Hamiltonian is written as $H_A = H_{\rm state} + H_{\rm band} + H_{\rm hop}$ where, in energy

representation[8],

$$\begin{aligned} H_{\text{state}} &= \delta\varepsilon\ n_{0\sigma} + U n_{0\uparrow} n_{0\downarrow} \\ H_{\text{band}} &= \int_{-D-\Delta\mu}^{D-\Delta\mu} d\omega\ \omega\ c^{\dagger}_{\omega\sigma} c_{\omega\sigma} \\ H_{\text{hop}} &= \int_{-D-\Delta\mu}^{D-\Delta\mu} d\omega \sqrt{\Gamma_{\text{dis}}(\omega)/\pi} \left(c^{\dagger}_{0\sigma} c_{\omega\sigma} + \text{h.c.} \right) , \end{aligned} \tag{4.56}$$

where $\delta\varepsilon = \epsilon_0^{\text{dis}} - \mu(V_g)$ is the midgap state energy relative to the Fermi level, located at $\mu(V_g)$, U is the Coulomb repulsion at the localized state (see Sec. 4.2.2.1), $c^{\dagger}_{0\sigma}$ ($c_{0\sigma}$) is the creation (destruction)[9] operator of an electron with spin σ at the $|0\rangle$ state ($n_{0\sigma} = c^{\dagger}_{0\sigma} c_{0\sigma}$ is the number operator). The electron band states β are treated in the energy representation. Accordingly, $c^{\dagger}_{\omega\sigma}$ ($c_{\omega\sigma}$) is a creation (destruction) operator of an electron with spin σ and energy ω in the (disordered) graphene band. The coupling between the band and the localized state is written in terms of an energy-dependent hybridization function $\Gamma_{\text{dis}}(\omega) = \pi \sum_{\beta} |t_{\beta 0}|^2 \delta(\omega - \epsilon_{\beta})$, which will undergo the standard NRG logarithmic discretization of the conduction band [9, 38] we discussed in Sec. 3.4.

4.3.1 "Weak disorder" toy model

Before addressing the effects of disorder, it is instructive to consider a simple toy model. This will give support to the analysis we present for the disordered case. In the absence of disorder or vacancies the band density of states is written as:

$$\rho(\omega) = \rho_0 |\omega - \Delta\mu|. \tag{4.57}$$

We consider that the hybridization function is given by $\Gamma(\omega) = \pi |t_{\text{hop}}|^2 \rho(\omega) = \Gamma_0 |\omega - \Delta\mu|$ and $\Gamma_0 = \pi t_{\text{hop}}^2 \rho_0$, where Γ_0 is chosen as the hybridization energy scale at the band edge [38]. At this point, the choice of Γ_0 seems rather arbitrary. It will be justified when we discuss the effects of disorder on the determination of the hybridization function.

In this simple model, both ρ and Γ are linear in ω (see dashed curve in Figs. 36 and 37a) and disorder manifests only through a variation in the energy ϵ_0^{dis}. We call this the "weak disorder" limit. Note that when $\Delta\mu = 0$ (charge neutrality point) we have a realization of the pseudogap model we discussed earlier (see Sec. 3.4).

By setting $\Gamma(\omega) = \Gamma_0$, the model displays the metallic behavior characterized in Figs.

[8] This is the same procedure carried out in Sec. 3.4.2.1.

[9] We adopt this notation, instead of the one with the d subscript used earlier, in allusion to the vacancy-induced localized state.

38a-b (compare with Figs. 24 and 27). Model parameters are $\Gamma_0 = 0.016D$, $U = 0.5D$, $-0.25D \leq \delta\varepsilon \leq 0.25D$ and the step in $\delta\varepsilon$ equals $0.01D$. The results show that as the impurity level gets more immersed into the Fermi sea (decreasing $\delta\varepsilon$) the system goes from the empty-orbital ($\langle n_0 \rangle \sim 0$) to the Kondo regime ($\langle n_0 \rangle \sim 1$), crossing a region of mixed valence ($0.25 \lesssim \langle n_0 \rangle \lesssim 0.75$). The magnetic susceptibility $T\chi_{\rm imp}(T)$ (we are setting $k_B = g = \mu_B = 1$) always vanishes[10] as $T \to 0$ (see Fig. 38b) in agreement with the discussion presented in Sec. 3.4.4. Kondo screening occurs for $\delta\varepsilon < 0$, but sufficiently apart from $\delta\varepsilon = 0$ to enter the Kondo regime. For the more general case $\Gamma(\omega) = \Gamma_0|\omega|$, the model reproduces the magnetic susceptibility and ground state occupation for the pseudogap situation as presented in Figs. 38c-d (see also Fig. 25), where $\Gamma_0 = 0.016D$ and $-0.02D \lesssim \delta\varepsilon \lesssim -0.0001D$. The system presents a quantum phase transition at $\delta\varepsilon = \delta\varepsilon_c = -0.00253724D$ separating the empty-orbital ($\delta\varepsilon > \delta\varepsilon_c$) and local moment phases ($\delta\varepsilon < \delta\varepsilon_c$). Note the absence of intermediate values of the occupation $\langle n_0 \rangle$ for this case, consistent with what is expected for pseudogaped systems with small Γ_0 values [38]. The physics background of these results was discussed in Sec. 3.4. Here we focus on the results of such model to help in the interpretation of the disordered scenario we present below.

4.3.2 Disordered case

We now consider the disordered case, in which the (realization-dependent) parameters from tight-binding calculations ($\epsilon_0^{\rm dis}$, ϵ_β and $|t_{\beta 0}|^2$) enter the model either directly or through the hybridization function $\Gamma_{\rm dis}(\omega)$. Those effects are realization-dependent and thus one can think in terms of a disordered effective Anderson model [88, 89, 90, 91] describing the low-energy physics of the system. Hence, for a given disorder realization, the first step in the NRG analysis is to obtain an energy-dependent hybridization function $\Gamma_{\rm dis}(\omega)$ from the tight-binding results.

For each disorder realization, the hybridization is constructed from the effective couplings $|t(\omega)|^2$ and the disordered density of states $\rho_{\rm dis}(\omega)$, derived in Secs. 4.2.4.2 and 4.2.4.3, and reads $\Gamma_{\rm dis}(\omega) \approx \pi|t(\omega)|^2\rho_{\rm dis}(\omega)$ (see the diamonds in Figs. 36 and 37). The choice of the parameter ΔE used to determine $|t(\omega)|^2$ and $\rho_{\rm dis}(\omega)$ has little influence on the low-energy part of $\Gamma_{\rm dis}(\omega)$ (compare curves in the bottom panel of Fig. 36) as long as ΔE is small, typically of order of the finite-size-induced gap. In Fig. 39 one sees that

[10] In the scale of Fig. 38b, the lowest temperature value shown is $T = 10^{-7}D$. Some of the blue curves have T_K lower than this value. The susceptibilities vanish in these cases when simulations are carried out down to $T = 10^{-14}D$.

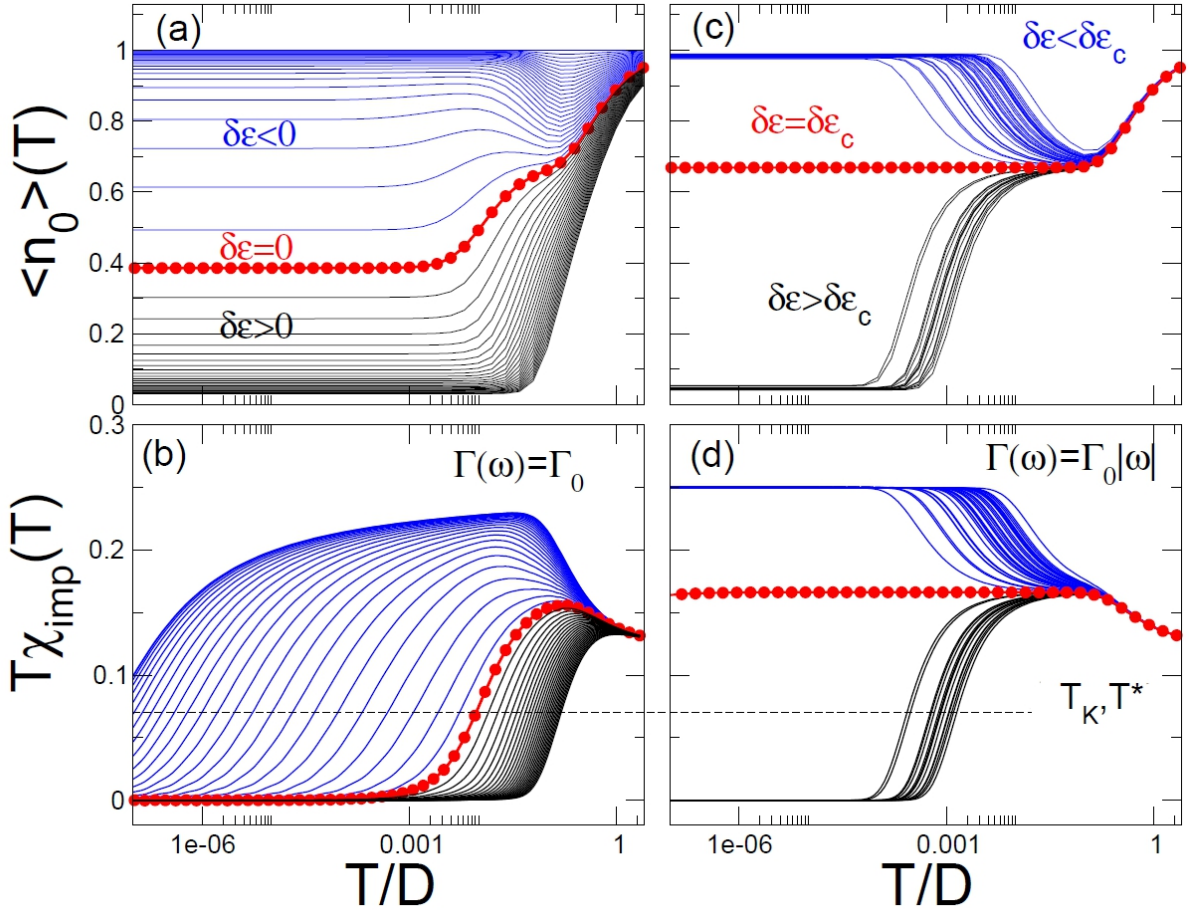

Figure 38: Level occupation $\langle n_0\rangle(T)$ (a,c) and impurity magnetic susceptibility $T\chi_{\rm imp}(T)$ (b,d) for the metallic (left panels) and pseudogap (right) Anderson models. In the pseudogap model, a quantum phase transition (QPT) occurs at $\delta\epsilon = \delta\epsilon_c$ separating empty-orbital ($\langle n_0\rangle(T\to 0) \sim 0$ and $T\chi_{\rm imp}(T\to 0) \sim 0$ for $\delta\epsilon > \delta\epsilon_c$) and local-moment ($\langle n_0\rangle(T\to 0) \sim 1$ and $T\chi_{\rm imp}(T\to 0) \sim \frac{1}{4}$ for $\delta\epsilon < \delta\epsilon_c$) phases. This is in contrast with the smooth crossover from Kondo screening to the empty-orbital regime in the metallic Anderson model (a,b).

the behavior of $\Gamma_{\rm dis}(\omega)$ suffers a strong influence from the hoppings fluctuations in the low-energy region. We see that the disordered hybridization functions obtained (dashed lines) can be expressed as $\Gamma_{\rm dis}(\omega) \approx \Gamma_0(\omega) + \gamma$, meaning that disorder not only implies in different inclinations but also to a filling of the pseudogap γ. This mechanism is the one responsible for giving a "metallic" character to the disordered system. Figure 37b illustrates that in some cases such fluctuations can lead to a large nonzero value of $\Gamma_{\rm dis}(\omega = 0)$ and a nonlinear behavior of $\Gamma_{\rm dis}(\omega)$ at $\omega \approx 0$ (this occurs at a small number $5-10$ percent of the disorder realizations). In these cases the "metallic" character of $\Gamma_{\rm dis}(\omega)$ is reinforced. Since the density of states, in general, retain its characteristic linear energy dependence in this region, the effect is exclusively due to the hoppings fluctuations.

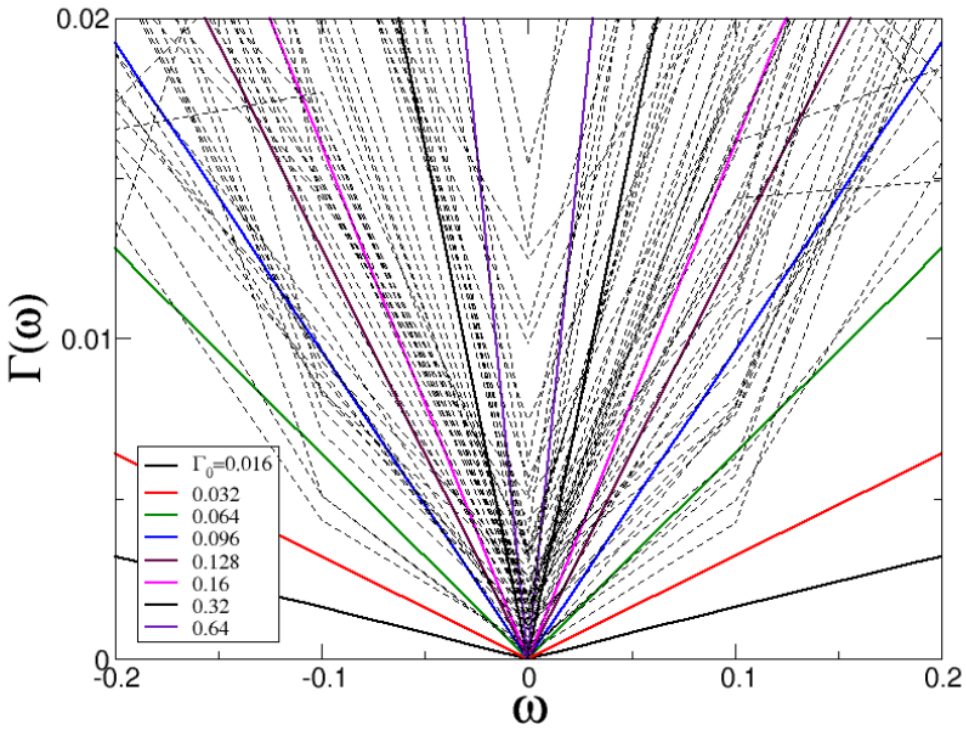

Figure 39: Hybridization functions obtained from different disorder realizations (dashed lines). Solid lines illustrates what would be the behavior for $\Gamma(\omega) = \Gamma_0|\omega|$ with varying Γ_0.

We are now in a position to apply the NRG method to study the disordered case. The Kondo temperature T_K or the crossing temperature T^* are obtained from the analysis of the NRG results for the magnetic susceptibility and ground state occupation $\langle n_0 \rangle$ as previously discussed in Sec. 3.4.

We first address the charge neutrality situation. Figure 40 shows the NRG results for the crossover temperature T^* and ground state occupation $\langle n_0 \rangle$ for ≈ 1000 realizations for $U = 0.5D$. The realization parameters are $\delta W = 0.32t$, $N_{\rm imp} = N_i/10$, $N_i = 40 \times 40$ and $\xi = 3a$. For practical purposes, we have stopped the NRG calculations at scales of the order $10^{-20}D$. This scale (dashed line) defines "zero temperature". We keep 1000 states in each NRG iteration and the parameter $\bar{\beta}$ is taken as $\bar{\beta} = 0.727$.

For a comparison with the "weak-disorder" toy model case, we also show results using $\Gamma(\omega) = \Gamma_0|\omega|$ with $\Gamma_0 = 0.064D$ (squares), $0.16D$ (circles) and $0.32D$ (triangles) (disorder here enters only through $\epsilon_0^{\rm dis}$). For each of the above values of Γ_0, a quantum phase transition is observed at values around $\epsilon_0^* \approx -0.01D$ (squares), $-0.025D$ (circles) and $-0.05D$ (triangles) separating empty-orbital ($\epsilon_0^{\rm dis} > \epsilon_0^*$) and local-moment ($\epsilon_0^{\rm dis} < \epsilon_0^*$) phases. The latter is characterized by vanishing T^* and $\langle n_0 \rangle \to 1$ while the former has

non-zero T^* and $\langle n_0 \rangle \to 0$. As the hybridization "strength" increases, the transition shifts to lower values of $\epsilon_0^{\rm dis}$ implying in the diminishment of the region of localized moments. The rise of a mixed valence regime with increasing Γ_0 is also consistent with results in the literature (see Fig. 7 in Ref. [38]).

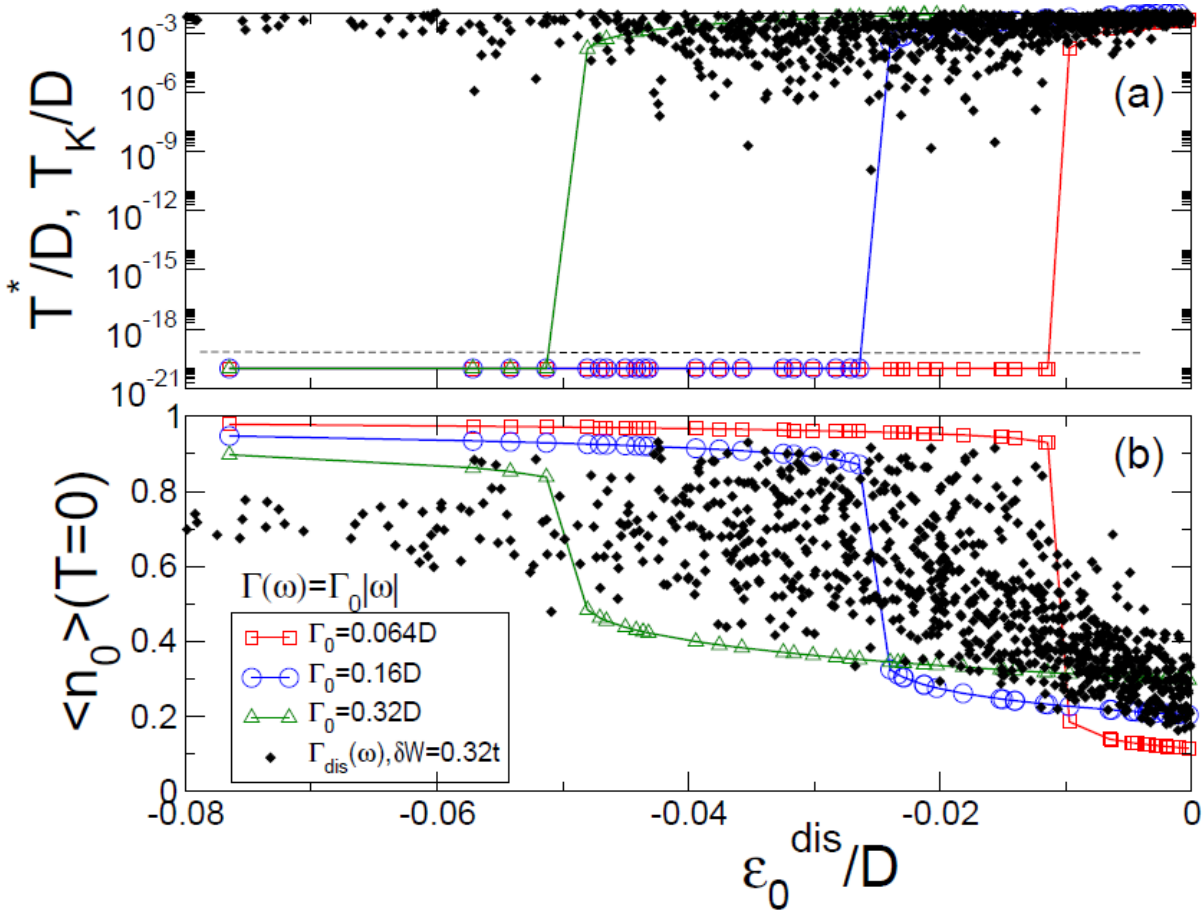

Figure 40: Crossover temperature T^* (a) and ground-state occupation $\langle n_0 \rangle$ (b) for different disorder realizations, each giving a different $\epsilon_0^{\rm dis}$. Solid lines: predictions of the weak disorder pseudogap model ($\Gamma(\omega) = \Gamma_0|\omega|$ with $\Gamma_0 = 0.064D$ (squares), $0.16D$ (circles) and $0.32D$ (triangles). The diamonds are outputs of the disordered situation.

The disordered case (filled diamonds) shows important differences: fluctuations in the disorder potential will lead to Kondo ground states, characterized by $\langle n_0 \rangle \to 0.8-1.0$ with a non-vanishing T^*, which, in this case, corresponds to the Kondo temperature T_K. Sharp features of pseudogap-related quantum phase transitions are no longer evident. Instead, as pointed above, the disorder induces a filling of the pseudogap (see Figs. 37 and 39) and leads to the formation of Kondo singlets which dominate the low temperature properties.

Disorder leads to a scenario where the vacancy state behaves as an Anderson impurity embedded in a "disordered metal" [88, 89, 90, 91], where different model parameters are realization-dependent. This is explored in Fig. 41, which shows distributions $P(T^*)$ (or

$P(T_K)$ in the Kondo regime) and ground state impurity occupation $P(\langle n_0 \rangle)$ for the same ≈ 1000 disorder realizations of Fig. 40 and different values of $\Delta\mu$.

The panels (e) and (f) of Fig. 41 confirm and clarify the conclusions drawn from Fig. 40. The distribution $P(T^*)$ displays two clear features: a sharp peak at larger values of T^* and a longer, log-distributed tail. As expected from the analysis of Fig. 40, the realizations contributing to the peak in $P(T^*)$ correspond to small values of $\langle n_0 \rangle$, related to the large number of points agglutinated close to $\epsilon_0^{\rm dis} > 0.02$ in Fig. 40, which gives rise to the "tail" in $P(\langle n_0 \rangle)$ (note that the histograms are built for log-distributed values) shown in Fig. 41f.

Figure 40 shows another interesting aspect, namely, the presence of intermediate values of the localized state occupation $\langle n_0 \rangle$, characteristic of a mixed valence phase, in a large region of the parameter space. For a pseudogaped system with $r = 1$ this regime is diminished in favor of the local moment phase [38, 67], so this is another indicator that disorder changes the pseudogap nature of the system into a "metallic" one.

In Ref. [90] the Kondo temperature distribution $P(T_K)$ obtained for metallic disordered system has a bimodal character. We do not observe such behavior in our simulations, however, the unimodal distributions we find are in accordance with those observed in Refs. [88, 91].

In order to make contact with the experimental situation described in Ref. [1], we explore the influence of a nonzero chemical potential on the T_K and $\langle n_0 \rangle$ distributions. We see that for large negative values of $\Delta\mu$ there is a predominance of positive values of $\delta\varepsilon$ which favor small occupations ($\langle n_0 \rangle \sim 0$). This is indeed the case already for $\Delta\mu = -0.05D$, as shown in Fig. 41b. This leads to relatively large crossover temperatures T^* into the empty-orbital regime (see Fig. 41a). As $\Delta\mu$ increases, this scenario changes qualitatively. Already at $\Delta\mu = -0.02D$, distinct "tails" in the distributions of $\langle n_0 \rangle$ and T^* can be seen (see, for instance, Figs. 41c-d), with $\langle n_0 \rangle \sim 0.8$ for some realizations.

For positive values of $\Delta\mu$, the disordered Kondo phase clearly dominates, characterized by $P(T_K)$ with long logarithmic tails along with a sharp peak in $P(\langle n_0 \rangle)$ around $\langle n_0 \rangle \sim 1$ (see Figs. 41g-j).

According to Ref. [80], the conversion of the gate potential V_g into μ for the Maryland experiment [1] leads to $|\mu| \leq 0.2$eV. Since our estimates leads to $D = 3t = 8.4$eV, this implies $\mu \simeq 0.025D$, showing that the values are in good correspondence with the experimental setup [1].

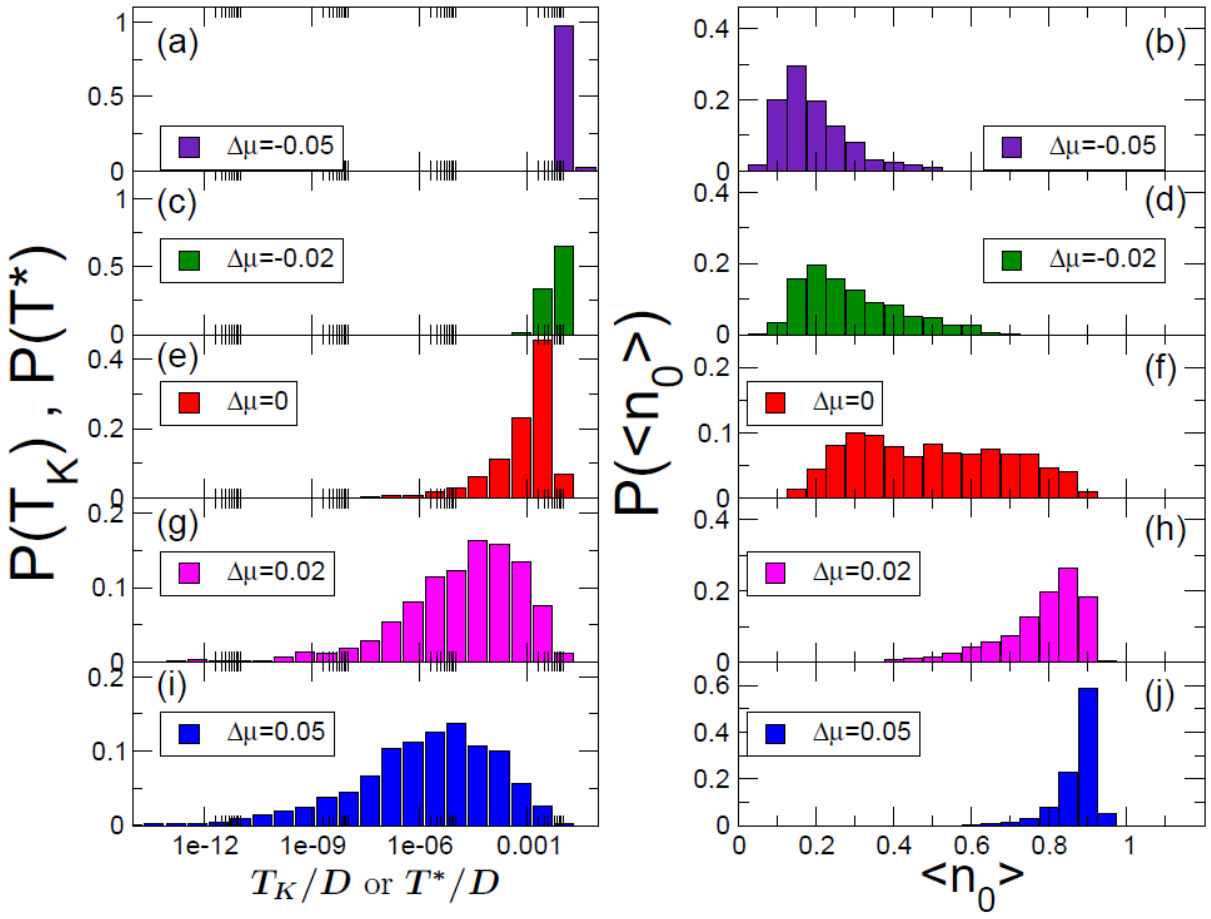

Figure 41: Normalized distributions for the crossover/Kondo temperature (left) and impurity occupation (right) for different values of the chemical potential $\Delta\mu$.

Typical values of T_K emerging from our data (see Fig. 41) are $T_K \sim 10^{-5}D - 10^{-3}D$ which means $T_K \sim 1K - 100K$. This is in good accordance with the range of temperature estimates found in Ref. [1].

Figure 42 summarizes the results of Fig. 41 presenting the distributions for the crossover/Kondo temperatures, Fig. 42a, and ground state occupation, Fig. 42b, distributions for different dopings in the same frame. The transition in these distributions as the system is filled, passing from the empty-orbital regime to the Kondo one, is clearly seen. The variable $y = \log(T_K[T^*]/D)$ is used for better visualization of the different curves in the same plot. We find that for negative values of $\Delta\mu$ the distributions follow a log-normal distribution. However, as the chemical potential is increased the distribution departs from this behavior and no longer retains its log-normal form. Instead, a long tail emerges on the low-T_K side. A similar behavior is shown in Fig. 1 of Ref. [88], although the transition observed there occurs due to direct varation of the disorder strength

whereas here it is due to a variation of the chemical potential.

A more careful analysis shows that, for small values of T_K, the Kondo temperature distributions follow a power-law behavior $P(T_K) \propto T_K^{(\alpha-1)}$ [88, 92]. The exponents α can be easily obtained through the distributions of $y = \log(T_K)$ whose probability distribution is given by $P(y = \log(T_K)) \propto T_K^{\alpha}$. The derivation of this result can be obtained through the use of a theorem from probability theory (see Appendix B).

In the inset of Fig. 42 we show that the estimates obtained from the $\log - \log$ plot of $y = \log(T_K)$ lead to $\alpha = 0.1 - 0.2$, depending weakly on $\Delta\mu$. Such behavior has been previously found in disordered Anderson systems [88, 89], where the interpretation for the divergent behavior of $P(T_K)$ for small T_K with non-universal exponents was given in terms of a Griffiths phase and disorder-induced non-Fermi-liquid behavior [92, 93, 94].

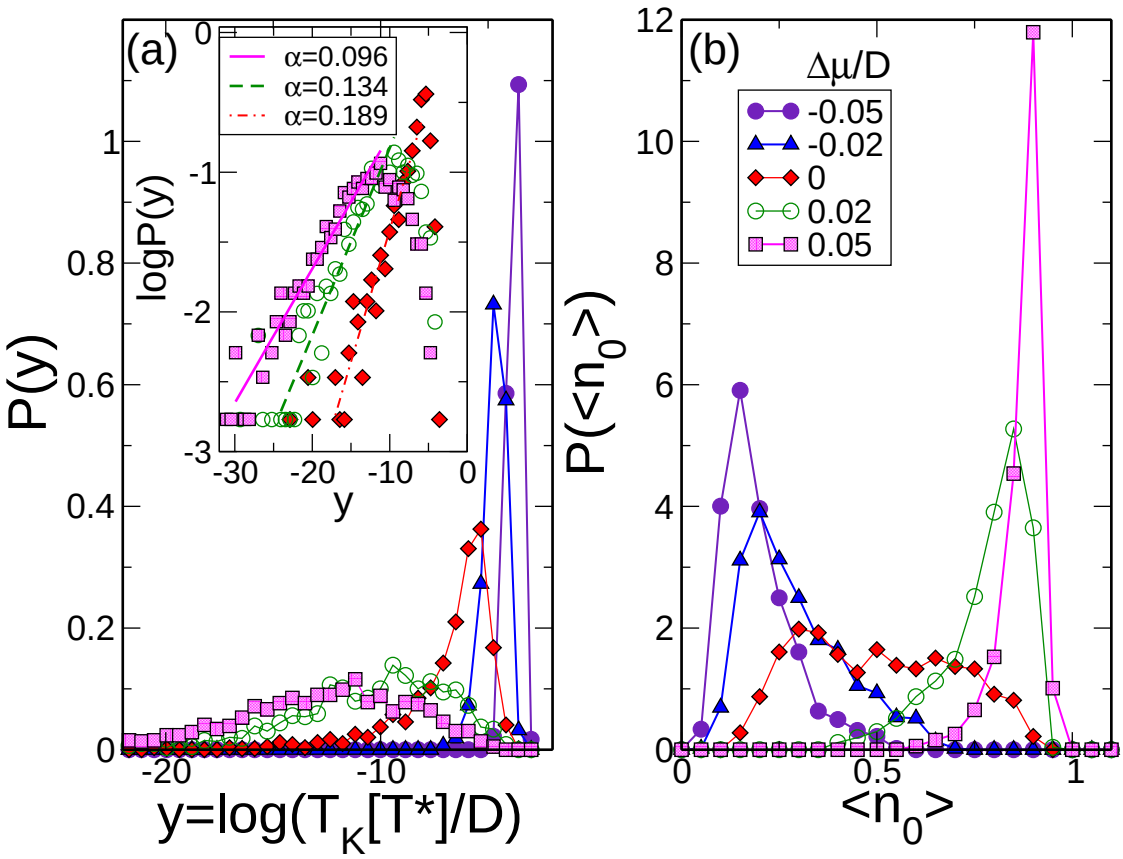

Figure 42: Normalized distributions for the crossover/Kondo temperature (left) and impurity occupation (right) for different values of the chemical potential $\Delta\mu$. Inset: Power-law behavior of the low T_K distributions, and corresponding exponent α, for varying $\Delta\mu$.

The exponent α is known to depend on the disorder strength and one expects $\alpha < 1$ and divergent behavior in $P(T_K)$ only for strong disorder [88, 89]. Interestingly, in Fig. 42, the disorder strength was kept fixed at the value $W = 0.32t$ and even then we obtained

$\alpha \sim 0.1 - 0.2$, with a weak dependency with $\Delta\mu$. We attribute these features as an enhancement of the disorder strength due to Kondo correlations. As the system enters deeper in the Kondo regime (increasing $\Delta\mu$), small fluctuations in the single-particle parameters produces large fluctuations in the Kondo scale [95]. Thus, the low-temperature properties are more strongly affected by the disorder potential, yielding a large effective disorder strength in the Kondo regime.

5 Conclusions

In this thesis we have addressed the problem of the Kondo effect generated by the presence of vacancies in a monolayer graphene sheet. We show that disorder plays a central role for the appearance of Kondo effect in graphene. To the best of our knowledge, this work is pioneering in presenting a systematic study of the Kondo effect in a disordered system with Dirac fermions.

We showed that long range disorder provides a natural coupling mechanism between the localized midgap state and the conduction band, opening the possibility of observing the Kondo effect due to π magnetism in graphene. This is in contrast with the existing works in the literature which only considered lattice reconstructions as a source of disorder and attributed σ magnetism as the responsible for the onset of Kondo physics. We find that the resulting distributions of Kondo temperatures $P(T_K)$ depends on the disorder strength and, in a more subtle manner, on the chemical potential.

Based on estimates of the ground state occupancy and the magnetic susceptibility, we observed that at charge neutrality the effect of disorder is to dress graphene with a metallic character and "spoil" the quantum critical behavior expected for pseudogaped systems. This result is in agreement with the metallic Kondo behavior namely, the single-parameter scaling observed in the experiments of Ref. [1] as discussed in Chapter 2.

Our modelling can also offer a conciliatory scenario between the experiments of Refs. [1] and [2]. Our findings suggest that sufficiently low disorder can imply in a very low value of T_K that may not be accessible through the experiments. This is a possible reason why the experiment conducted by Manchester's group [2] observes a Curie-like susceptibility since the samples they use appear to be cleaner than those used in the Maryland's experiment [1]. It should also be mentioned that the Manchester group measured the magnetic susceptibility whereas the Maryland group presents resistivity data. This is also an important aspect to consider since presence of any weakly-screened (i.e. low T_K) magnetic moments will dominate the results of susceptibility measurements. On the other hand,

electric resistivity receives contributions from strongly screened (i.e. high T_K) moments and hence measurement of transport data are more likely to display Kondo screening traces.

We have also explored the effect of doping for the Kondo effect in graphene. In order to be in close contact to the experimental environment, we adopt doping levels consistent to those used in Ref. [1]. According to Ref. [80], the mapping of V_g into μ for this experiment leads to $|\mu| \leq 0.2$eV ($\simeq 0.025D$ for $D \approx 8$eV, the value we use). As expected for metallic systems, a negative doping tends to favor the empty orbital regime, consistent with the probability distributions of $\langle n_0 \rangle$ and T^* we find. The Kondo screening scenario is recovered as the doping is increased. This situation contrasts with the experimental results [1] which display a nearly particle-hole symmetric behavior of T_K. However, the T_K estimates we obtain are $T_K \sim 10^{-5}D - 10^{-3}D$ which means $T_K \sim 1K - 100K$, this is in good agreement with the experiment [1]. Our results show that increasing disorder leads to an increase in the width of $P(T_K)$. Then, for sufficiently low disorder strength, narrow distributions should rise opening the possibility for an approximately single-parameter scaling regime to hold and support the behavior observed in Ref. [1].

An important outcome of our study is the observation of long tails in the distribution of $P(T_K)$ and as μ is increased, the occurrence of power-law divergence at low $T_K \to 0$. This is consistent with the presence of a Griffiths phase. Unlike the metallic situation, where this phenomenon is observed trough a variation of the disorder strength [88], we observe the onset of Griffiths phase due to doping variation while the disorder strength remains fixed.

Our results suggest interesting routes for experiments. First, by gradually introducing disorder to the graphene sheet it may be verified the transition from the local moment scenario to a screened one. This may be tested for instance by exploring Kondo effect in graphene deposited in different substrates such as SiO_2 and BN, as disorder effects are expected to be very different in these composites. The second interesting route is the exploration of non-Fermi-liquid behavior in transport experiments or measurements of thermodynamics quantities in graphene sheets by varying the doping in graphene disordered samples.

A straightforward extension of our work is to calculate transport properties via the NRG method. Also, a systematic variation of the disorder parameters and observation of how this affects the distributions of $P(T_K)$ and $P(\langle n_0 \rangle)$ is also one of our tasks for a future work. Another interesting possibility is try to perform more realistic calculations

treating the case of several vacancies. The study of the contribution of σ magnetism in the disordered context is also an interesting issue still not addressed in the literature.

The long range disorder model with vacancies discussed in this thesis can also be explored to model the spin relaxation in diffusive graphene samples. There is experimental evidence [96] that vacancies and local magnetic moments play an important role in the fast spin relaxation rate observed experimentally [97] which is orders of magnitude smaller than theoretical predictions [98]. Our model of charge puddles offers a possible solution for the puzzle of spin relaxation times in graphene. Local fluctuations of the chemical potential enhance the transition rates at the charge neutrality point, dramatically suppressing the charge relaxation times. This study is in course, but it is not included in this thesis.

APPENDIX A – The Schrieffer-Wolff transformation: Anderson meets Kondo

In Sec. 3.1 we saw how one can determine a range of values for U and $\gamma_{\mathbf{k}d}$ required for a crossover between magnetic and nonmagnetic limits and hence establish why, in empirical observations, some transition elements with partially-filled d-shells remain magnetic when diluted in some but not all host metals.

In the magnetic case, the impurity state is singly occupied with a two-fold degeneracy corresponding to spin 1/2. By assuming that such configuration is the ground state, the empty and doubly occupied cases will be higher excited states. With the additional condition that $\gamma_{\mathbf{k}d}$ is small compared to ϵ_d and U, charge fluctuations in the impurity will be small. This observation suggests that such fluctuations might be eliminated altogether. This procedure is achieved by a canonical transformation developed by Schrieffer and Wolff [99], which replaces the charge fluctuations by an effective interaction between the spins of the conduction band and the impurity. As we will see, the transformation is equivalent to a diagonalization of the Anderson Hamiltonian in the subspace of the singly occupied impurity states.

The first step to develop the transformation is to separate the Anderson Hamiltonian into a zeroth-order part:

$$H_0 = \sum_{\mathbf{k},\sigma} \epsilon_{\mathbf{k}} c^{\dagger}_{\mathbf{k}\sigma} c_{\mathbf{k}\sigma} + \sum_{\sigma} \epsilon_d c^{\dagger}_{d\sigma} c_{d\sigma} + \sum_{\mathbf{k},\sigma} + U n_{d\uparrow} n_{d\downarrow} \tag{A.1}$$

and a "perturbation",

$$H_1 = \sum_{\mathbf{k},\sigma} \gamma_{\mathbf{k}d} (c^{\dagger}_{\mathbf{k}\sigma} c_{d\sigma} + c^{\dagger}_{d\sigma} c_{\mathbf{k}\sigma}) \tag{A.2}$$

The similarity transformation applied to the Hamiltonian $H_A = H_0 + H_1$ reads:

$$\begin{aligned}\tilde{H} &= e^S H_A e^{-S} \\ &= H_A + [S, H_A] + \frac{1}{2}[S[S, H_A]] + \dots \\ &= H_0 + H_1 + [S, H_0] + [S, H_1] + \frac{1}{2}[S, [S, H_0]] + \frac{1}{2}[S, [S, H_1]] + \dots, \end{aligned} \tag{A.3}$$

where S is a similarity matrix chosen to eliminate the coupling between conduction band and impurity states to leading order in $\gamma_{\mathbf{k}d}$. According to Eq. (A.3), this is accomplished through the condition:

$$[S, H_0] + H_1 = 0. \tag{A.4}$$

Insertion of Eq. (A.4) into Eq. (A.3) results

$$\begin{aligned}\tilde{H} &= H_0 + [S, H_1] + \frac{1}{2}[S, -H_1] + \frac{1}{2}[S, [S, H_1]] + \dots \\ &\approx H_0 + \frac{1}{2}[S, H_1]. \end{aligned} \tag{A.5}$$

The second step is the construction of the similarity matrix S. Through the observation that $[S, H_0] = -H_1$, one concludes that S must contain terms $\propto c^\dagger_{\mathbf{k}\sigma} c_{d\sigma}$. Furthermore, as the commutator of $c^\dagger_{\mathbf{k}\sigma} c_{d\sigma}$ with $U n_{d\uparrow} n_{d\downarrow}$ is proportional to $n_{d-\sigma} c^\dagger_{\mathbf{k}\sigma} c_{d\sigma}$, a nice try is the assumption that the transformation takes the form

$$S = \sum_{\mathbf{k},\sigma} \left(A_{\mathbf{k}} + B_{\mathbf{k}} n_{d-\sigma}\right) c^\dagger_{\mathbf{k}\sigma} c_{d\sigma} - H.c. \tag{A.6}$$

The condition that S is antihermitian relies on the fact that e^S is an unitary transformation.

After some algebra one obtains [6]:

$$[H_0, S] = \sum_{\mathbf{k},\sigma} \left[\left(\epsilon_{\mathbf{k}} - \epsilon_d\right) A_{\mathbf{k}} + \left(\epsilon_{\mathbf{k}} - \epsilon_d - U\right) n_{d-\sigma} B_{\mathbf{k}} - U n_{d-\sigma} A_{\mathbf{k}}\right] c^\dagger_{\mathbf{k}\sigma} c_{d\sigma} + H.c. \tag{A.7}$$

To satisfy Eq. (A.7) it is required that [6]

$$A_{\mathbf{k}} = \frac{\gamma_{\mathbf{k}d}}{\epsilon_{\mathbf{k}} - \epsilon_d} \quad \text{and} \quad B_{\mathbf{k}} = \gamma_{\mathbf{k}d}\left[\frac{1}{\epsilon_{\mathbf{k}} - (\epsilon_d + U)} - \frac{1}{\epsilon_{\mathbf{k}} - \epsilon_d}\right]. \tag{A.8}$$

Inserting the results of Eq. (A.8) back into Eq. (A.6) defines the Schrieffer-Wolff transformation.

The last step of the transformation is the calculation of the commutator $[S, H_1]$ aiming at finding the expression of $\tilde{H}$.

We adopt the simplified notation $\rho_{\mathbf{k}d\sigma} = c^{\dagger}_{\mathbf{k}\sigma} c_{d\sigma}$ and write the commutator as

$$\begin{aligned}
\frac{1}{2}[S, H_1] &= \frac{1}{2} \sum_{\mathbf{k},\mathbf{k}'\sigma,\sigma'} \Big\{ A_{\mathbf{k}} \gamma_{\mathbf{k}'d} \left[\rho_{\mathbf{k}d\sigma}, \rho_{\mathbf{k}'d\sigma'}\right] + A_{\mathbf{k}} \gamma^{*}_{\mathbf{k}'d} \left[\rho_{\mathbf{k}d\sigma}, \rho^{\dagger}_{\mathbf{k}'d\sigma'}\right] + B_{\mathbf{k}} \gamma_{\mathbf{k}'d} \left[n_{d-\sigma} \rho_{\mathbf{k}d\sigma}, \rho_{\mathbf{k}'d\sigma'}\right] \\
&+ B_{\mathbf{k}} \gamma^{*}_{\mathbf{k}'d} \left[n_{d-\sigma} \rho_{\mathbf{k}d\sigma}, \rho^{\dagger}_{\mathbf{k}'d\sigma'}\right] - A^{*}_{\mathbf{k}} \gamma_{\mathbf{k}'d} \left[\rho^{\dagger}_{\mathbf{k}d\sigma}, \rho_{\mathbf{k}'d\sigma'}\right] - A^{*}_{\mathbf{k}} \gamma^{*}_{\mathbf{k}'d} \left[\rho^{\dagger}_{\mathbf{k}d\sigma}, \rho^{\dagger}_{\mathbf{k}'d\sigma'}\right] \\
&- B^{*}_{\mathbf{k}} \gamma_{\mathbf{k}'d} \left[n_{d-\sigma} \rho^{\dagger}_{\mathbf{k}d\sigma}, \rho_{\mathbf{k}'d\sigma'}\right] - B^{*}_{\mathbf{k}} \gamma^{*}_{\mathbf{k}'d} \left[n_{d-\sigma} \rho^{\dagger}_{\mathbf{k}d\sigma}, \rho^{\dagger}_{\mathbf{k}'d\sigma'}\right] \Big\} . \qquad \text{(A.9)}
\end{aligned}$$

Performing the algebra of commutators and anti-commutators of the terms Eq. (A.9) we write:

$$\begin{aligned}
\frac{1}{2}[S, H_1] &= \frac{1}{2} \Bigg\{ \sum_{\mathbf{k},\sigma} \left[\left(A_{\mathbf{k}} + B_{\mathbf{k}} n_{d-\sigma}\right) \gamma^{*}_{\mathbf{k}d} n_{d\sigma} + H.c \right] + \sum_{\mathbf{k},\mathbf{k}',\sigma} \left[A_{\mathbf{k}} \gamma^{*}_{\mathbf{k}'d} c^{\dagger}_{\mathbf{k}\sigma} c_{\mathbf{k}'\sigma} + H.c \right] \\
&- \sum_{\mathbf{k},\mathbf{k}',\sigma} \left[B_{\mathbf{k}} \gamma_{\mathbf{k}'d} \rho_{\mathbf{k}d\sigma} \rho_{\mathbf{k}'d-\sigma} + H.c \right] + \sum_{\mathbf{k},\mathbf{k}',\sigma} \left[B_{\mathbf{k}} \gamma^{*}_{\mathbf{k}'d} \left(n_{d-\sigma} c^{\dagger}_{\mathbf{k}\sigma} c_{\mathbf{k}'\sigma} + \rho_{\mathbf{k}d\sigma} \rho_{\mathbf{k}'d-\sigma} \right) \right. \\
&+ \left. H.c \right] \Bigg\} \qquad \text{(A.10)}
\end{aligned}$$

The terms in Eq. (A.10) can still be arranged in a more enlightening format, to wit,

$$\frac{1}{2}[S, H_1] = H_{exchange} + H_{band} + H_{single} + H_{double}, \qquad \text{(A.11)}$$

where

$$H_{exchange} = -\sum_{\mathbf{k},\mathbf{k}'} \frac{J_{\mathbf{k}\mathbf{k}'}}{\hbar^2} \left(\sum_{\sigma,\sigma'} c^{\dagger}_{\mathbf{k}\sigma} \mathbf{S}_{\sigma\sigma'} c_{\mathbf{k}'\sigma'} \right) \cdot \left(\sum_{\sigma'',\sigma'''} c^{\dagger}_{d\sigma''} \mathbf{S}_{\sigma''\sigma'''} c_{d\sigma'''} \right), \qquad \text{(A.12)}$$

$$H_{band} = \sum_{\mathbf{k},\mathbf{k}'} \left[w_{\mathbf{k}\mathbf{k}'} + \frac{1}{4} J_{\mathbf{k}\mathbf{k}'} \left(n_{d\uparrow} + n_{d\downarrow} \right) \right] \sum_{\sigma} c^{\dagger}_{\mathbf{k}\sigma} c_{\mathbf{k}'\sigma}, \qquad \text{(A.13)}$$

$$H_{single} = -\sum_{\mathbf{k},\sigma} \left[w_{\mathbf{k}\mathbf{k}} + \frac{1}{2} J_{\mathbf{k}\mathbf{k}} n_{d-\sigma} \right] n_{d\sigma}, \qquad \text{(A.14)}$$

$$H_{double} = -\frac{1}{2} \sum_{\mathbf{k},\mathbf{k}',\sigma} \left[B_{\mathbf{k}} \gamma_{\mathbf{k}'d} c^{\dagger}_{\mathbf{k}'-\sigma} c^{\dagger}_{\mathbf{k}\sigma} c_{d\sigma} c_{d-\sigma} + H.c \right]. \qquad \text{(A.15)}$$

In the above expressions, the spin "vector" reads $\mathbf{S} = (\hbar/2)\boldsymbol{\sigma}$, where $\boldsymbol{\sigma} = (\sigma_x, \sigma_y, \sigma_z)$

and $\sigma_{x,y,z}$ are the Pauli matrices. Also $w_{\mathbf{k}\mathbf{k}'}$ and $J_{\mathbf{k}\mathbf{k}'}$ are given by [6]

$$w_{\mathbf{k}\mathbf{k}'} = \frac{\gamma_{\mathbf{k}d}\gamma^*_{\mathbf{k}'d}}{2}\left[\frac{1}{\epsilon_{\mathbf{k}} - \epsilon_d} + \frac{1}{\epsilon_{\mathbf{k}'} - \epsilon_d}\right] \tag{A.16}$$

$$J_{\mathbf{k}\mathbf{k}'} = \gamma_{\mathbf{k}d}\gamma^*_{\mathbf{k}'d}\left[\frac{1}{\epsilon_{\mathbf{k}} - (\epsilon_d + U)} - \frac{1}{\epsilon_{\mathbf{k}} - \epsilon_d} + \frac{1}{\epsilon_{\mathbf{k}'} - (\epsilon_d + U)} - \frac{1}{\epsilon_{\mathbf{k}'} - \epsilon_d}\right]. \tag{A.17}$$

In the regime of single occupancy of the localized state, we see that the term H_{double} can be neglected since it changes the occupancy of the impurity by two, hence, it does not connect the part of the Hilbert space having one d electron (the case of interest) with the remainder of the Hilbert space, i.e., 0 or 2 d electrons [99].

As $n_{d\uparrow} + n_{d\downarrow} = 1$, H_{band} reduces to a one-body potential which can be eliminated by a transformation of the $\mathbf{k}$ states to a set of one-electron conduction states which include this direct scattering term. The resulting shift in the conduction states energies may be incorporated in H_0.

The term H_{single} renormalizes the energy of the localized state:

$$\epsilon_d \to \tilde{\epsilon_d} = \epsilon_d - \sum_{\mathbf{k}} w_{\mathbf{k}\mathbf{k}}. \tag{A.18}$$

The only important term to be retained for the Kondo physics is the exchange Hamiltonian Eq. (A.12), reducing the transformed Hamiltonian to

$$\tilde{H} = H_0 + H_{exchange}, \tag{A.19}$$

which may be explicitly written as

$$\begin{aligned}\tilde{H} &= \sum_{\mathbf{k},\sigma} \epsilon_{\mathbf{k}} c^\dagger_{\mathbf{k}\sigma} c_{\mathbf{k}\sigma} - \sum_{\mathbf{k},\mathbf{k}'} \frac{J_{\mathbf{k}\mathbf{k}'}}{\hbar^2}\left(\sum_{\sigma,\sigma'} c^\dagger_{\mathbf{k}\sigma}\mathbf{S}_{\sigma\sigma'}c_{\mathbf{k}'\sigma'}\right)\cdot\left(\sum_{\sigma'',\sigma'''} c^\dagger_{d\sigma''}\mathbf{S}_{\sigma''\sigma'''}c_{d\sigma'''}\right) \\ &= \sum_{\mathbf{k},\sigma} \epsilon_{\mathbf{k}} c^\dagger_{\mathbf{k}\sigma} c_{\mathbf{k}\sigma} - \sum_{\mathbf{k},\mathbf{k}'} \frac{J_{\mathbf{k}\mathbf{k}'}}{\hbar^2}\mathbf{s}\cdot\mathbf{S}.\end{aligned} \tag{A.20}$$

We used the fact that the impurity terms in H_0 will only shift the system energy in the impurity single occupation limit to drop the ϵ_d and U terms. In the interacting term, $\mathbf{s}$ denotes the conduction electron spins and $\mathbf{S}$ the impurity spin. The interacting part in Hamiltonian Eq. (A.20) is denoted as the Kondo Hamiltonian (also known as s-d model)[8].

One aspect of major importance about the exchange coupling is that it is negative.

This assertion is proved by setting $\epsilon_{\mathbf{k}} = \epsilon_{\mathbf{k}'} = \epsilon_F$ in Eq. (A.17), resulting [6]

$$J_{\mathbf{k}_F\mathbf{k}_F} = -2\left(\frac{U}{|\epsilon_d|\,(U - |\epsilon_d|)}\right) < 0. \tag{A.21}$$

This result entails an antiferromagnetic coupling between the band electrons and the impurity one. The character of this interaction is responsible for the formation of a singlet state at the d-impurity below the Kondo temperature T_K.

APPENDIX B – Derivation of the $P(y = \log(T_K))$ *distribution*

In order to derive the distribution of $y = \log(T_K)$, it is useful to make use of the following theorem from probability theory [100]:

Theorem 1 *Let X be a continuous random variable with probability density $f(x)$, where $f(x) > 0$ for $a < x < b$. Suppose that $y = H(x)$ is a strictly monotone (increasing or decreasing) function of x. Assume that this function is differentiable (and hence continuous) for all x. Then the random variable Y defined as $Y = H(X)$ has a probability density function g given by:*

$$g(y) = f(x)\left|\frac{dx}{dy}\right|, \tag{B.1}$$

where x is expressed in terms of y.

For our case, identifying $X = e^Y = T_K$ we have $dx/dy = e^y = T_K$, hence, making use of the Theorem 1:

$$P(y = \log(T_K)) \propto T_K^{\alpha-1} T_K \propto T_K^{\alpha}. \tag{B.2}$$

References

[1] Jian-Hao Chen, Liang Li, William G Cullen, Ellen D Williams, and Michael S Fuhrer. Tunable Kondo effect in graphene with defects. *Nature Phys.*, 7:535, 2011.

[2] R R Nair, I-L Tsai, M Sepioni, O Lehtinen, J Keinonen, a V Krasheninnikov, a H Castro Neto, M I Katsnelson, a K Geim, and I V Grigorieva. Dual origin of defect magnetism in graphene and its reversible switching by molecular doping. *Nature communications*, 4(May):2010, January 2013.

[3] A. H. Castro Neto, F. Guinea, N. M. R. Peres, K. S. Novoselov, and A. K. Geim. The electronic properties of graphene. *Rev. Mod. Phys.*, 81:109–162, Jan 2009.

[4] Vitor M. Pereira, J M B Lopes dos Santos, and A H Castro Neto. Modeling disorder in graphene. *Phys. Rev. B*, 77:115109, 2008.

[5] Eva Y Andrei, Guohong Li, and Xu Du. Electronic properties of graphene: a perspective from scanning tunneling microscopy and magnetotransport. *Reports on progress in physics. Physical Society (Great Britain)*, 75(5):056501, May 2012.

[6] Philip Phillips. *Advanced Solid State Physics*. Westview Press, 1st edition, 2003.

[7] M. P. Sarachik, E. Corenzwit, and L. D. Longinotti. Resistivity of mo-nb and mo-re alloys containing 1% fe. *Phys. Rev.*, 135:A1041–A1045, Aug 1964.

[8] A. C. Hewson. *The Kondo Problem to Heavy Fermions*. Cambridge University Press, 1st edition, 1993.

[9] Ralf Bulla, Theo A. Costi, and Thomas Pruschke. Numerical renormalization group method for quantum impurity systems. *Rev. Mod. Phys.*, 80:395–450, Apr 2008.

[10] H. R. Krishna-murthy, J. W. Wilkins, and K. G. Wilson. Renormalization-group approach to the anderson model of dilute magnetic alloys. i. static properties for the symmetric case. *Phys. Rev. B*, 21:1003–1043, Feb 1980.

[11] Matthias Vojta, Lars Fritz, and Ralf Bulla. Gate-controlled Kondo screening in graphene: Quantum criticality and electron-hole asymmetry. *EPL (Europhysics Letters)*, 90:27006, 2010.

[12] A. A. El-Barbary, R. H. Telling, C. P. Ewels, M. I. Heggie, and P. R. Briddon. Structure and energetics of the vacancy in graphite. *Phys. Rev. B*, 68:144107, Oct 2003.

[13] K. S. Novoselov, A. K. Geim, S. V. Morozov, D. Jiang, Y. Zhang, S. V. Dubonos, I. V. Grigorieva, and A. A. Firsov. Electric field effect in atomically thin carbon films. *Science*, 306(5696):666–669, 2004.

[14] A. K. Geim and K. S. Novoselov. The rise of graphene. *Nature Materials*, 6(3):183–191, March 2007.

[15] A. K. Geim. Graphene: Status and prospects. *Science*, 324(5934):1530–1534, 2009.

[16] E. R. Mucciolo and C H Lewenkopf. Disorder and electronic transport in graphene. *J. Phys.: Cond. Mat.*, 22:273201, 2010.

[17] Valeri N. Kotov, Bruno Uchoa, Vitor M. Pereira, F. Guinea, and A. H. Castro Neto. Electron-electron interactions in graphene: Current status and perspectives. *Rev. Mod. Phys.*, 84:1067–1125, Jul 2012.

[18] S. Das Sarma, Shaffique Adam, E. H. Hwang, and Enrico Rossi. Electronic transport in two-dimensional graphene. *Rev. Mod. Phys.*, 83:407–470, May 2011.

[19] D. R. Cooper, B. D'Anjou, N. Ghattamaneni, and et al. Experimental review of graphene. *ISRN Condensed Matter Physics*, 2012:501686, 2012.

[20] N. M. R. Peres. colloquium: The transport properties of graphene: An introduction. *Rev. Mod. Phys.*, 82:2673–2700, Sep 2010.

[21] Antonio H Castro Neto. Les Houches Notes on Graphene. 2010.

[22] C. W. J. Beenakker. colloquium: Andreev reflection and klein tunneling in graphene. *Rev. Mod. Phys.*, 80:1337–1354, Oct 2008.

[23] K. S. Novoselov, V. I. Fal[prime]ko, L. Colombo, P. R. Gellert, M. G. Schwab, and K. Kim. A roadmap for graphene. *Nature*, 490(7419):192–200, October 2012.

[24] Edward McCann and Mikito Koshino. The electronic properties of bilayer graphene. *Reports on progress in physics. Physical Society (Great Britain)*, 76(5):056503, May 2013.

[25] Mikhail I. Katsnelson. *Graphene Carbon in two dimentions*. Cambridge University Press, 1st edition, 2012.

[26] E. Kaxiras. *Atomic and Eletronic Structure of Solids*. Cambridge University Press, 1st edition, 2003.

[27] R. Saito, G. Dresselhaus, and M. S. Dresselhaus. *Properties of carbon nanotubes*. Imperial College Press, 1st edition, 1998.

[28] N. W. Ashcroft and N. D. Mermin. *Solid state physics*. Harcourt College Publishers, 1st edition, 1976.

[29] P. R. Wallace. The band theory of graphite. *Phys. Rev.*, 71:622–634, May 1947.

[30] K. S. Novoselov, A. K. Geim, S. V. Morozov, D. Jiang, M. I. Katsnelson, I. V. Grigorieva, S. V. Dubonos, and A. A. Firsov. Two-Dimensional Gas of Massless Dirac Fermions in Graphene. *Nature*, September 2005.

[31] Yuanbo Zhang, Yan-Wen Tan, Horst L. Stormer, and Philip Kim. Experimental Observation of Quantum Hall Effect and Berry's Phase in Graphene. *Nature*, 438(7065):201–204, September 2005.

[32] K. S. Novoselov, Z. Jiang, Y. Zhang, S. V. Morozov, H. L. Stormer, U. Zeitler, J. C. Maan, G. S. Boebinger, P. Kim, and A. K. Geim. Room-Temperature Quantum Hall Effect in Graphene. *Science*, 315(5817):1379, March 2007.

[33] D. J. Goldhaber-Gordon. *The Kondo effect in a single-electron transistor*. PhD Thesis, 1998.

[34] P. W. Anderson. Localized magnetic states in metals. *Phys. Rev.*, 124:41–53, Oct 1961.

[35] J. Kondo. Resistance minimum in dilute magnetic alloys. *Progress of Theoretical Physics*, 32:37–49, July 1964.

[36] Kenneth G. Wilson. The renormalization group: Critical phenomena and the kondo problem. *Rev. Mod. Phys.*, 47:773–840, Oct 1975.

[37] D Withoff and E Fradkin. Phase-Transitions in Gapless Fermi Systems with Magnetic Impurities. *Phys. Rev. Lett.*, 64(15):1835–1838, 1990.

[38] Carlos Gonzalez-Buxton and Kevin Ingersent. Renormalization-group study of Anderson and Kondo impurities in gapless Fermi systems. *Phys. Rev. B*, 57(22):14254–14293, 1998.

[39] Lars Fritz and Matthias Vojta. The Physics of Kondo Impurities in Graphene. *Reports on Progress in Physics*, 76(3), 2013.

[40] Bruno Uchoa, Valeri N. Kotov, N. M. R. Peres, and A. H. Castro Neto. Localized magnetic states in graphene. *Phys. Rev. Lett.*, 101:026805, Jul 2008.

[41] Bruno Uchoa, T. G. Rappoport, and A. H. Castro Neto. Kondo quantum criticality of magnetic adatoms in graphene. *Phys. Rev. Lett.*, 106:016801, Jan 2011.

[42] K. Sengupta and G. Baskaran. Tuning kondo physics in graphene with gate voltage. *Phys. Rev. B*, 77:045417, Jan 2008.

[43] Martina Hentschel and Francisco Guinea. Orthogonality catastrophe and kondo effect in graphene. *Phys. Rev. B*, 76:115407, Sep 2007.

[44] P S Cornaglia, Gonzalo Usaj, and C A Balseiro. Localized Spins on Graphene. *Phys. Rev. Lett.*, 102(4):46801, January 2009.

[45] J. O. Sofo, Gonzalo Usaj, P. S. Cornaglia, A. M. Suarez, A. D. Hernández-Nieves, and C. A. Balseiro. Magnetic structure of hydrogen-induced defects on graphene. *Phys. Rev. B*, 85:115405, Mar 2012.

[46] Maxim Kharitonov and Gabriel Kotliar. Kondo effect in monolayer and bilayer graphene: Physical realizations of the multichannel kondo models. *Phys. Rev. B*, 88:201103, Nov 2013.

[47] H. C. Manoharan, C. P. Lutz, and D. M. Eigler. Quantum mirages formed by coherent projection of electronic structure. *Nature*, 403(6769):512–515, February 2000.

[48] Victor W Brar, Régis Decker, Hans-michael Solowan, Yang Wang, Lorenzo Maserati, Kevin T Chan, Hoonkyung Lee, O Girit, Alex Zettl, Steven G Louie, Marvin L Cohen, and Michael F Crommie. Gate-controlled ionization and screening of cobalt adatoms on a graphene surface. *Nature Phys.*, 7(October 2010):43–47, 2011.

[49] Oleg V Yazyev. Emergence of magnetism in graphene materials and nanostructures. *Reports on Progress in Physics*, 73(5):056501, May 2010.

[50] Oleg V. Yazyev and Lothar Helm. Defect-induced magnetism in graphene. *Phys. Rev. B*, 75:125408, Mar 2007.

[51] B R K Nanda, M Sherafati, Z S Popović, and S Satpathy. Electronic structure of the substitutional vacancy in graphene: density-functional and Green's function studies. *New J. Phys.*, 14(8):083004, August 2012.

[52] J. J. Palacios and F. Ynduráin. Critical analysis of vacancy-induced magnetism in monolayer and bilayer graphene. *Phys. Rev. B*, 85:245443, Jun 2012.

[53] R R Nair, M Sepioni, I-Ling Tsai, O Lehtinen, J Keinonen, A V Krasheninnikov, T Thomson, A K Geim, and I V Grigorieva. Spin-half paramagnetism in graphene induced by point defects. *Nature Phys.*, 8(March):199–202, 2012.

[54] Kathleen M. McCreary, Adrian G. Swartz, Wei Han, Jaroslav Fabian, and Roland K. Kawakami. Magnetic Moment Formation in Graphene Detected by Scattering of Pure Spin Currents. *Phys. Rev. Lett.*, 109(18):186604, November 2012.

[55] H. R. Krishna-murthy, J. W. Wilkins, and K. G. Wilson. Renormalization-group approach to the anderson model of dilute magnetic alloys. ii. static properties for the asymmetric case. *Phys. Rev. B*, 21:1044–1083, Feb 1980.

[56] Jian-Hao Chen, W G Cullen, C Jang, M S Fuhrer, and E D Williams. Defect Scattering in Graphene. *Phys. Rev. Lett.*, 102:236805, 2009.

[57] P Nozières. A " Fermi-Liquid " Description of the Kondo Problem at Low Temperatures. *J. Low. Temp Phys.*, 17:31–42, 1974.

[58] T A Costi, A C Hewson, and V Zlatic. Transport coefficients of the Anderson model via the numerical renormalization group. *J. Phys. Condens. Matter*, 6:2519–2518, 1994.

[59] Johannes Jobst and Heiko B. Weber. Origin of logarithmic resistance correction in graphene. *Nature Physics*, 8(5):352–352, May 2012.

[60] Johannes Jobst, Daniel Waldmann, Igor V. Gornyi, Alexander D. Mirlin, and Heiko B. Weber. Electron-Electron Interaction in the Magnetoresistance of Graphene. *Physical Review Letters*, 108(10):106601, March 2012.

[61] Jian-Hao Chen, Liang Li, William G Cullen, Ellen D Williams, and Michael S Fuhrer. Reply: Origin of logarithmic resistance correction in graphene. *Nature Physics*, 8(5):353–353, May 2012.

[62] P. Fulde. *Electron correlations in molecules and solids.* Springer, 3rd edition, 1995.

[63] F. D. M. Haldane. Scaling theory of the asymmetric anderson model. *Phys. Rev. Lett.*, 40:416–419, Feb 1978.

[64] P. W. Anderson. A poor man ' s derivation of scaling laws for the Kondo problem. *J. Phys. C*, 3:2436, 1970.

[65] Carlos R. Cassanello and Eduardo Fradkin. Kondo effect in flux phases. *Phys. Rev. B*, 53:15079–15094, Jun 1996.

[66] Lech S. Borkowski and P. J. Hirschfeld. Kondo effect in gapless superconductors. *Phys. Rev. B*, 46:9274–9277, Oct 1992.

[67] Carlos Gonzalez-Buxton and Kevin Ingersent. Stabilization of local moments in gapless fermi systems. *Phys. Rev. B*, 54:R15614–R15617, Dec 1996.

[68] Kevin Ingersent. Behavior of magnetic impurities in gapless fermi systems. *Phys. Rev. B*, 54:11936–11939, Nov 1996.

[69] Wanda C. Oliveira and Luiz N. Oliveira. Generalized numerical renormalization-group method to calculate the thermodynamical properties of impurities in metals. *Phys. Rev. B*, 49:11986–11994, May 1994.

[70] M. Yoshida, M. A. Whitaker, and L. N. Oliveira. Renormalization-group calculation of excitation properties for impurity models. *Phys. Rev. B*, 41:9403–9414, May 1990.

[71] H. O. Frota and L. N. Oliveira. Photoemission spectroscopy for the spin-degenerate anderson model. *Phys. Rev. B*, 33:7871–7874, Jun 1986.

[72] Th. Pruschke R. Bulla and A. C. Hewson. Anderson impurity in pseudo-gap Fermi systems. *J. Phys. Condens. Matter*, 9:10463, 1997.

[73] M. M. Ugeda, I. Brihuega, F. Guinea, and J. M. Gómez-Rodríguez. Missing atom as a source of carbon magnetism. *Phys. Rev. Lett.*, 104:096804, Mar 2010.

[74] M. M. Ugeda, D. Fernández-Torre, I. Brihuega, P. Pou, A. J. Martínez-Galera, Rubén Pérez, and J. M. Gómez-Rodríguez. Point defects on graphene on metals. *Phys. Rev. Lett.*, 107:116803, Sep 2011.

[75] Wendel S. Paz, Wanderlã L. Scopel, and Jair C.C. Freitas. On the connection between structural distortion and magnetism in graphene with a single vacancy. *Solid State Communications*, (0):–, 2013.

[76] M. Casartelli, S. Casolo, G. F. Tantardini, and R. Martinazzo. Spin coupling around a carbon atom vacancy in graphene. *Phys. Rev. B*, 88:195424, Nov 2013.

[77] C.C. Lee, Yukiko Yamada-takamura, and Taisuke Ozaki. Competing magnetism in π electrons in graphene with a single carbon vacancy. *arXiv:1311.0609v2*, pages 1–5, 2013.

[78] EJG Santos, S Riikonen, D Sanchez-Portal, and A Ayuela. Magnetism of single vacancies in rippled graphene. *The Journal of Physical Chemistry C*, 116(13):7602–7606, 2012.

[79] M A Cazalilla, A Iucci, Francisco Guinea, and A. H. Castro Neto. Local Moment Formation and Kondo Effect in Defective Graphene. *cond-mat/1207.3135*, 2012.

[80] T Kanao, H Matsuura, and M Ogata. No Title. *J. Phys. Soc. Japan*, 81:063709, 2012.

[81] Andrew K. Mitchell and Lars Fritz. Kondo effect with diverging hybridization: Possible realization in graphene with vacancies. *Phys. Rev. B*, 88:075104, Aug 2013.

[82] Taro Kanao, Hiroyasu Matsuura, and Masao Ogata. Theory of defect-induced kondo effect in graphene: Effect of zeeman field. *Journal of Physics: Conference Series*, 456(1):012018, 2013.

[83] Vitor M Pereira, F Guinea, J M B Lopes dos Santos, N M R Peres, and A H Castro Neto. Disorder Induced Localized States in Graphene. *Phys. Rev. Lett.*, 96:36801, 2006.

[84] P. Haase, S. Fuchs, T. Pruschke, H. Ochoa, and F. Guinea. Magnetic moments and kondo effect near vacancies and resonant scatterers in graphene. *Phys. Rev. B*, 83:241408, Jun 2011.

[85] O. Lehtinen and J. Kotakoski. Ion beam damage simulator for graphene http://www.helsinki.fi/nanocarbon/tools/ikmc/.

[86] M. Schüler, M. Rösner, T. O. Wehling, A. I. Lichtenstein, and M. I. Katsnelson. Optimal hubbard models for materials with nonlocal coulomb interactions: Graphene, silicene, and benzene. *Phys. Rev. Lett.*, 111:036601, Jul 2013.

[87] T. O. Wehling, E. Şaşıoğlu, C. Friedrich, A. I. Lichtenstein, M. I. Katsnelson, and S. Blügel. Strength of effective coulomb interactions in graphene and graphite. *Phys. Rev. Lett.*, 106:236805, Jun 2011.

[88] E. Miranda and V. Dobrosavljević. Localization-induced griffiths phase of disordered anderson lattices. *Phys. Rev. Lett.*, 86:264–267, Jan 2001.

[89] D. Tanasković, E. Miranda, and V. Dobrosavljević. Effective model of the electronic griffiths phase. *Phys. Rev. B*, 70:205108, Nov 2004.

[90] A. Zhuravlev, I. Zharekeshev, E. Gorelov, A. I. Lichtenstein, E. R. Mucciolo, and S. Kettemann. Nonperturbative scaling theory of free magnetic moment phases in disordered metals. *Phys. Rev. Lett.*, 99:247202, Dec 2007.

[91] P. S. Cornaglia, D. R. Grempel, and C. A. Balseiro. Universal distribution of kondo temperatures in dirty metals. *Phys. Rev. Lett.*, 96:117209, Mar 2006.

[92] E Miranda and V Dobrosavljević. Disorder-driven non-Fermi liquid behaviour of correlated electrons. *Reports on Progress in Physics*, 68(10):2337–2408, October 2005.

[93] A. H. Castro Neto, G. Castilla, and B. A. Jones. Non-fermi liquid behavior and griffiths phase in f-electron compounds. *Phys. Rev. Lett.*, 81(16):3531–3534, 1998.

[94] Olexei Motrunich, Siun-Chuon Mau, David A. Huse, and Daniel S. Fisher. Infinite-randomness quantum ising critical fixed points. *Phys. Rev. B*, 61:1160–1172, Jan 2000.

[95] E Miranda, V Dobrosavljevi, and G Kotliar. Kondo disorder : a possible route towards non-Fermi-liquid behaviour. *J. Phys. Condens. Matter*, 8:9871–9900, 1996.

[96] M. B. Lundeberg, R. Yang, J. Renard, and J. A. Folk. Defect-mediated spin relaxation and dephasing in graphene. *Phys. Rev. Lett.*, 110:156601, Apr 2013.

[97] Nikolaos Tombros, Csaba Jozsa, Mihaita Popinciuc, Harry T Jonkman, and Bart J van Wees. Electronic spin transport and spin precession in single graphene layers at room temperature. *Nature*, 448(7153):571–4, August 2007.

[98] Christian Ertler, Sergej Konschuh, Martin Gmitra, and Jaroslav Fabian. Electron spin relaxation in graphene: The role of the substrate. *Phys. Rev. B*, 80:041405, Jul 2009.

[99] J. R. Schrieffer and P. A. Wolff. Relation between the anderson and kondo hamiltonians. *Phys. Rev.*, 149:491–492, Sep 1966.

[100] P. Meyer. *Introductory probability and statistical applications*. Addison-Wesley Publishing Company, 2nd edition, 1970.